UNIVERSITÀ DEGLI STUDI DI MILANO

PHYSICS DEPARTMENT

Doctorate School in Physics, Astrophysics and Applied Physics

Cycle XXXII

Measuring CMB polarization with the LSPE experiment: simulation and sensitivity studies for the STRIP instrument

Disciplinary scientific sector FIS/05

Supervisor: Dr. Barbara CACCIANIGA

Co-supervisor: Dr. Maurizio TOMASI

Director of the School: Prof. Matteo PARIS

PhD Thesis of:

Silvia CAPRIOLI

A.Y. 2019-2020

Thesis Referees:

External Referee:
Dr. Gemma TESTERA

External Referee:
Dr. Andrea ZACCHEI

Commission of the final examination:

External Member:
Prof. Carlo BACCIGALUPI

External Member:
Prof. Marco PALLAVICINI

Internal Member:
Prof. Marco BERSANELLI

Final examination:

Date: February 19$^{\text{th}}$ 2020

Università degli Studi di Milano, Dipartimento di Fisica, Milano, Italy

In those days, in those distant days,
In those nights, in those remote nights,
In those years, in those distant years;
In the first days, when everything needed was brought into being;
In the first days, when everything needed was properly nourished,
when bread had been tasted for the first time in the shrines of the Land,
when the ovens of the Land had been made to work;
When heaven had moved away from earth;
and the earth had separated from heaven,
and the name of man was fixed.

From the prologue to the Sumerian epic poem
"Gilgamesh, Enkidu, and the Netherworld",
the oldest known written cosmogony, from perhaps 2600 B.C.

Contents

Introduction

Humankind has made stories about the origin of the Universe since prehistoric times, but it is only in the last hundred years that such myths and images have been replaced by a well-established scientific description of the origin and evolution of the Universe. The development of modern cosmology is with no doubt one of the scientific triumphs of the twentieth century, culminated in the establishment of the Standard Cosmological Model, representing an almost universal consensus amongst scientists as to the best description of our Universe. According to this model, the Universe started out in an extremely hot and dense state called the "Big Bang" about 13.8 billion years ago and continued expanding since then. The Standard Model is remarkably successful and supported by numerous astronomical evidences; however, ongoing mysteries such as the cause of the current accelerated expansion of the Universe and the true nature of dark matter make it clear that we have some way to go before we can say that a full picture of the physics of the Universe is complete.

The most important observation supporting the Standard Cosmological Model is the existence of the Cosmic Microwave Background (CMB) radiation, heat radiation released when the Universe was just few hundreds of thousands years old. From its discovery in the 1960s, more and more accurate observations of the CMB has followed, providing us invaluable information about the early history of the Universe obtainable in no other way.

The current frontier in the study of the Cosmic Microwave Background is the measurement of its polarization anisotropies. Indeed, the curl-like component of the CMB polarization field (also known as "B-modes") is thought to be holding the imprint of primordial gravitational waves, whose presence is predicted by the Inflationary paradigm. This theory accounts for the accelerated expansion of the Universe that is believed to have happened

in the very first stages of its life. The detection of B-modes would, therefore, provide a strong evidence for the inflationary theory, paving the way for the study of the physics of the very early Universe.

Unfortunately, such a signal is expected to be extremely faint (of the level of fraction of μK), which makes its detection anything but easy. To achieve the measurement of such tiny differences in the sky temperature, it is necessary to build complex experiments with extremely high sensitivity and to precisely characterize the astrophysical foregrounds, mainly coming from our Galaxy, that would mimic the primordial signal.

The quest for CMB B-modes is open and several experiments all around the World are trying to accomplish this difficult task. The Large Scale Polarization Explorer (LSPE), an italian-led experiment, is one of them and in its framework I carried out my PhD work.

LSPE will observe 25% of the sky in the Northern hemisphere relying on the synergy of two different instruments, a balloon-borne experiment (SWIPE) and a ground-based telescope (STRIP), complementary for frequency coverage and technology. During my PhD, I worked in the observational cosmology group of the University of Milan, which is deeply involved in the developement of the STRIP instrument and leads the activities involving its simulation and data analysis pipeline.

STRIP is composed by an array of 49 polarimeters based on radiometric technology and will observe the sky at a frequency of 43 GHz in order to characterize the Galactic synchrotron signal, the dominant sky emission at this frequency. A second channel, made of 6 polarimeters operating at 95 GHz has been included for atmospheric monitoring. STRIP will be installed at the Teide Observatory in Tenerife (Canary Islands, Spain) in late 2021, and at least two years of observations will follow.

The first part of my PhD work was devoted to the characterization of STRIP polarimeters, which took place from March 2017 to April 2018 at the University of Milano Bicocca. I have been involved in the operating team which carried out the tests procedure in the lab and I gave an important contribution to the data analysis, focusing in particular on the bandpass characterization.

The second and major part of this PhD thesis was focused on the implementation of a simulation pipeline for STRIP. The pipeline simulates STRIP observation, with the goal of computing end-to-end simulations of the sky observation in order to assess the scientific performance of the experiment. I particularly focused on the generation of realistic data time streams and on the implementation of a map-maker, following the destriping technique.

In order to extract the faint B-mode signal, the sensitivity of CMB experiments is constatly increasing and the size of their datasets is growing, approaching trillions of raw data samples. The reconstruction of the sky

map is a very important step of any CMB data analysis pipeline as it allows to compress by many orders of magnitude the data volume, while striving for preserving all the cosmological information. The map-making is made difficult by the fact that raw data do not include only sky signal, but also instrumental noise that, if not removed, generates unwanted structures in the sky map compromising the accuracy of the measurement. The destriping technique, initially developed for the Planck experiment, is an interesting way to perform map-making, as it has proven to be able to produce optimal maps with very low noise residuals in a reasonable computational time.

Thanks to the simulation pipeline I implemented, I was able to perform sensitivity studies to evaluate the behaviour of the destriping algorithm in the particular case of the STRIP experiment, and to estimate the impact of some systematics effects, in particular of the residual correlated noise and of the bandpass mismatch.

The thesis is organized as follows:

- **Chapter 1**: in this chapter I introduce the current theory describing the evolution of our Universe. After a brief description of the Standard Big Bang model, I focus the discussion on the Cosmic Microwave Background, describing its main features. Then, I outline the Inflationary paradigm, presented as a solution of several observational problems that the standard model is not able to explain. Finally, I review the physics underlying the CMB polarization signal together with the current status of observations.

- **Chapter 2**: in this chapter I review the main challenges an experiment aiming to measure the CMB polarized signal has to face. I start with a description of the Galactic foreground emissions and of the impact they can have on the observation of the CMB polarization. Then, I review the technological challenges that experiments have to overcome in order to reach the requested high sensitivities, from noise management to the main sources of systematic effect. Finally, I overview the main current and future experiments.

- **Chapter 3**: this chapter describes the LSPE experiment. After a general presentation of the experiment and of its scientific purposes, both the instruments (SWIPE and STRIP) are described, focusing in particular on the characteristics of the STRIP instrument.

- **Chapter 4**: in the first part of this Chapter, I review the architecture of the STRIP polarimeters, providing an analytical description of their functioning. Then, I describe the unit tests campaign, from the test procedures to the data analysis, ending with a discussion of the results.

- **Chapter 5**: here I describe the simulation pipeline I developed for the STRIP experiment. After shortly describing the main steps of the typical data analysis pipeline for a CMB experiment, I focus on the Map-making problem and in particular on the destriping technique and on its implementation strategy. After that, I present the other parts of the pipeline and I conclude with some validation examples.

- **Chapter 6**: in the last Chapter, I present some sensitivity studies perfomed by exploiting the simulation pipeline previously described. I discuss the performance of the destriper in the STRIP case and present the study of some systematics effects. I, finally, conclude with an outlook on possible future improvements to the simulation pipeline.

Chapter 1

The Cosmic Microwave Background

In this introductory Chapter we review the current understanding of the Universe, focusing our discussion on the Cosmic Microwave Background. In Sections 1.1 and 1.2 we provide a brief description of the Standard Big Bang model, the most widely held theory for the evolution of the Universe. The landmark evidence of the Big Bang is the existence of a relic radiation, the Cosmic Microwave Background (CMB), which is the oldest observable light and thus a unique window on the primordial Universe. The main features of the CMB are described in Section 1.3. Despite its numerous successes, the Standard Big Bang model is not able to provide explanation to some observations, as described in section 1.4. The Inflationary paradigm (Section 1.5), which postulates a period of accelerated expansion in the early Universe, is the most popular solution to these problems. If it really happened, Inflation should have left an imprint in the polarization pattern of the CMB in terms on B-modes. The hunt for B-modes has thus become one of the main targets of modern observational cosmology and represents the main topic of this work. Section 1.6 is focused on the polarization of the CMB, giving particular attention to the encoded information on the early Universe and to the current status of observations. The main references for this Chapter are Liddle, 2005 and Ryden, 2017.

1.1   An expanding Universe

The milestone of observational cosmology is the evidence that almost everything in the Universe appears to be moving away from us. This discovery dates back to 1929, when Edwin Hubble studied 24 galaxies (Hubble, 1929). In particular, he measured their relative distance by using Cepheids as *standard candels*[1] and their velocity, by measuring their redshift ($z := \frac{\lambda_{obs} - \lambda_{em}}{\lambda_{em}} = \frac{v}{c}$). Hubble derived its famous diagram (shown in the top panel of Figure 1.1) and he found that galaxies are apparently receding away from us with a velocity v that is proportional to their distance d from us:

$$v = H_0 d. \tag{1.1}$$

This linear relation is known as the *Hubble's law*, and the constant of proportionality H_0 is known as *Hubble's constant*. Latest measurements lead to a Hubble constant of about $67 \, \mathrm{km \, s^{-1} Mpc^{-1}}$ (Planck Collaboration et al., 2018). Hubble's measurement turns out to be affected by severe systematic errors (leading to a value of H_0 7 times greater with respect to the current estimate), but it is considered the first evidence of the expansion of the Universe, a key event that ultimately lead the scientific community to abandon the idea of a static Universe (dominant at the time) in favour of a dynamically evolving one. Over the decades since Hubble's discovery, numerous observations of the Hubble Law have been carried out to much greater distances and with much higher precision using a variety of standard candles, including Supernovae type-Ia (SNIa). The bottom panel of Figure 1.1 shows the most up-to-date Hubble diagram (Betoule et al., 2014), using SNIa as distance indicators for galaxies at distances hundreds times greater than the ones observed by Hubble. In 1998, two independent groups using SNIa (Riess et al., 1998; Perlmutter et al., 1999) showed a surprising deviation from linearity on a Hubble diagram. The results indicated that the expansion rate has been speeding up in the last ~ 6 billion years. The slight deviation from linearity, seen at large distances in Figure 1.1, is indeed the observational evidence for an accelerating universe. The nature of the mysterious *dark energy* that causes this acceleration is not yet known and is currently the greatest mystery of modern cosmology.

---

[1]In astronomy, a *standard candle* is a class of objects whose distances can be computed by comparing their observed brightness with their known luminosity. Cepheids are variable stars with a strong relationship between the luminosity and the pulsation period. This makes possible to know the true luminosity of a Cepheid by simply observing its pulsation period, which in turn allows one to determine the distance to the star, by comparing its known luminosity to its observed brightness.
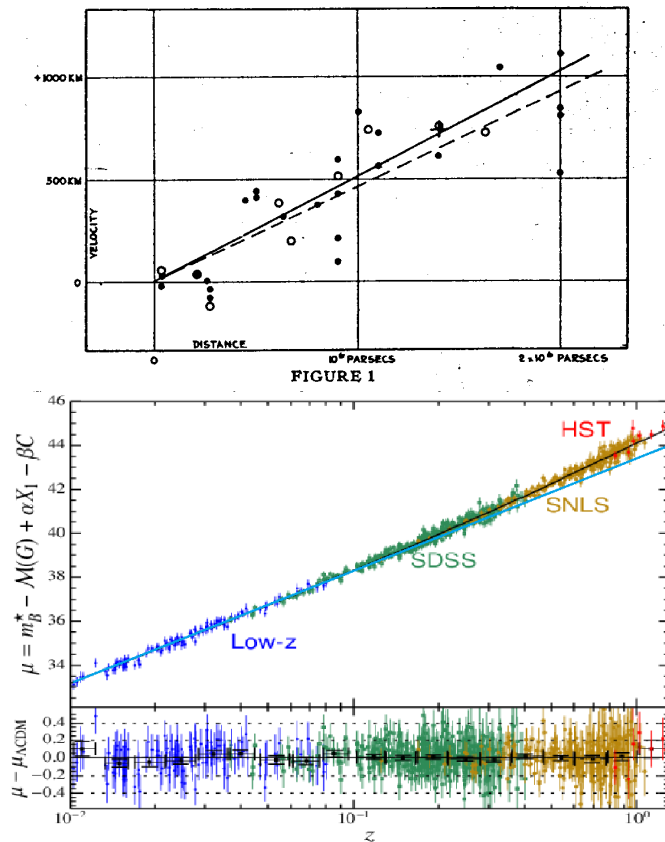
Figure 1.1: *Top*: Hubble's original diagram (1929). *Bottom*: state-of-art Hubble diagram using various SNIa samples. The different samples are denoted by different colors and are listed by name. Hubble's original diagram fits into a tiny spot near the origin of this graph (corresponding to our immediate cosmic neighborhood). The deviation from linearity (cyan line) is evident at large distances, showing that the expansion of the Universe is accelerating.

1.2   The Standard Big Bang Model

The "Big Bang" is the term given to what is currently the most widely accepted scientific model for the origin and evolution of the Universe. The Big Bang theory describes how the Universe expanded from a very high-density and high-temperature state and offers a comprehensive explanation for a broad range of observed phenomena.

The framework for the Big Bang model relies on Albert Einstein's theory of General Relativity and on the *cosmological principle*, which states that, if viewed on sufficiently large distance scales, the Universe is homogeneus (no preferred points) and isotropic (no preferred directions). This principle is still considered valid: observations show that, although very inhomogeneous on small scales (think of stars, galaxies and cluster of galaxies), the Universe is homogeneus on scales larger than superclusters ($> 100\,\mathrm{Mpc}$). Moreover, as we will see later, the Cosmic Microwave Background is isotropic at very high level.

To describe the evolution of the Universe, it is convenient to introduce the so-called *scale factor* $a(t)$, a dimensionless number which parametrize the relative expansion of the Universe as a function of time. Its present value is conventionally set equal to one. The physical distance between two objects (e.g. two galaxy clusters) at a given time t can be written as $r(t) = r_0 a(t)$, where r_0 is the *comoving distance*, equal to the physical distance at the present epoch. Consequently, Hubble's law 1.1 tells us that the proportionality constant should be:

$$H(t) := \frac{\dot{a}(t)}{a(t)}. \tag{1.2}$$

This quantity (function of time) is called *Hubble parameter* and its value as measured today is the Hubble constant H_0. Note that the unit of $H(t)$ is the inverse of a time: the so-called *Hubble time* $1/H(t)$ is the order of magnitude of the time required for a light ray to propagate over the distance $c/H(t)$ (called *Hubble length*) and provide a rough estimate for the size of the observable Universe[2] at time t. Another important quantity is the *cosmological redshift*, which quantifies the stretch in the wavelength of a photon due to the dilatation of space caused by the scale factor $a(t)$. If the photon's wavelength at the time of emission was λ_{em}, and the wavelength at the time of the observation was λ_{obs}, the cosmological expansion causes

---

[2]The observable Universe is a sphere within the Universe, centered on some observer, with a radius large enough to contain all the points of space which have been visible by the observer at some time in the past.

a redshift equal to:

$$z(t) := \frac{\lambda_{\text{obs}} - \lambda_{\text{em}}}{\lambda_{\text{em}}} = \frac{1}{a(t) - 1}. \tag{1.3}$$

To understand the evolution of the Universe we must investigate the evolution of the scale factor, thing that ultimately depends on the energy density of the Universe. The link between the evolution of the scale factor and the energy content of the Universe is provided by the Friedmann Equations, derived in 1922 from Einstein's equations of General Relativity.

1.2.1 The Friedmann Equations

In General Relativity (Einstein, 1916), the link between the metric and the energy content of space-time is established by Einstein's field equation:[3]

$$G^{\mu\nu} := R_{\mu\nu} - \frac{1}{2}Rg_\mu\nu = 8G\pi T_{\mu\nu}. \tag{1.4}$$

The left-hand side of this equation (the Einstein tensor $G^{\mu\nu}$) describes the geometry of space-time through the metric tensor ($g_{\mu\nu}$) and its first and second derivatives (contained in the Ricci tensor $R_{\mu\nu}$ and in the scalar curvature R). On the right-hand side, instead, the stress-energy (or energy-momentum) tensor $T_{\mu\nu}$ describes the distribution of mass and energy in space-time and it represents the source of gravitational field. Finally, G is the gravitational constant and c is the speed of light in vacuum.

The semplicity of Einstein's equation is deceptive, since it is actually a set of ten coupled nonlinear second-order differential equations. This makes it extremely difficult to solve in the general case. Nonetheless, several effective techniques for obtaining exact solutions in some specific cases have been established, the simplest involving imposing symmetry conditions on the metric tensor (e.g., stationarity, axisymmetry,...). In particular, things become much simpler if the cosmological principle is assumed. In this case, the metric describing the curvature of space-time is the *Friedmann-Lemaître-Robertson-Walker* (FRLW) metric:

$$ds^2 = dt^2 - a^2(t)\left[\frac{dr^2}{1 - kr^2} + r^2(d\theta^2 + \sin^2\theta d\phi^2)\right], \tag{1.5}$$

where spherical coordinates have been adopted. The function $a(t)$ is the scale factor introduced in the previous Section and parametrizes the evolution of the Universe. The value of the scalar factor a at some time t is a

---

[3]Adopting (here as in the rest of this discussion) the natural units $c = \hbar = 1$.
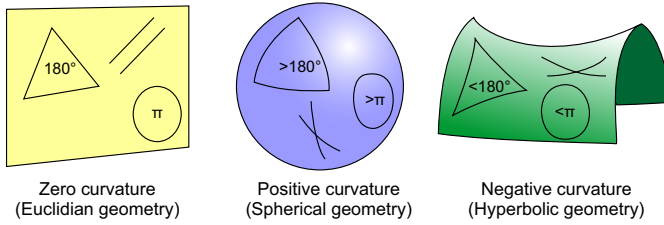
Figure 1.2: Three kinds of space curvature. For each curvature, the sum of the
internal angles of a triangle, the area of a circle with radius $r = 1$
and the behaviour of parallel lines are presented. In non-euclidean
geometries, parallel lines can intersect and non-parallel lines can be
non-intersecting. According to Friedmann's equations, the properties
of space belong to one of these threee kinds of geometries, depending
on the distribution of mass and energy.

pure number that multiplies the spatial part of the metric, and therefore it
quantifies how space dilates or contracts. The quantity k parametrizes the
spatial *curvature* of the Universe defining its geometry, in particular:

- k = 0: euclidean geometry (*flat Universe*);

- k > 0: spherical geometry;

- k < 0: hyperbolic geometry.

The three cases are schematically depicted in Fig. 1.2.
   Under the assuption of homogeneus and isotropic universe, the stress-
energy tensor $T_{\mu\nu}$ assumes the form of a perfect fluid:

$$T_{\mu\nu} = (\rho + P)u_\mu u_\nu - P g_{\mu\nu}, \tag{1.6}$$

where ρ and P are respectively the energy density and the pressure of the
fluid and $u_{\mu\nu}$ is the four-velocity. By using this expression for the energy-
momentum tensor and the FRLW metric, Einstein's equations 1.4 reduce to
the much simpler *Friedmann equations*, which describes the behaviour of the
scale factor $a(t)$ in terms of few observables:

$$\left(\frac{\dot{a}(t)}{a(t)}\right)^2 = \frac{8\pi G}{3}\rho(t) - \frac{k}{a^2}, \tag{1.7}$$

$$\frac{\ddot{a}(t)}{a(t)} = -\frac{4\pi G}{3}(\rho(t) + 3P(t)). \tag{1.8}$$

By looking at the first Friedmann equation we notice that the space curvature
has an impact on the evolution of the Universe (see Figure 1.3): if $k < 0$, both

the terms on the right-side of the equation are positive and, consequently, the Universe will expand forever; if $k = 0$, the Universe will still expand forever (since $\rho > 0$), but at lower speed. On the other hand, if $k > 0$, the two terms will eventually cancel out, leading to a collapse of the Universe (*Big Crunch*)[4]. Recent measurements suggests our Universe is spatially flat (Planck Collaboration et al., 2018).

The second equation, also known as the *acceleration equation*, implies that if the material has any (positive) pressure, this further decelerates the expansion[5].

Besides the two Friedmann equations, the covariant conservation of the energy-momentum tensor $D_\mu T^{\mu\nu} = 0$ (embedded in the Einstein equations, since $D_\mu G^{\mu\nu} = 0$) gives another useful expression:

$$\dot\rho + 3(\rho + P)\frac{\dot a(t)}{a(t)} = 0, \tag{1.9}$$

which is called the *fluid equation*. Of these three equations, just two are independent. To solve for the three unknown functions ($a(t)$, $\rho(t)$, $P(t)$) we need an *equation of state* $P(\rho)$, that is a mathematical relation between the pressure and the energy density of the content of the Universe. In general, the equation of state can be dauntingly complicated, but in most cosmological cases it can be written in a simple linear form:

$$P = w\rho \tag{1.10}$$

where w is a dimensionless number whose value depends on the component of the Universe we are considering. Cosmologists have identified three main components:

- **Matter**: intended as "non-relativistic" matter, which includes baryonic matter and Cold Dark Matter (CDM). Matter exerts negligible pressure, therefore $P = 0$ and so, $w = 0$. Hence, from the fluid equation we get:

$$\rho_{\mathrm{m}} \propto \frac{1}{a(t)^3}, \tag{1.11}$$

  which says that, as expected, the density falls off in proportion to the volume of the Universe. Solving the Friedmann equations for a matter-dominated Universe (in case of $k = 0$) gives:

$$H := \frac{\dot a}{a} = \frac{2}{3t}, \tag{1.12}$$

---

[4]This is true for a matter or radiation dominated Universe.
[5]There are no pressure forces in a homogeneous Universe, because density and pressure are everywhere the same. A pressure gradient is required to supply a force.

meaning that the Universe expands forever but with a rate of expansion decreasing in time.

- **Radiation**: made of relativistic particles (photons and neutrinos). Their kinetic energy leads to a pressure force, the radiation pressure, which can be shown to be $P = \rho/3$. For radiation:

$$\rho_{\rm r} \propto \frac{1}{a(t)^4}, \tag{1.13}$$

$$H := \frac{\dot{a}}{a} = \frac{1}{2t}, \tag{1.14}$$

which tell us that the Universe expands more slowly if radiation dominates than if matter dominates, a consequence of the extra deceleration that the pressure supplies.

- **Cosmological constant**: it appears in the Friedmann equations as an extra term Λ, giving:

$$\left(\frac{\dot{a}}{a}\right)^2 = \frac{8\pi G}{3}\rho - \frac{k}{a^2} + \frac{\Lambda}{3}, \tag{1.15}$$

$$\frac{\ddot{a}}{a} = -\frac{4\pi G}{3}(\rho + 3P) + \frac{\Lambda}{3}. \tag{1.16}$$

Einstein originally introduced the cosmological constant in 1917 to counterbalance the effects of gravity and achieve a static Universe, a notion which was the most accepted view at the time. Einstein abandoned the concept in 1931 after Hubble's discovery of the expanding Universe. The surprising discovery in 1998 that the expansion of the Universe is accelerating, however, implies the possibility of a positive value for the cosmological constant. From equation 1.16, in fact, a positive cosmological constant gives a positive contribution to $\ddot{a}$ and acts effectively as a repulsive force. If sufficiently large, it can overcome the gravitational attraction represented by the first term and lead to an accelerating Universe.
In order to compare Λ to the othere constituents of the Universe, it is useful to describe it as a fluid, defining an energy density ρ_Λ:

$$\rho_\Lambda := \frac{\Lambda}{8\pi G}. \tag{1.17}$$

Considering the fluid equation 1.9 in this case, we get:
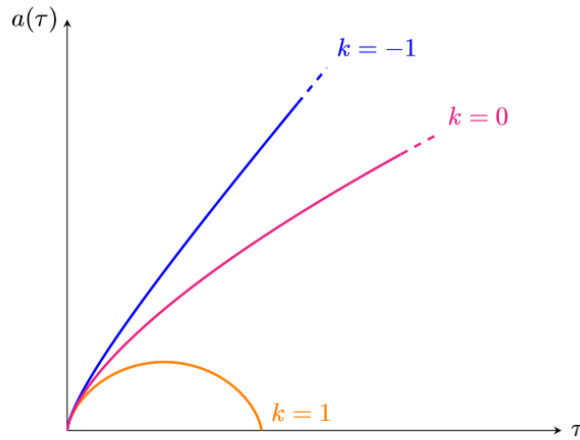
Figure 1.3: Three possible evolutions for the Universe, corresponding to the different signs of k.

$$\dot{\rho}_\Lambda + \frac{\dot{a}}{a}(\rho_\Lambda + P_\Lambda) = 0. \tag{1.18}$$

And, since ρ_Λ is constant by definition, we must have:

$$\rho_\Lambda = -P_\Lambda, \tag{1.19}$$

which means that the cosmological constant has *negative* pressure. The physical nature of the cosmological constant is still a mistery. One possibility is that it is due to *vacuum energy*, an underlying background caused by quantum fluctuations determing the continuous creation and annihilation of particles over all the space-time.

In a Universe made of matter, radiation and cosmological constant, the total energy density is:

$$\rho_{\text{tot}}(a) = \frac{\rho_{\text{m}}}{a^3} + \frac{\rho_{\text{r}}}{a^4} + \rho_\Lambda, \tag{1.20}$$

which means that, in an expanding Universe, the energy density is at first dominated by radiation, then by matter, and finally by dark energy. The three phases are depicted in Figure 1.5.

There is one last important quantity that can be derived from the Friedmann equations, the *critical density*. In the hypotesis of a flat Universe, Eq. 1.7 reduces to:

$$H^2(t) = \frac{8\pi G}{3}\rho(t), \tag{1.21}$$
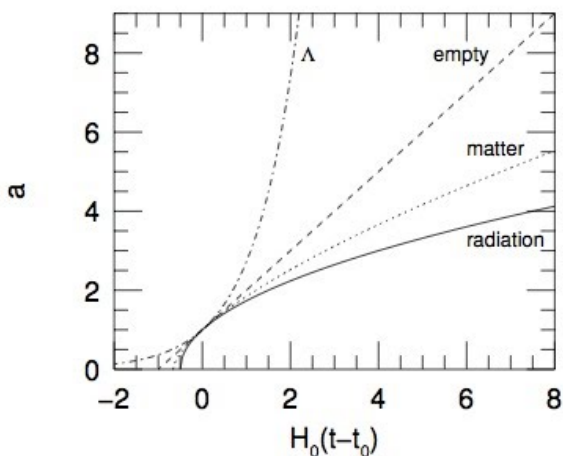
Figure 1.4: The scale factor as a function of time for an expanding empty Universe (dashed), a flat matter-dominated Universe (dotted), a flat radiation-dominated Universe (solid) and a flat Λ-dominated Universe (dot-dash).
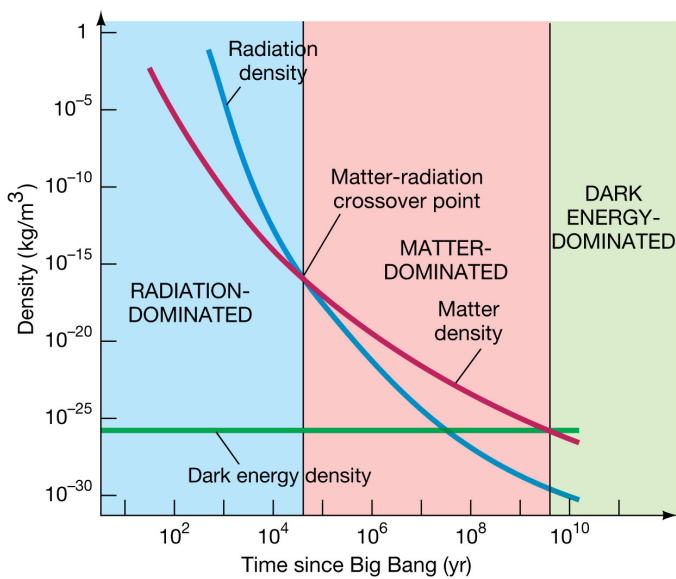
Figure 1.5: Evolution of the energy density of the Universe as a function of time. The energy density is dominated first by radiation ($\rho \sim 1/a(t)^3$), then by matter ($\rho \sim 1/a(t)^4$) and finally by the dark energy ($\rho \sim$ const.). The cross-over points define three cosmic eras.

which means that for any value of the Hubble parameter $H(t)$ there is a *critical density*:

$$\rho_c(t) = \frac{3H^2(t)}{8\pi G}, \tag{1.22}$$

which is the energy density that a flat (Euclidean) Universe must possess (larger densities lead to a positevely curved space, smaller densities to a negatively curved one). Rather that quote the density of the Universe directly, in cosmology it is common to quote its value relative to the critical density:

$$\Omega(t) := \frac{\rho(t)}{\rho_c}, \tag{1.23}$$

$$\Omega_m = \Omega_b + \Omega_c = \frac{\rho_m}{\rho_c}, \qquad \Omega_r = \Omega_\gamma + \Omega_\nu = \frac{\rho_r}{\rho_c}, \qquad \Omega_\Lambda = \frac{\rho_\Lambda}{\rho_c}, \tag{1.24}$$

where Ω_m expresses the density of matter (baryonic matter Ω_b plus dark matter Ω_c), Ω_r the density of radiation (photons Ω_γ plus neutrinos Ω_ν), and Ω_Λ the density of dark energy. The Ω parameter is determined by all components of the cosmological fluid:

$$\Omega_{\text{tot}} = \frac{\rho_{\text{tot}}}{\rho_c} = \Omega_m + \Omega_r + \Omega_\Lambda. \tag{1.25}$$

By rewriting equation 1.7 as:

$$\Omega_{\text{tot}}(t) - 1 = \frac{k}{a^2(t)H^2(t)}, \tag{1.26}$$

we notice that Ω_{tot} and the spatial curvature k are strictly connected: if $k = 0$ than $\Omega_{\text{tot}} = 1$, that is $\rho_{\text{tot}} = \rho_{\text{crit}}$ (if $k > 0$ than $\Omega_{\text{tot}} > 1$, if $k < 0$ than $\Omega_{\text{tot}} < 1$). As a consequence, by measuring the current energy density of the Universe and comparing it with the current value of the critical density, it is possible to know the spacial geometry of the Universe. The density of the Universe today is very close to the critical one evaluated today (Planck Collaboration et al., 2018), and it is about $10^{-26}\text{kg}/\text{m}^3$ (10 hydrogen atoms per m^3). This suggests an almost spacially flat Universe.

We can finally rewrite the first Friedmann equation as:

$$H^2(t) = H_0^2 \left(\frac{\Omega_{m,0}}{a^3} + \frac{\Omega_{r,0}}{a^4} + \Omega_{\Lambda,0} \right) - \frac{k}{a^2}, \tag{1.27}$$

where the subscript 0 indicates the value of the parameter evaluated at present time. H_0, Ω_m and Ω_b constitutes three of the six fundamental

cosmological parameters, which completely characterize the dynamic of our Universe. These parameters can be estimated from the observations of the Cosmic Microwave Background (see Section 1.3.1) and from them all the other cosmological parameters can be derived.

1.2.2   A brief history of the Universe

Knowing from observations that our Universe is expanding, we can imagine to travel backwards through its evolution, until the scale factor $a(t)$ reaches zero (*initial singularity*). This extrapolation leads to a Universe with infinite density and temperature in a finite time in the past (about 13.8 billion years ago), known as the **Big Bang**. In the vicinity of the Big Bang the Universe was at extremely high energies and quantum effects affected cosmological scales. In this regime, the standard Big Bang model, which is based on a non-quantum description of gravity, is no-longer valid. As a consequence, the Big Bang model does not state that a singularity necessarily occured, but it predicts an initial epoch in which the general relativity and the standard model of particle physics alone are not adequate to describe the physical phenomena. This epoch is known as *Planck epoch* and it is thought to have lasted until about 10^{-43} s after the Big Bang (or equivalently, when the temperature of the Universe was above 10^{32} K).

After the Planck era, we can imagine that the Universe was in a very hot and dense state in which all the particles were in the state of a primodial plasma. Temperatures were so high that the electromagnetic, weak and strong forces were unified in a single force (Grand Unified Theory, GUT) and the random motions of particles were at relativistic speeds, with particle–antiparticle pairs of all kinds being continuously created and annihilated in collisions. At some point, an unknown reaction called *baryogenesis*, violated the conservation of baryon number, leading to a very small excess of quarks and leptons over antiquarks and antileptons (of the order of one part in 30 million). This resulted in the predominance of matter over antimatter in the present Universe.

After about 10^{-11} s, the picture becomes less speculative, since particle energies drop to values that can be attained in particle accelerators. Symmetry breaking phase transitions put the fundamental forces of physics and the parameters of elementary particles into their present form. As the time goes by, the Universe continues to decrease in density and fall in temperature, reducing the kinetic energy of particles and allowing them to combine and form heavier particles. At about 10^{-6} s, quarks and gluons combined to form baryons such as protons and neutrons. The small excess of quarks over antiquarks led to a small excess of baryons over antibaryons. The temperature was now no longer high enough to create new baryon–antibaryon

pairs, so a mass annihilation immediately followed, leaving just one in 10^{10} of the original protons and neutrons, and none of their antiparticles.

At approximately 1 s after the Big Bang, neutrinos decoupled from matter and began traveling freely through space. As neutrinos rarely interact with matter, this cosmic neutrino background still exist today. However, since the neutrinos from this event have a very low energy ($10^{-4} \div 10^{-6}$ ev), their detection is far beyond the capabilities of present generation neutrino detectors. An annihilation process similar to the baryon-antibaryon one happened for electrons and positrons, when the photon energy drops under the rest mass of the electron-positron couple (500 KeV), breaking the balance between the pair production reaction ($2\gamma \to e^+ + e^-$) and the annihilation ($e^+ + e^- \to 2\gamma$) and favouring the latter. After these annihilations, the remaining protons, neutrons and electrons were no longer moving relativistically and the energy density of the Universe was dominated by photons (with a minor contribution from neutrinos).

From approximately 10 s, the photon energy became low enough to disable the photo-dissociation of deuterium nuclei, giving way to the *primordial nucleosynthesis* phase which lead to the formation of Hydrogen, Helium and Lithium nuclei. The successful prediction of the H, He and Li abundances in our Universe is one of the most convincing evidence supporting the Big Bang Theory. At about 3000 years after the Big Bang, the matter density reaches the radiation density, starting the matter-dominated era.

At this time of the evolution of the Universe, photons were still energetic enough to ionize the neutral atoms that at times formed. Electrons were mostly free and continuously interact with photons through Thomson scattering ($\gamma + e^- \to \gamma + e^-$). Matter and radiation were coupled in a ionized plasma and photons could not travel significant distances without interacting with ionized particles. As a result, the universe was opaque. This phase ended about 380 000 years after the Big Bang, when the temperature became low enough ($T \sim 3000$ K) to allow the formation of neutral atoms from the combination of nuclei and electrons (*recombination*). This broke the equilibrium between matter and radiation and the mean free path of photons suddenly diverged to infinity. Photons *decoupled* from matter and freely start to propagate through space. Today, about 13.8 billion years later, we see these primordial photons as a **Cosmic Microwave Background** (CMB), which constitutes an extraordinary cosmological instrument, as it provides a snapshot of the early Universe at the moment of recombination.

As the Universe evolved, the small dishomogeneities in the matter distribution grew via gravitational instability until the first stars and galaxies formed at $z \sim 20 \div 10$ (from 180 to 500 million years after the Big Bang). Today it is believed that the formation of structure proceeded from the smallest one (stars and then galaxies) to the largest one (clusters of galaxies)

in a so-called bottom-up scenario, by amalgamation. This is possible only if the dark matter is non-relativistic, favouring the structures accretion (Cold Dark Matter).

Around redshift $z \sim 16$ (250 million years), high energy photons from the first stars began to ionize the hydrogen in the inter-galactic medium, producing free electrons which were once more able to interact with the relic photons via Thomson scattering. This event is usually called *reionization*. However, the density of the Universe at this time was far smaller than at the time of recombination, and therefore these new interactions were not frequent enough to re-establish thermal equilibrium between matter and radiation anymore. The reionization phase gradually diminished and probably came to an end by around $z \sim 5$ (1 billion years) as the era of Population III stars and quasars, and their intense radiation, came to an end, and the ionized hydrogen gradually reverted to neutral atoms. In the meanwhile, the most massive stars ended their life-cycle and exploded as supernova creating the heavy elements (C, O,...). Finally, at $z \sim 1$ (6 billion years), the cosmological constant start to dominate the Universe, leading to the accelerating expansion we observe today.

Because of the double assumption of the presence of cold dark matter and dark energy, the standard model of cosmology is called the Λ**CDM model** (Λ Cold Dark Matter).

1.3   The Cosmic Microwave Background

One of the consequences of the Big Bang model is the existence of the Cosmic Microwave Background, a relic electromagnetic radiation that permeates the Universe. As seen in previus section, the CMB was emitted when the Universe was about 380 000 years old, after the decoupling of matter and radiation. The decoupling happened *everywhere*, in the sense that every point of space can be considered as an emitter of freely-propagating photons at the time of decupling. As earthly observers, we can see only the photons emitted by a spherical shell centered on Earth, called *Last Scattering Surface* (LSS), which includes the points in space at the right distance from us so that we are now receiving photons originally emitted from those points at the time of decoupling (see Figure 1.7). The LSS is now located at $z \sim 1100$ and will progressively get away as the Universe expands.

The first theoretical prediction of the presence of a relic radiation produced during the first stages of the Universe was made by Gamow, Alpher and Herman in 1948 (Alpher, 2014), but its detection happened nearly twenty years later, with the serendipitous observation made by Penzias and Wilson, two researches at Bell laboratories in Holmdel, New Jersey. While calibrating a radio antenna to be used for telecommunication and galactic
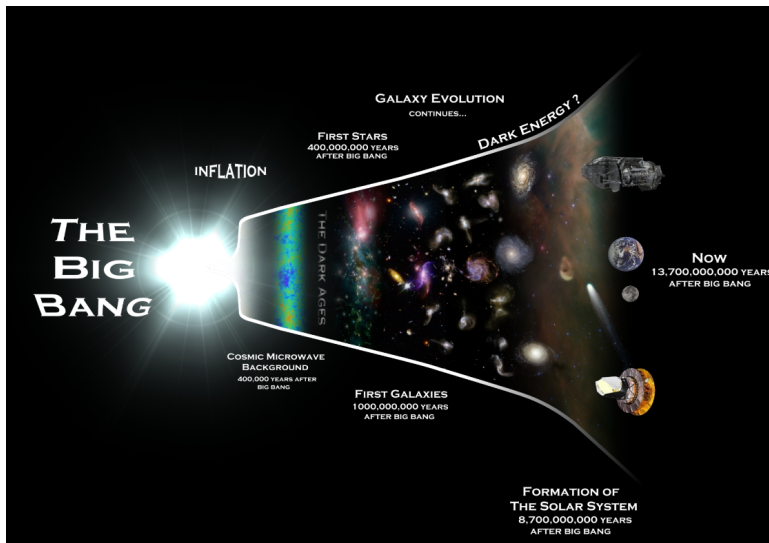
Figure 1.6: Depiction of the evolution of the Universe according to the Big Bang model. Time flows from left to right. The white lines which borders the plot constitute a rough depiction of the behaviour of the scale factor $a(t)$. Taken from http://planck.cf.ac.uk/science/timeline/universe.
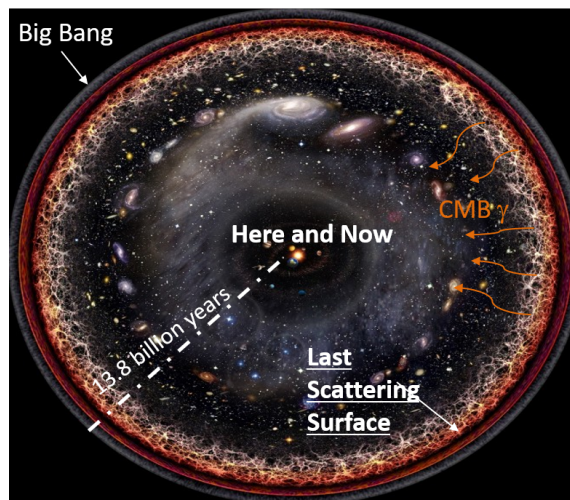
Figure 1.7: Artistic logarithmic scale conception of the Universe (author: Pablo Carlos Budassi). We, as observers on Earth, see the CMB as photons coming from the Last Scattering Surface, a spherical shell at $z \sim 1100$ surrounding us.

radio astronomy, they found an unexplained source of noise within the system, the same regardless of the direction on the sky the antenna was pointed to and with a temperature of 3 K (assuming a black-body spectrum) (Penzias and Wilson, 1965). For about an year they tried to track down the origin of this noise, when they eventually turned to Robert Dicke, a professor at Princeton University, for help. Dicke and his collegue Jim Peebles immediately offered the correct interpretation of the data, as they had realized several years earlier that the Big Bang model implied the existence of a relic radiation, and that this radiation should be detectable today with a black-body spectrum with a temperature of few kelvin. Dicke's group was even building a dedicate detector when the two researchers contacted him. The discovery of the Cosmic Microwave Background earned Penzias and Wilson the 1978 Nobel Prize in Physics, while its prediction earned Peebles the 2019 Nobel Prize. Since then, many accurate measurements of the CMB radiation have been carried out by three dedicated space missions (COBE (Fixsen et al., 1997), WMAP (Bennett et al., 2003), Planck (Planck Collaboration, 2016)) and many ground-based and balloon-borne experiments.

Today we know that this radiation has a black-body spectrum at the temperature $T = 2.725 \pm 0.001$ K, peaked in the microwave range $\lambda_{\mathrm{max}} \simeq 1$ mm, with a number density of photons $n_\gamma \approx 400 \, \mathrm{cm}^{-3}$. The spectrum of the CMB was measured with high accuracy by the FIRAS (*Far Infrared Absolute Spectrophotometer*) instrument onboard the COBE (*COsmic Background Explorer* satellite, Fixsen et al., 1997). The spectral radiance of a black-body is given by the Planck law:

$$B_\nu(\nu, T) = \frac{2h\nu^3}{c^2} \frac{1}{e^{\frac{h\nu}{k_b T}} - 1}, \tag{1.28}$$

where ν is the frequency of the electromagnetic radiation emitted and T is the temperature of the body. At the time of decoupling, the temperature of the Universe was about 3000 K, and then, for Wien law, $\lambda_{\mathrm{max}} \simeq 960$ nm, which means that CMB photons were originally emitted in the infrared. We know, however, that the energy density of the radiation emitted by a black body is given by the Stefan-Boltzmann law: $\rho \sim \sigma T^4$, and we know from 1.13 that $\rho \sim 1/a^4$. This means that the expansion of the Universe reduces the temperature of the CMB as $T \sim 1/a$. Moreover, because of cosmological redshift, the CMB photons are stretched and shifted to lower frequencies, $\nu \sim 1/a$, implying $\nu/T \sim$ const. As a consequence, the photons of the CMB propagated up to us while preserving the black-body shape they have at the time of recombination. Deviations from the perfect black-body spectrum (not found, so far) would imply deviations in the thermodynamic equilibrium of primordial plasma. The only effect of the expansion of the
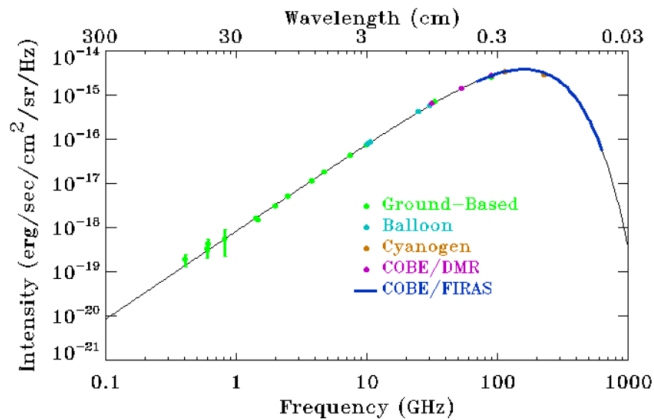
Figure 1.8: The spectrum of the Cosmic Microwave Bakground, measured by several experiments. The most precise measurements of the CMB spectrum at the millimeter wavelengths near its peak were made by the Far Infrared Asbolute Spectrophotometer (FIRAS) instrument aboard the Cosmic Background Explorer (COBE) satellite. FIRAS determined the CMB temperature to be $2.725 \pm 0.001\,\mathrm{K}$, with deviations from a perfect blackbody limited to less than 50 parts per million in intensity.

Universe on the CMB was to shift the spectrum peak from the infrared to the microwave range, which is equivalent to cool the temperature from 3000 to 2.7 K.

1.3.1   Temperature fluctuations

The black-body spectrum is not the only feature of the CMB. We also know that it is extremely isotropic, showing the same black-body spectrum at $\overline{T} = 2.7\,\mathrm{K}$ from every direction in the sky. It is not perfectly isotropic, though. It shows tiny temperature anisotropies of the order of:

$$\frac{\Delta T}{T}(\theta, \phi) = \frac{T(\theta, \phi) - \overline{T}}{\overline{T}} \approx 10^{-5}, \tag{1.29}$$

where $(\theta \phi)$ identifies a point on the celestial sphere. These anisotropies are not unexpected: the presence of fluctuations in the matter density of the primordial Universe are necessary to generate the gravitational imbalance that allowed the formation of the large scale structures (stars, galaxies and cluster of galaxies) we observe in our Universe today. Since at decoupling time matter and radiation were strongly coupled, fluctuations in the matter density implicated fluctuations in the radiation density, which now we observe as fluctuations in the CMB temperature.

To statistically analize the CMB anisotropies, it is useful to study the angular distribution of the temperature field on the sphere. Let us expand the CMB temperature field using spherical harmonics $Y_{lm}(\theta\phi)$ as orthonormal basis:

$$T(\theta, \phi) = \sum_{l=0}^{\infty} \sum_{m=-l}^{l} a_{lm} Y_{lm}(\theta, \phi). \tag{1.30}$$

An interesting property of spherical harmonics is that the angular scale of their oscillations is roughly $180°/l$, where l is called multipole moment. Therefore, the module of the complex number a_{lm} quantifies the amplitude of perturbations at a specific angular scale. The quantity mostly analized by cosmologists is however the *power spectrum C_l*, which, under the assumption of Gaussian fluctuations, provides a complete statistical description of the temperature field:

$$C_l :=< a_{lm}a_{lm}^* >= \frac{1}{2l+1} \sum_{m=-l}^{l} a_{lm}a_{lm}^*. \tag{1.31}$$

Since there are only $2l + 1$ coefficients a_{lm} for any fixed l, this means that the average is made on more and more values as l increases; on the other hand, for small values of l, the statistical error on the estimate of C_l will be larger. This statistical error is called *cosmic variance* and it represents an intrinsic uncertainty in the knowledge of the C_l. It is unavoidable, as we "have only one sky" to look at. Its mathematical expression is:

$$\Delta C_l = C_l \sqrt{\frac{1}{2l+1}}. \tag{1.32}$$

In Figure 1.9 the most up-to-date full sky map of the CMB temperatures anisotropies is shown, obtained thanks to the measurements of the Planck satellite. The power spectrum of this map is shown in Figure 1.10., where $D_l := l(l + 1)C_l/2\pi$ is plotted as a function of the multipole moment. The power spectrum of the CMB contains invaluable cosmologic information: its shape, in fact, is determined by the primordial fluctuations, which in turn are influenced by the cosmological parameters of our Universe. There are actually two types of anisotropies: primary anisotropies, due to effects that occured at the last scattering surface and before; and secondary anisotropies, due to effects which occured between the last scattering surface and the observer. Sources of secondary anisotropies are for example gravitational lensing, which deflects CMB photons in proximity of galaxy clusters, and the Sunyaev-Zeldovich effect, which distorts the spectrum of the CMB through inverse Compton in the intracluster medium.
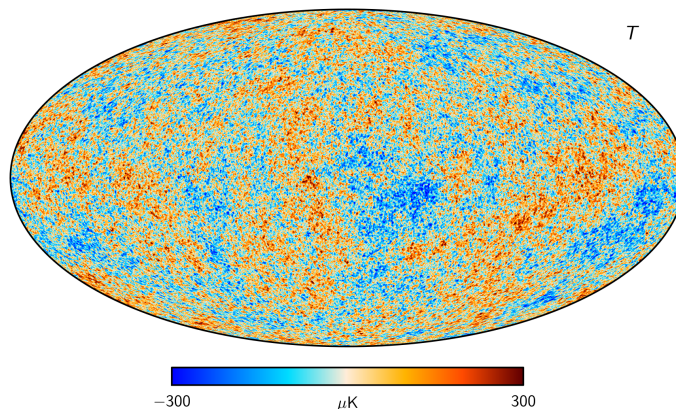
Figure 1.9: Map of the CMB temperature anisotropies obtained from four years of data of the Planck satellite. The full-sky map is shown using the Mollweide projection. The angular resolution is 5 arcmin (Planck Collaboration, 2018).

The structure of the CMB primary anisotropies is principally determined by acoustic oscillations, arising from a conflict in the photon–baryon plasma in the early Universe. The pressure of the photons tends to erase anisotropies, whereas the gravitational attraction of the baryons makes them collapse to form overdensities. These two effects compete to create acoustic oscillations, which give the power spectrum its characteristic peak structure. The peaks correspond, roughly, to resonances in which the photons decoupled when a particular mode (i.e. a particular angular scale) was at its oscillation peak. The acoustic oscillation involves angular scales from $1°$ to $5'$ ($100 \leq l \leq 1500$). Since the causal horizon at the time of decoupling was of about $1°$, at higher angular scales the acoustic oscillations had no time to start. At lower angular scales, on the other hand, the anisotropies are diluted because of photon diffusion process in the plasma (*Silk damping*). The peaks contain interesting physical signatures: the angular scale of the first peak, for example, determines the curvature of the Universe; the ratio between the odd peaks amplitude and the even peaks amplitude is related to the baryon density; the third peak can be used to get information about the dark-matter density, and so on.

By fitting the power spectrum with a ΛCDM model, it is possible to estimate the six main cosmological parameters, which completely determine the evolution of the (ΛCDM) Universe (Planck Collaboration et al., 2018). These six parameters are:

- *Hubble constant*: defined as in equation 1.2, it quantifies the expansion
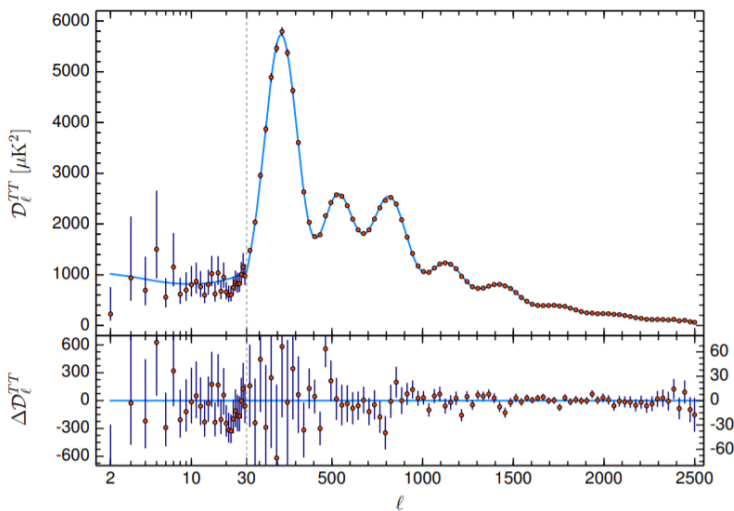
Figure 1.10: Power spectrum of the CMB temperature primary anisotropies obtained from the Planck map in Fig. 1.9. Error bars at lower multipoles are due to the instrinsic cosmic variance. The blue solid line represents the best ΛCDM model fit. The lower panel shows the residual with respect to this model. The vertical scale changes at $l = 30$, where the horizontal axis switches from logarithmic to linear. (Planck Collaboration et al., 2018)

rate of the Universe today:

$$H_0 = 67.36 \pm 0.54\,\mathrm{km\,s}^{-1}\mathrm{Mpc}^{-1}.$$

- *Barionic matter, dark matter and dark energy densities*:

$$\Omega_b h^2 = 0.02237 \pm 0.00015,$$
$$\Omega_c h^2 = 0.1200 \pm 0.0012,$$
$$\Omega_\Lambda = 0.6847 \pm 0.0073,$$

where $h := H_0/100\mathrm{kms}^{-1}\mathrm{Mpc}^{-1}$. So, in approximate percentage terms, the Planck results indicate 69% dark energy, 26% dark matter, and 5% ordinary matter as the mass-energy balance of our Universe.

- *Acoustic scale*: the characteristic angular size of the fluctuations in the CMB. It is defined as $\theta_* := r_s/D_m$, where r_s is the comoving size of the sound horizon at the time of recombination and D_m the comoving angular diameter distance, that maps this size into an angle on the sky.

Its value is constrained by the position of the peaks (and not by their amplitude):

$$0.59643° \pm 0.00026°.$$

- *Scalar spectral index*: primordial fluctuations are expected on all length scales. For density perturbations (i.e. scalar perturbations), the power spectrum $P_s(k)$ is predicted to be proportional to the wavenumber: $P_s(k) \propto k^{n_s-1}$. According to this law, a spectral index equal to one corresponds to scale invariant fluctuations.

$$n_s = 0.9649 \pm 0.0042.$$

- *Optical depth*: small-scale flutuations in the CMB are damped by Thomson scattering from free electrons generated during the epoch of reionization. This scattering suppress the amplitude of the power spectrum by a factor $e^{-\tau}$ on scales smaller that the horizon at reionization.

$$\tau = 0.0544^{+0.0070}_{-0.0081}.$$

1.4 Problems of the Standard Big Bang model

The Standard Big Bang model is spectacularly successful. It provides a reliable and tested accounting of the history of the Universe from about 10^{-11} s after the Big Bang until today, 18 billion years later. The primary pieces of evidence that support the model are: the expansion of the Universe, the discovery and measurement of the CMB and of its temperature fluctuations, the relative abundances of light elements produced by Big Bang nucleosynthesis, and the distribution of large-scale cosmic structures. As it is, however, the model is incomplete. Indeed, it has to postulate the existence of dark matter and dark energy, the nature of which is still unknown. Moreover, there are some issues, coming from observations, that the model is not able to satisfactorily solve.

1.4.1 The flatness problem

Current observations show an almost spatially flat Universe. Let us examine the evolution of the space-time curvature by recalling equation 1.26. In a matter- or radiation-dominated Universe, we have:

$$|\Omega_{\text{tot}}(t) - 1| \propto t \qquad \text{radiation domination,}$$
$$|\Omega_{\text{tot}}(t) - 1| \propto t^{2/3} \qquad \text{matter domination.}$$

In either case, the difference between Ω_{tot} and 1 is an increasing function of time. That means that the flat geometry is an unstable situation for the Universe: if there is any deviation from it, the Universe will become more and more curved. Consequently, the fact that the Universe is so close to flatness today means that at very early age it must have been *extremely* close to the flat geometry. In particular, at the time of nucleosynthesis, an era we think to understand well, the density parameter must have lain within the very restrictive range of $|\Omega_{\text{tot}}(t) - 1| < 7 \times 10^{-16}$ (which even decreases to $|\Omega_{\text{tot}}(t) - 1| < 2 \times 10^{-62}$ going back to the Planck era). Any other value would led to a Universe very different from that which we observe. This *fine-tuning* of the inital conditions of the Universe appears far-fetched: it would be far more satisfactory if we could find a physical mechanism for flattening the early Universe, instead of relying on extremely artificial initial conditions.

1.4.2   The horizon problem

The Universe has a finite age, so, since the singularity, photons have travelled only for a finite time. The comoving distance that light could have traveled in a time t is:

$$\eta = \int_0^{t_{\text{dec}}} \frac{dt'}{a(t')} \tag{1.33}$$

This length, called *comoving horizon*, implies that regions separated by distance larger than the comoving horizon are not casually connected. One of the most important properties of the CMB is that it is homogeneous and isotropic on very large scales: to very great accuracy, it has the same temperature of 2.725 K all over the sky. Being at the same temperature is the characteristic of thermal equilibrium, and so this observation is naturally explained if different regions of the sky have been able to interact and move towards thermal equilibrium, before the time of decoupling. However, the comoving horizon at the time of decoupling was about 0.250 Mpc, which corresponds to an angular distance of $\sim 1°$. This means that regions that, according to the Standard Big Bang model, would have been causally connected $\sim 380\,000$ years after the Big Bang, subtend now an angle of about $1°$ in the sky. The model does not provide any mechanism which can explain a causally connection between regions larger than this angular dimensions and, as a consequence, how they can be so homogenous in their properties as the CMB observations suggest.

1.4.3 The monopole problem

According to the GUT, at early times the fundamental forces were combined in one. As the Universe cooled down, the breaking of symmetries separated the forces in the form we see them today. According to the theory, this process should have been produced a consistent number of *topological defects*, such as *magnetic monopoles*, which, however, have never been observed.

1.4.4 The origins of structures problem

The framework of the Big Bang model assumes the homogeneity of the Universe at large scales (> 100 Mpc). The structures we observe at smaller scales are the results of the gravitational collapse seeded by some initial perturbations. These initial conditions are an assumption of the Standard Model, which does not provide a natural explanation for their presence.

1.5 The Inflationary Paradigm

Alan Guth first proposed *inflation* in 1981 as a solution of all the problems listed above (Guth, 1981). The basic idea of inflation is that there was a limited period, early in the history of our Universe, were the expansion was accelerating. That is, an epoch when $\ddot{a} > 0$. Friedmann's acceleration equation 1.8 implies that:

$$P < -\frac{\rho}{3}. \tag{1.34}$$

Since the energy density is always positive, pressure must be negative, meaning that whatever it is that drives inflation is not ordinary matter or radiation. The simplest example of inflationary expansion is a Universe temporarily dominated by a cosmological constant Λ, for which $P = -\rho$. The Friedmann's equation in this case becomes:

$$\left(\frac{\dot{a}}{a}\right)^2 = \frac{\Lambda}{3}, \tag{1.35}$$

which means that during the inflationary phase, the scale factor grew exponentially with time:

$$a(t) \propto e^{H_i(t-t_i)}, \tag{1.36}$$

where $H_i = \sqrt{\Lambda/3}$ and t_i is the time inflation starts. After some amount of time, inflation came to an end and the Universe reverted to its former state of radiation-dominated expansion, as shown in Fig.1.11.

We can easily see how the inflationary paradigm solves the flatness problem, by recalling equation 1.26:

$$|\Omega_{\text{tot}}(t) - 1| = \frac{|k|}{a^2(t)H^2(t)}.$$

The problem was that this quantity always increases with time, forcing Ω_{tot} away from one. Inflation reveres this state of things. Since $H(t) = H_i = \text{const}$ and $a(t) \propto \exp(H_i t)$, we get:

$$|\Omega_{\text{tot}}(t) - 1| \propto e^{-2H_i t}, \tag{1.37}$$

which means that during the inflationary period the difference between Ω_{tot} and 1 falls exponentially with time. In order to match the current observations of $|1 - \Omega_{\text{tot}}, 0| \leq 0.005$, inflation must have been a dramatic event. Assuming that it started during the GUT era ($t_i \sim 10^{-36}\,$s), inflation should have increased the dimensions of the Universe by at least a factor $a(t_f)/a(t_i) \sim 10^{26}$ in just about 10^{-34} seconds.

This enourmous expansion is able to expand a patch of Universe, small enough to achieve thermalization before inflation, to be much larger than the size of our presently observable Universe. This means that regions that today appears causally disconnected to us, were actually in causal contact before the inflationary era. This explain the observed homogeneity and isotropy of the Universe, solving the horizon problem.

Finally, if magnetic monopoles were created before or during inflation, then the number density of monopoles was diluted to an undetectably low level ($\approx 5 \times 10^{-16}\text{Mpc}^{-3}$).

1.5.1 The physics of Inflation

Summarizing, inflation is a perfect candidate to explain some of the otherwise puzzling aspects of the Universe. It is yet a very unfamiliar physical phenomenon: within a fraction of second the Universe grows exponentially at an accelerating rate. What triggers inflation? and (just as important) what turns it off?

The easiest way to produce inflation is through a scalar field $\phi(t)$ [6], called *inflaton*, with an associated potential energy $V(\phi)$.

$$T_{\mu\nu} = \partial_\mu \phi \partial_\nu \phi - g_{\mu\nu} \left[\frac{1}{2} g^{\alpha\beta} \partial_\alpha \phi \partial_\beta \phi - V(\phi) \right]. \tag{1.38}$$

---

[6]We are restricting to the case of a homogeneous field $\phi(\vec{r}, t) \equiv \phi(t)$
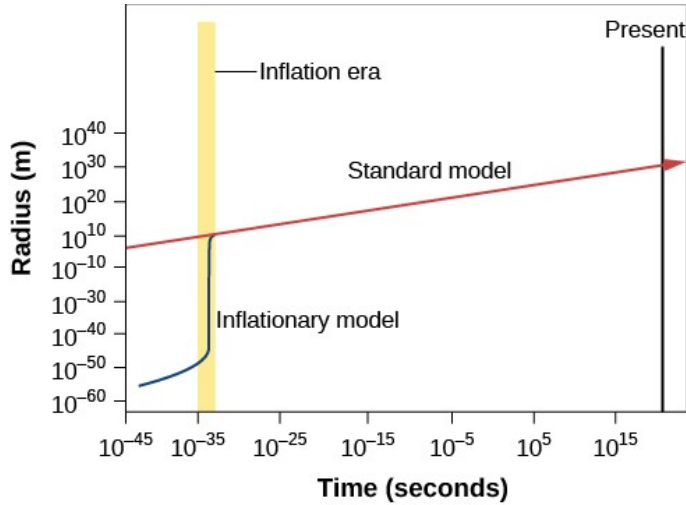
Figure 1.11: The size of the Universe as a function of time according to the standard Big Bang model (red line) and to the inflationary paradigm (blue line). Inflation causes an exponential expansion of the Universe from about 10^{-36} s to 10^{-34} s after the Big Bang. After the end of the inflation era, the Universe continued to expand at as slower rate, reconnecting to the standard model predictions.

Comparing this with equation 1.6, one finds that the scalar field $\phi(t)$ behaves like a perfect fluid with:

$$\rho_\phi = \frac{\dot{\phi}^2}{2} + V(\phi), \tag{1.39}$$

$$P_\phi = \frac{\dot{\phi}^2}{2} - V(\phi). \tag{1.40}$$

If the kinetic energy of the scalar field is sufficiently smaller than the potential energy (*slow roll condition*):

$$\dot{\phi}^2 \ll V(\phi), \tag{1.41}$$

then the inflaton acts like a cosmological constant, with:

$$\rho_\phi \approx -P_\phi \approx V(\phi). \tag{1.42}$$

Thus, the inflaton field can drive exponential inflation if there is a temporary period when its rate of change $\dot{\phi}$ is small and its potential $V(\phi)$ high enough to dominate the energy density of the Universe. In order for this period to last sufficiently long to solve the flatess and horizon problems,

Figure 1.12: Schematic illustration of an inflationary potential. In the slow-roll
scenario, an accelerated expansion of the Universe occurs when the
inflaton rolls slowly along its potential. After inflation ends, the
inflaton oscillates around the minimum of its potential, and its energy
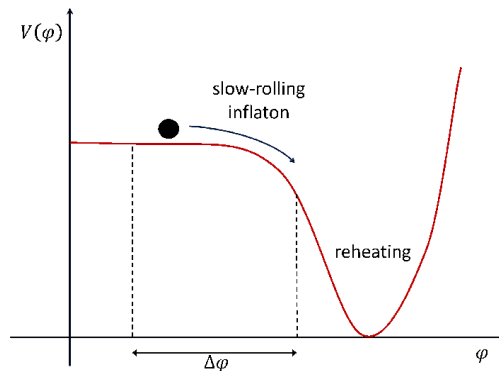is converted into particles (reheating).

we also need the second derivative of ϕ to be small enough ($|\ddot{\phi}| \ll |3H\dot{\phi}|$).
In other words, we need a potential with a gentle slope.

As a concrete example of a potential $V(\phi)$ that can give rise to inflation,
consider the potential shown in Figure 1.12. The scalar field ϕ starts on
a "plateau" of the potential, where $V(\phi) \approx \text{const}$. It is in this state that
inflation can take place. This state, however, cannot be a truly stable state,
otherwise the inflation would never end. It is instead a *metastable false
vacuum state* from which the inflaton field slowly rolls away, going towards
the true vacuum state, where $V = 0$. Inflation stops when the kinetic
energy of the field has grown enough to make the slow-roll conditions no
more satisfied. When the inflaton reaches the minimum of the potential, its
energy is converted into photons and other relativistic particles, which *reheat*
the Universe after the precipitous drop in temperature caused by inflation
(Bassett, Tsujikawa, and Wands, 2006). This *reheating* phase brings back the
Universe in the hot and dense state and, from that moment on, its evolution
continues following the Standard Cosmological Model [7]. The duration and
extent of inflation depends on the exact shape of the potential $V(\phi)$ and
on the initial and final values of the field ϕ. There are several possible
potential shapes that satisfy the slow-roll conditions and allow an expansion
of $a(t_f)/a(t_i) \sim 10^{26}$ (the minimum to solve the flatness problem); as a
consequence there are several inflationary theories.

---

[7]Inflation ensures that we live in a Universe with negligibly low density of magnetic
monopoles, while reheating phase ensures that we don't live in a Universe with a negligibly
low density of photons.

1.5.2 Inflation and cosmological perturbations

As we have seen in previous sections, the inflationary paradigm solves the horizon, flatness and monopole problems. In addition, it naturally explains the inhomogeneities in the Universe, observed in the CMB anisotropies, that seed structure formation. It is natural to introduce quantum fluctuations of the inflaton field ϕ, which appears as first-order perturbations:

$$\phi(\vec{r}, t) = \phi^0(t) + \delta\phi(\vec{r}, t) \tag{1.43}$$

Being ϕ the dominant component of the Universe in this phase, perturbations of the inflaton causes perturbations of the energy-momentum tensor and of the metric. In particular, a generic perturbation of the metric is made of scalar, vector and tensor perturbations. If the perturbations are small, they evolve independently and can therefore be treated separately. Fluctuations are created on all length scales with a spectrum of wavenumbers k. The exponential growth of the scale factor during inflation caused the quantum fluctuations to be stretched to macroscopic scales. While the horizon grew at the speed of light, physical scales expanded exponentially in time and the perturbations exited the horizon. Since physics does not affect the evolution of fluctuations when their wavelength is outside the horizon, their amplitude was frozen. At the later stages of radiation- and matter-domination, these fluctuations eventually re-entered the horizon, and thus set the initial conditions for structure formation[8]. While vector perturbations decayed with the expansion of the Universe (Baumann, 2009), scalar perturbations generated the energy density fluctuations that the standard Big Bang model was not able to explain, which eventually evolved in baryonic and dark matter density fluctuations, seeding the formation of stars, galaxies and galaxy clusters. Tensor perturbations, on the other hands, propagated as primordial gravitational waves. The presence of this gravitational waves background, in particular, is considered to be a "smoking gun" for inflation The amplitude of tensor perturbations is often expressed in terms of the *tensor-to-scalar ratio*:

$$r \equiv \frac{\Delta_t}{\Delta_s}, \tag{1.44}$$

where Δ_t and Δ_s are the power spectra of the tensor and scalar perturbations respectively [9]. Proving the existence of gravitational waves in the primordial Universe would be a solid proof of the validity of the inflationary paradigm. However, the wavelength expected for these gravitational waves is of the order of the Hubble radius (c/H_0), which makes them too long to be

---

[8]For a more detailed discussion, see Dodelson, 2003

[9]Evaluated at some scale k, usually the "statistical center" of the range explored by the data

detectable by current gravitational waves interferometers. Fortunately, there might be another way: if the amplitude of the tensor perturbations (and consequently of the primordial gravitational waves) was high enough, it may have left a trace in the polarization pattern of the Cosmic Microwave Background. Measuring the imprint of primordial gravitational waves on the CMB polarization pattern would provide a strong confirmation of the inflation theory. The study of the polarization of the CMB, in particular its B-modes, has thus become one of the most active fields in modern observational cosmology. However, probing inflation through CMB is a real technological challenge: every inflationary theory predicts a different, but in general very small, value for r. This means looking for a signal $< 1\,\mu$K, thing that requires very sensitive instruments and a very good control of systematics. As we will see in Section 1.6.3, no experiment has been able to measure the value of the tensor-to-scalar ratio so far. We currently have just upper bounds.

1.6   CMB polarization

We expect the CMB to be partially linearly polarized, thanks to Thomson scattering events during the recombination era. Thomson scattering is the elastic scattering of electromagnetic radiation by a free charged particle, under the condition that the photon energy is much smaller than the mass energy of the particle ($h\nu \ll mc^2$). Its cross section σ per solid angle Ω depends on polarization as:

$$\frac{d\sigma_T}{d\Omega} \propto |\hat{\epsilon}' \cdot \hat{\epsilon}|^2, \qquad (1.45)$$

where $\hat{\epsilon}'$ and $\hat{\epsilon}$ are the incident and scattered polarization directions respectively. The outcoming radiation is thus linearly polarized with polarization parallel to the incident one. As the electromagnetic field of a photon is always orthogonal to its heading, only the component of the incoming polarization orthogonal to the outbound direction survives the scattering. The total radiation leaving any point in the plasma in any given direction is the sum of contributions from photons incident from all directions. If the incident radiation field is isotropic (i.e., all photons from all directions having the same energy), the two orthogonal polarization states (from orthogonal incident directions) surviving the scattering have the same intensity and thus the scattered radiation remains unpolarized.

There is however a peculiar spatial configuration, the *quadrupolar anisotropy*, which is able to produce a net linear polarization: this happens when the radiation field around an electron varies in intensity at an angle of 90%, as shown in Figure 1.13. Mathematically, quadrupoles are defined as spherical

harmonics Y_{lm} with $l = 2$. There are therefore 3 possibles quadrupole configurations, corresponding to $m = 0, \pm1, \pm2$.

Quadrupole anisotropy could have been generated by perturbations in the primordial plasma and, in particular, by three different kinds of perturbations generated by distinct physical processes (see Hu and White, 1997 for a detailed discussion):

- *Scalar perturbations*: or simply density perturbations in the cosmological fluid, can be caused by adiabatic pressure oscillations (sound waves). They generates a $m = 0$ quadrupole anisotropy.

- *Vector perturbations*: represent vortices in velocity fields, which create a spacially varying Doppler shift in the radiation that in turn produces quadrupoles with $m = \pm1$. As mentioned in Section 1.5.2, however, vorticity is damped by the expansion of the Universe, ad so vector perturbations are not expected to have left an imprint on CMB at detectable level.

- *Tensor perturbations*: can be generated only by perturbations of the metric in the primordial Universe, that is primordial gravitational waves. Gravitational waves distort space in a way that generates quadrupole anisotropies with $m = \pm2$.

It is important to notice that polarization can only be produced if the decoupling takes place in a short time, but not too short. If decoupling were an instantaneous process, there were no time for photons to scatter on electrons and produce polarization. On the other hand, if decoupling were too slow, quadrupolar anisotropies would smooth out while reaching thermal equilibrium, and thus polarization would not occurr. Given the duration of decoupling, roughly 10% of the CMB signal should be polarized. Typically, this means a polarized signal $\lesssim 1\,\mu\text{K}$.

1.6.1 Measuring polarization: the Stokes parameters

Polarization of electromagnetic radiation is usually described in terms of *Stokes parameters*. Let us consider, without loss of generality, a plane electromagnetic wave propagating along the $\hat{z}$ direction. The electric field $\vec{E}(z, t)$ can be written as:

$$\vec{E}(z, t) = E_x(z, t)\hat{x} + E_y(z, t)\hat{y}, \tag{1.46}$$

where

$$E_x(z, t) = |E_x| \cos(kz - \omega t + \phi_x), \qquad E_y(z, t) = |E_y| \cos(kz - \omega t + \phi_y). \tag{1.47}$$
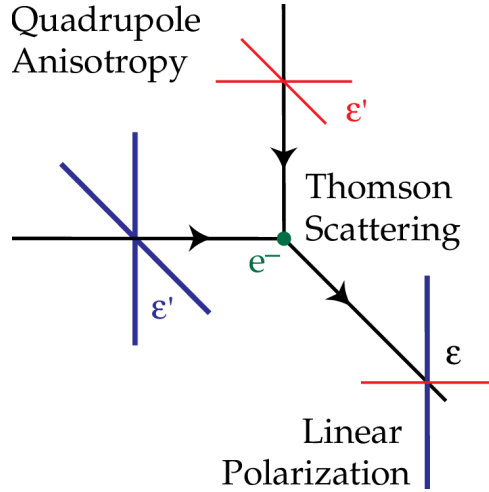
Figure 1.13: Local quadrupole anisotropies causes the linear polarization of the CMB. In this example, unpolarized light (i.e. light with equal amounts of all tipe of polarization) scatters on an electron. The outgoig radiation inherits the horizontal polarization component from the vertically incident radiation and vice versa for the horizontal radiation. If the horizontally and vertically incident radiation have different intensities (quadrupolar anisotropy), the outgoing radiation will be linearly polarized.

The four Stokes parameters are defined as:

$$I \equiv \langle |E_x|^2 \rangle + \langle |E_y|^2 \rangle, \tag{1.48}$$

$$Q \equiv \langle |E_x|^2 \rangle - \langle |E_y|^2 \rangle, \tag{1.49}$$

$$U \equiv \langle 2Re(E_x E_y^*) \rangle = \langle 2|E_x||E_y|cos(\phi_x - \phi_y) \rangle, \tag{1.50}$$

$$V \equiv \langle 2Im(E_x E_y^*) \rangle = \langle 2|E_x||E_y|sin(\phi_x - \phi_y) \rangle. \tag{1.51}$$

where the average $\langle \cdot \rangle$ is calculated over a time longer than the the wave period. The parameter I represents the total intensity of radiation, while the Q, U parameters describe linear polarization. Finally, V quantifies the amount of circular polarization. Unpolarized light will have $I > 0$ but $Q = U = V = 0$, reflecting that no polarization type predominates. Figure 1.15 shows examples of the Stokes parameters in degenerate states. Because of the properties of Thomson scattering, the CMB is not expected to have circular polarization, which means that measuring Q and U parameters only is enough to completely describe CMB polarization. For this reason, we are going to ignore the V parameter from now on.
While I is a scalar quantity and does not depend on the reference frame, Q
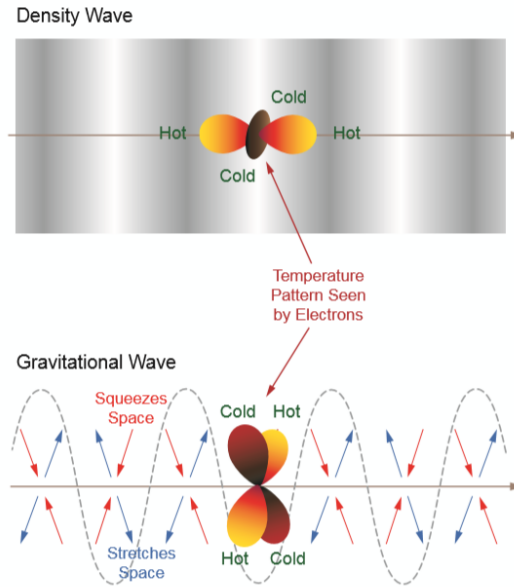
Figure 1.14: Illustration of the local quadrupole anisotropy induced a scalar (density waves) and tensor (gravitational waves) perturbations. On the top, we show a density wave on the last scattering surface, with peaks in dark gray and troughs in white. Considering an electron in in a cold spot, there is a quadrupolar anisotropy with $m = 0$ in the of the radiation interacting with it via Thomson scattering. The radiation coming from above and from below has, on average, lower intensity with respect to the radiation coming from left or from right (i.e. from overdensities). On the bottom, a gravitational wave travels across a space region. In this case the intensity of the incident radiation shows an quadrupole anisotropy with $m = 2$ (Collaboration et al., 2018)

and U depends on the chosen coordinate system. Under a rotation by a an angle θ, they transform according to the equation:

$$\begin{pmatrix} Q' \\ U' \end{pmatrix} = \begin{pmatrix} \cos 2\theta & \sin 2\theta \\ -\sin 2\theta & \cos 2\theta \end{pmatrix} \begin{pmatrix} Q \\ U \end{pmatrix}. \tag{1.52}$$

However, the quantity $P := \sqrt{Q^2 + U^2}$, which defines the total polarization intensity of the electromagnetic wave, is invariant. In each point of the sky, the value of the polarimeter P together with the polarization angle $\alpha = \arctan(U/Q)/2$ specifies the CMB polarization pattern.
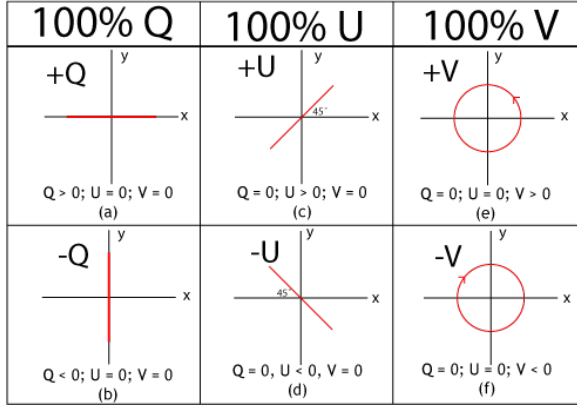
Figure 1.15: Illustration of the linear polarization Stokes parameters Q U and V. While Q and U quantifies the linear polarization of the radiation, V quantifies its circular polarization.

1.6.2 E-modes and B-modes

All the discussion presented in Section 1.3.1 is valid for the decomposition of a *scalar* field on a sphere (this is the case of CMB temperature field). However, that approach can be generalized to vector and tensor fields, so that we can actually decompose the CMB polarization into spherical harmonics as well and visualize it on the sphere. The quantity:

$$(Q \pm iU)(\theta, \phi) \tag{1.53}$$

trasforms as a spin-2 tensor under a rotation by an angle ψ:

$$(Q \pm iU)(\theta, \phi) \rightarrow (Q \pm iU)'(\theta, \phi) = e^{\mp 2i\psi}(Q \pm iU)(\theta, \phi). \tag{1.54}$$

We can expand this quantity in therms of spin-2 spherical harmonics $Y_{lm}^{\pm 2}$ (Zaldarriaga and Seljak, 1997):

$$(Q + iU)(\theta\phi) = \sum_{l,m} a_{2,lm} Y_{2,lm}(\theta, \phi), \tag{1.55}$$

$$(Q - iU)(\theta\phi) = \sum_{l,m} a_{-2,lm} Y_{-2,lm}(\theta, \phi). \tag{1.56}$$

Instead of $a_{2,lm}$ and $a_{-2,lm}$, we can conveniently introduce their linear combinations:

$$a_{lm}^E \equiv -\frac{a_{2,lm} + a_{-2,lm}}{2}, \qquad a_{lm}^B \equiv \frac{i(a_{2,lm} - a_{-2,lm})}{2}. \tag{1.57}$$

Figure 1.16: E-modes and B-modes polarization pattern in the sky. We should imagine radiation emitted towards us, orthogonal to the page. The direction of black bars indicates the polarization direction, while t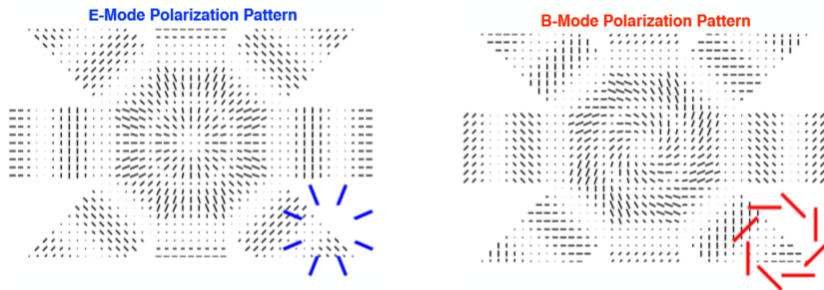heir lenght indicates the intensity of polarization. E-modes shows a curl-free pattern on the sky, always tangential or radial around a given point, while B-modes show a characteristic vortex pattern (Collaboration et al., 2018)

These two combinations behave dfferently under parity transformation: while E remains unchanged B changes the sign, in analogy with electric and magnetic field. Starting from these coefficients we can now define two quantities:

$$E(\theta\phi) = \sum_{l,m} \left[\frac{(l+2)!}{(l-2)!}\right]^{1/2} a_{lm}^E Y_{lm}(\theta, \phi), \tag{1.58}$$

$$B(\theta\phi) = \sum_{l,m} \left[\frac{(l+2)!}{(l-2)!}\right]^{1/2} a_{lm}^B Y_{lm}(\theta, \phi), \tag{1.59}$$

which represent the so-called *E-modes* and *B-modes* of the CMB and completely specify the statistical properties of its linear polarization field. These quantities are scalar (spin-0[10]) as the CMB temperature; and, therefore, we can easily visualize them on the sphere and build power spectra in the same manner. E and B-modes shows different patterns in the sky, as shown in Fig. 1.16: E-modes shows a radial or tangential pattern, while B-modes shows a curly pattern.

As done with the temperature field, to statistically analyze the properties of CMB polarization, we can define power spectra also for E-modes and B-modes. Equation 1.31 can be generalized in the following way:

---

[10]The factor $\left[\frac{(l+2)!}{(l-2)!}\right]^{1/2}$ comes from the usage of the spin raising and lowering operators, which turn a spin-2 element into a spin-0 element (Zaldarriaga and Seljak, 1997))

$$C_l^{\alpha\beta} = \frac{1}{2l+1} \sum_{m=-l}^{l} a_{lm}^{\alpha}(a_{lm}^{\beta})^*, \qquad (1.60)$$

where α and β can be T, E, or B. Power spectra with $\alpha = \beta$ (i.e. C_l^{TT}, C_l^{EE}, C_l^{BB}) are called *auto-spectra* and measure the power in temperature, E or B modes. If $\alpha \neq \beta$, they are called *cross-correlation spectra*, which measure the amount of correlation betweeen two modes. For example, if C_l^{TE} is large at a certain angular scale l it means that there is a significant amount of power both in temperature and in E-mode polarization. For simmetry reasons, primordial cross-spectra C_l^{EB} and C_l^{TB} are expected to be consistent with zero at any angular scale l (Hu and White, 1997)[11]

It can be demonstrated that scalar perturbations at the epoch of recombination generate both temperature and polarization anisotropies. Nevertheless, the latter are generated only in terms of E-modes. Tensor perturbations (i.e. gravitational waves), on the contrary, produce both E-modes (in lower amount with respect to scalar perturbations) and B-modes. For this reason, the detection of primordial B-modes in the CMB radiation would provide an indirect proof of the presence of gravitational waves in the primordial plasma, and therefore a strong evidence in favour of the inflationary paradigm. Unfortunately, this measurement is nothing close to easy. Figure 1.17 shows theoretical predictions for TT, EE and BB power spectra. The first thing we can notice is that polarization spectra are fainter than the temperature spectrum. As mentioned before, in fact, the duration of the decoupling phase allowed a 10% polarization of the CMB, resulting in an expected signal $\lesssim 1\mu$K. Moreover, the amount of power associated with B-modes is significantly smaller than the power in E-modes.

At very large angular scales, we can see the so-called *reionization bump* in both polarization spectra. As mentioned in Section 1.2.2, CMB photons interacted again via Thomson scattering with free electrons generated in the formation processes of the first stars. This process has contributed to polarize the CMB on large scales, as the horizon was larger with respect to the epoch of recombination. The amplitude of E and B-modes spectra at $l \lesssim 10$ depends on the value of the optical depth of Thomson scattering τ and can be studied to get information on the reionization era.

The B-modes signal strongly depends on the amplitude of the primordial gravitational waves which generates them. The tensor-to-scalar ratio, introduced in equation 1.44, is thus a good indicator of how much the B-modes

---

[11]This is true only for *primordial* polarization patterns. Polarization produced by Galactic emissions can have non-zero C_l^{EB} and C_l^{TB}.

spectrum is suppressed with respect to the E-modes one (which instead is in greatest part produced by scalar perturbations).

Looking at the figure, we can also notice another problem that complicates the search for B-modes: at small angular scales B-modes are principally not of primordial origin, but instead generated by gravitational lensing. The presence of massive structures in out Universe, such a galaxy clusters, can deviate the path of CMB photons travelling from the last scattering surface toward us, generating secondary anisotropies and distorting the shape of the CMB power spectrum. In particular, gravitational lensing can reshape the polarization pattern of the CMB, commuting E-modes in B-modes. This effect dominates the B-modes power spectrum at small angular scales ($l \gtrsim 100$), with a peak at arcominute scales (~ 1000). The lensing spectrum makes it very difficult to detect primordial-B modes beyond a certain multiple, with a more and more dramatic effect as r gets small. It is clear that to be able to detect primordial B-modes we need experiments looking at large angular scales.

1.6.3   Status of observations

In the last twenty years many experiments have built with the purpose of detecting and measuring the polarization signal of the CMB, pushing the sensitivity of the instruments as further as possible. The first detection of E-modes was made in 2000 by the DASI experiment (Kovac et al., 2002), which confirmed the presence of polarization anisotropies at a level of 10^{-6}, as expected. But it was the CBI experiment that first obtained the E-modes spectrum (Readhead, 2004). Since then, several other experiments were able to detect and characterize the E-modes spectrum and the cross-correlation spectrum between temperature and E-modes (C_l^{TE}) on many angular scales, getting important information on the evolution of the Universe. So far, the most accurate measurement of the E-modes spectrum is the one obtained by the Planck satellite, shown in Figure 1.18. Planck has also provided the first full-sky map of the E-modes polarization pattern. From the joint analysis of the Planck temperature and E-modes power spectra, it has been possible to obtain the value of τ as reported in Section 1.3.1 and a measure of the redshift of reionization $z_{re} = 7.68 \pm 0.79$ (68% C.L.).

While the E-modes spectrum has been extensively studied, no experiment so far has been able to detect the signal of primordial B-modes. In the absence of a detection, upper limits on the B-modes signal have been put according to the sensitivity of the various experiments, as shown in Figure 1.19. Ground experiments as POLARBEAR (Keating and PolarBEAR collaboration, 2011), SPTPol (Benson and SPT collaboration, 2014) and ACT-Pol (ACTPol collaboration, 2016a), however, have been able to measure the
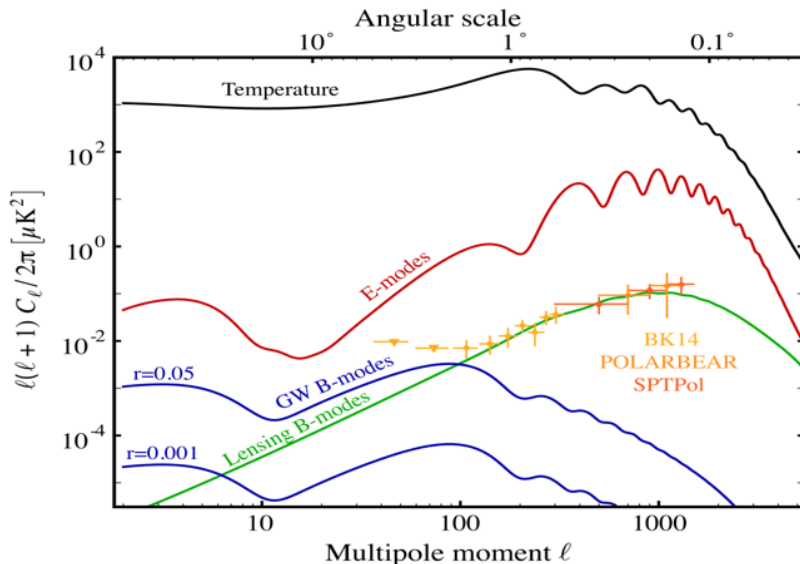
Figure 1.17: Theoretical predictions for the temperature (black), E-mode (red), and tensor B-mode (blue) power spectra (Abazajian et al., 2016). Primordial B-mode spectra are shown for two representative values of the tensor-to-scalar ratio: $r = 0.001$ and $r = 0.05$. Also shown are expected values for the contribution to B modes from gravitationally lensed E modes (green). Since the E-modes have been mostly generated by density waves in the primordial plasma, they show acoustic oscillations similarly to the temperature spectrum (although with fainter peaks and with $\pi/2$ phase-shift). Current measurements of the B-mode spectrum are shown for a few experiments: although the lensing spectrum has been measured, no detection of the primordial spectrum due to gravitational waves has been found so far.

signal of B-modes due to gravitational lensing, at small angular scales. In 2014 the BICEP2 experiment, located at the South Pole, announced the first detection of primordial B-modes at high significance (Ade et al., 2014). A subsequent check with Planck data in the same sky region, however, showed that the B-modes signal detected by BICEP2 was actually polarized emission from interstellar dust. The best constraint so far comes from a joint analysis of Bicep/Keck/WMAP/Planck data (Ade, 2018), which gives:

$$r < 0.07 \qquad (95\% \, \text{confidence level}) \tag{1.61}$$

which implies a polarization signal of less than 10^{-7} K. To push forward the search for primordial B-modes, it is crucial to build instruments with extremely high sensitivity, as well as develop software techniques to disentangle the signal of primordial origin from the signal produced by galactic
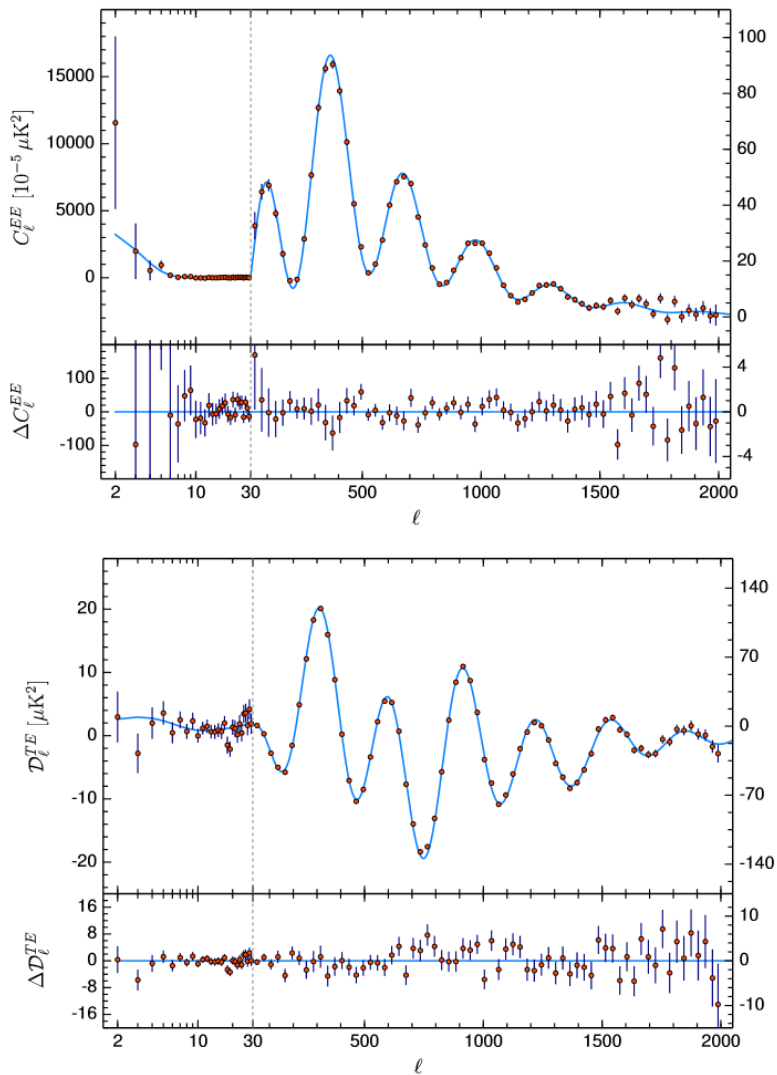
Figure 1.18: EE (bottom) and TE (top) power spectra in terms of $D_l \equiv l(l+1)C_l/2\pi$ obtained by the Planck satellite(Planck Collaboration et al., 2018). The ΛCDM fit is plotted in light blue. Residuals with respect to this model are shown in the lower panels. The vertical scale changes at $l = 30$, where the horizontal axis switches from logarithmic to linear.
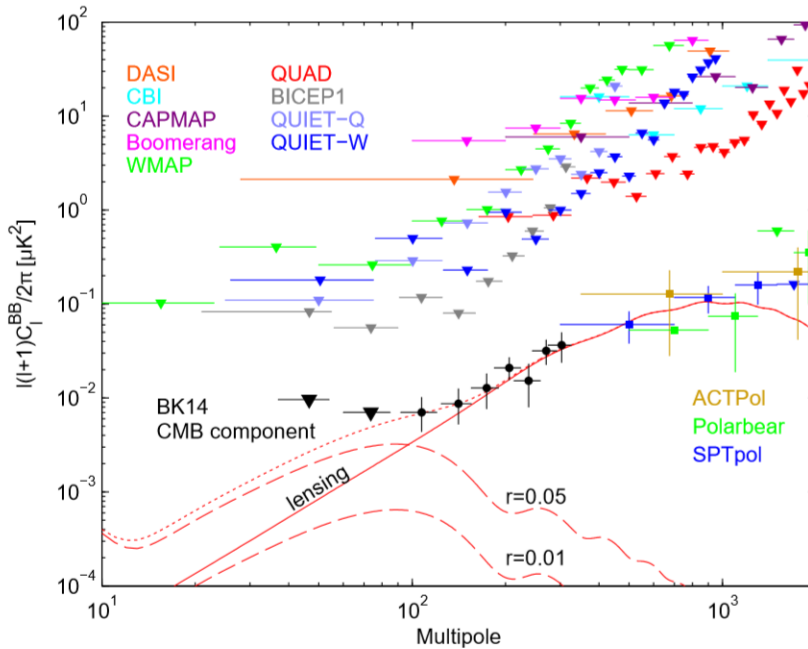
Figure 1.19: B-modes power spectra measured by several experiments up to March 2018. The red lines show the theoretical predictions for the B-modes signal (dashed) for r = 0.05 and r = 0.01, as well as the lensing signal (solid). The dots show detected signals, and triangles are 95% upper limits. The black points show the B-mode spectrum from Bicep/Keck data, combined with WMAP and Planck, after removing galactic foreground contamination. Other data points from telescopes focusing on the small scale lensing signal are shown (Collaboration et al., 2018).

foregrounds, ad to control systematic effects. In the next chapter, we will breafly overview the main experimental challenges that experiments face in trying to measure the B-modes polarization of the CMB.

Chapter 2

Experimental challenges in observing CMB polarization

2.1 Polarized foregrounds

We have seen in the previous Chapter that the Cosmic Microwave Background is the most distant source of electromagnetic radiation in our Universe, at a redshift $z \sim 1100$. The CMB is therefore a backlight to all other sources of radiation between the surface of last scattering and the observer, which contaminate the primordial signal. These sources of contamination are called *CMB foregrounds*. One of the most difficult tasks in measuring the CMB and its anisotropies is the proper disentanglement between the signal of cosmological origin and foregrounds, done during data analysis through *component separations* techniques (see Section 5.1).

The foregrounds issue is particularly tough for polarized signals. Even though it is observationally evident that, in total intensity, CMB dominates at high Galactic latitudes over foreground emissions (mostly concentrated on the Galactic plane), this is not true in the case of polarization. This makes the foreground emission a source of contamination even far from the Galactic plane.

The difficulty of dealing with foregrounds, particularly in polarization, has been highlighted by the announced detection of primordial B-modes by the BICEP2 collaboration, which has been later shown to be fully compatible with a thermal dust-only origin (BICEP2/Keck Collaboration and Planck Collaboration, 2015).

In the following, we briefly review the main sources of foreground contamination for CMB polarization and their basics characteristics.

2.1.1 Synchrotron emission

Synchrotron radiation results from the acceleration that cosmic rays electrons undergo in the Galactic magnetic field. The intensity and spectrum of this emission depend on the magnetic field strengh and on cosmic ray energy, and therefore they show significant spatial variations on the sky. The energy distribution of cosmic rays electrons can be well described by a power law, $N(E) \propto E^{-p}$, over a wide range of frequencies. With this approximation, together with the assumption of uniform magnetic field, the frequency spectrum of the synchrotron emission can be described by a power law as well:

$$T(\nu) \propto \nu^{\beta_s} \qquad \text{where} \qquad \beta_s = -\frac{p+3}{2}, \tag{2.1}$$

where T is the brightness temperature. The resulting emission is also partially polarized with linear polarization fraction of:

$$f_s = \frac{p+1}{1+7/3} \tag{2.2}$$

and aligned perpendicularly to the magnetic field (Rybicki and Lightman, 1979). At frequencies $\lesssim 100\,\text{GHz}$, Galactic synchrotron dominates the microwave sky, and thus most of the information we have about it comes from low-frequency radio surveys. Observations tell us that a typical value of the spectral index is $\beta_s \sim -3$ at $\sim 10\,\text{GHz}$ frequencies, with a typical variations across the sky of $\Delta\beta \approx \pm 0.2$ (Dickinson, 2016).

The best full-sky map of polarized synchrotron emission to date comes from WMAP and Planck experiments. In their lowest frequency bands (22, 33 GHz fo WMAP and 30 GHz for Planck) the synchrotron radiation dominates the polarized maps, allowing the component separation algorithm to extract precise maps of the synchrotron emission all over the sky. The top panel of Figure 2.1 shows the polarized synchrotron map at the frequency of 30 GHz measured by Planck, plotted in terms of polarization amplitude $P = \sqrt{Q^2 + U^2}$. From this map it is possible to appreciate the tortuous morphology of the synchrotron emission, reflecting the shape of the Galactic magnetic field. We can also see that the polarized emission significanty extends even at very high Galactic latitudes, following magnetic fields that elongate perpendicularly to the Galactic plane.

A spectral index of $\beta_s \sim -3$ implies that the polarization fraction of synchrotron radiation f_s can, in principle, be as high as 75%, in a uniform

magnetic field. In practice, variability of the field orientation along the line-of-sight and non-regular fields reduces the degree of polarization observed. The bottom panel of Figure 2.1 (obtained from WMAP nine-years data) shows that the mean polarization fraction rises from $\sim 5\%$ near the Galactic plane up to $\sim 20\%$ at high Galactic latitudes $|b| > 50°$. The larger polarization degrees at high Galactic latitudes are mostly attributed to local structures, namely the Fan region and the North Galactic Spur (which have $f_s > 30\%$), while the decline of polarization degree towards low Galactic latitudes could be interpreted as a depolarization effect due to the superposition of emissions with different polarization angles. We underline that, even though polarization degree at low Galactic latitudes may be small, synchrotron emission is instrinsically strong there and these regions are not suitable for CMB observation anyway. The characterization of synchrotron polarization fraction is a tricky task: polarization can only be directly mapped at frequencies above a few GHz, due to the effect of Faraday rotation effect, but at high frequencies the intensity of synchrotron emission become difficult to disentangle due to the contributions of free-free and anomalous microwave emission.

2.1.2 Thermal dust emission

In the microwave sky at frequencies $\gtrsim 100\,\text{GHz}$, the thermal emission from interstellar dust dominates the foreground. Interstellar dust is mostly made of graphites, silicates and PAHs (Polycyclic Aromatic Hydrocarbons), and its thermal emission spectrum is well described by a modified black-body of the form:

$$I_\nu \propto \nu^{\beta_d} B_\nu(T_d), \qquad (2.3)$$

where $B_\nu(T_d)$ is the Planck spectrum (Ichiki, 2014). The temperature T_d is determined by the dust grains composition and shape, the interstellar radiation field (causing heating of the grains) and the efficiency of the grains in emitting far-infrared light (causing cooling).

Thermal dust emission can be significantly polarized. Elongated dust grains, in fact, emit preferentially along the longest axis (Lazarian and Finkbeiner, 2003). This, combined with the fact that alignment mechanisms tend to make the long grain axis perpendicular to the local magnetic field, generates linear polarization perpendicular to the Galactic magnetic field. The degree of alignment would vary according to the shape and size of dust grains, leading to a frequency-dependent polarization.

Planck, with its 353 GHz frequency channel, has permitted to obtain a full-sky map where the polarized emission of thermal dust dominates the observed signal, allowing the component separation algorithm to well isolate

Figure 2.1: *Top*: Polarized synchrotron map at 30 GHz in terms of polarization amplitude $P = \sqrt{Q^2 + U^2}$, smoothed to an angular resolution of 40 arcmin. Measured by Planck (Planck Collaboration, 2018). *Bottom*: synchrotron fractional polarization P/I, estimated from the WMAP nine-year analysis (Ichiki, 2014). The polarization fraction is 3-5% on the Galactic plane, increasing above 20% at high Galactic latitudes.
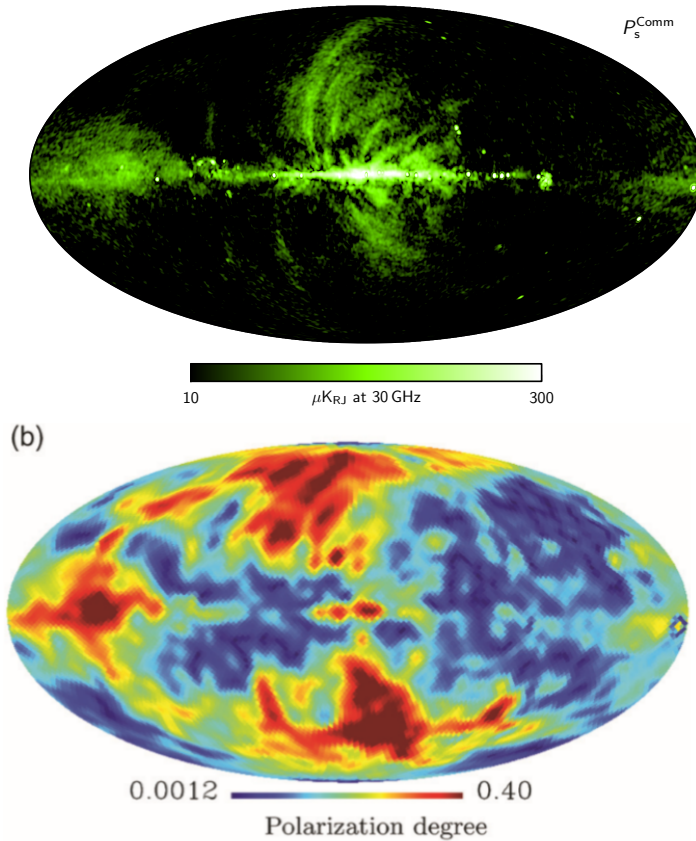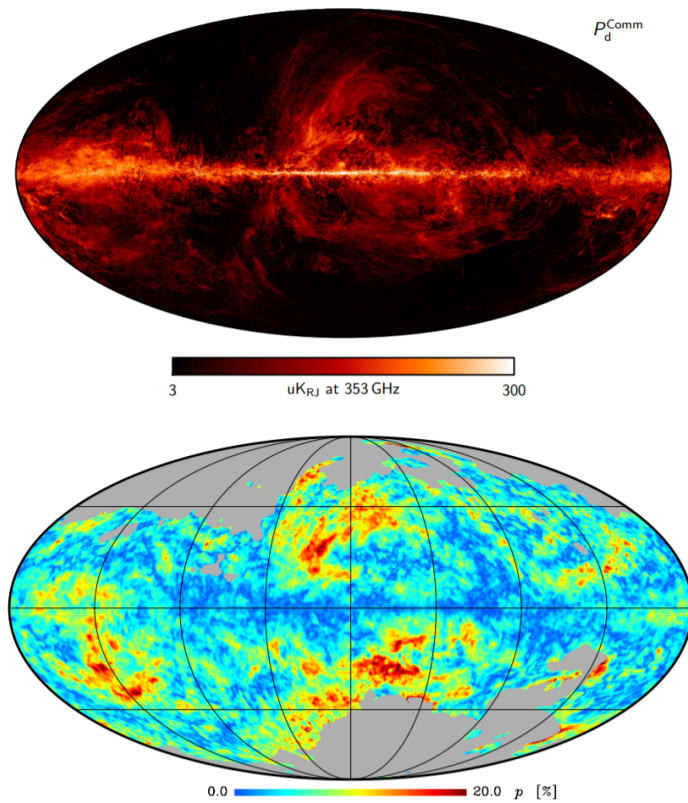
Figure 2.2: *Top*: Polarized dust map at $353\,\mathrm{GHz}$ in terms of polarization amplitude $P = \sqrt{Q^2 + U^2}$, smoothed to an angular resolution of $5\,\mathrm{arcmin}$. Measured by Planck (Planck Collaboration, 2018). *Bottom*: dust fractional polarization P/I at $353\,\mathrm{GHz}$, estimated from Planck data. The map is at $1°$ angular resolution on 79% of the sky (data are not shown in the grey areas where the dust emission is not dominant). The polarization fraction is 3-5% on the Galactic plane, increasing above 20% at high Galactic latitudes (Ade et al., 2015).

the dust contribution. The top panel of Figure 2.2 shows the polarization amplitude of the thermal dust at $353\,\mathrm{GHz}$, smoothed to an angular resolution of $5\,\mathrm{arcmin}$. As for the synchrotron maps, we can see that the thermal dust emission extends significantly even at high Galactic latitudes.

The bottom panel of Figure 2.2 shows the map of polarization fraction as measured by Planck. Similarly to synchrotron, the polarization fraction can reach up to 20% in some regions of the sky at intermediate latitudes, while on the Galactic plane the typical polarization fraction is of few percent, due to the effect of line-of-sight depolarization.

2.1.3   Lensing

Lensing can be considered a foreground contamination, but it is of a fairly different nature than those described above. Foregrounds like thermal dust and synchrotron emissions are caused by the presence of photons of non-cosmological origin in the electromagnetic radiation entering the optical system of an instrument. Lensing, instead, does not produce new photons, but it creates spurious polarization patters in the CMB radiation. The photons of the cosmic microwave background are deflected by the presence of large scale structures on their path from the last scattering surface to the observer. As mentioned in Section 1.6.2, this deflection can mix power between E and B modes, so that purely E-mode polarization pattern becomes a E/B pattern. In order to detect primordial B-mode polarization, it is necessary to clean the CMB polarization maps through a procedure called *delensing*, which exploits the information from large scale structures surveys to reconstruct a template of expected lensing B-modes and then uses it to disentangle the lensing contribution from data.

2.1.4   Possible other sources

An important foreground for the measurement of CMB temperature anisotropies is the free-free emission. This radiation, also known as thermal bremsstrahlung, arises from electron-ion scattering in ionised gas. Fortunately, free-free should not be a concern for polarization measurements, as it is intrinsically unpolarized.

The Anomalous Microwave Emission (AME) at 20-60 GHz could be another possible source of foreground. This emission, spatially correlated with interstellar dust, most probably arises from the electric dipole of very rapidly spinning extremely small (nanometer) dust grains, probably PAHs or silicates (Dickinson et al., 2018). Electric dipole emission from a single rotating grain is perfectly polarized. Thus, the spinning dust emission spectrum could be highly polarized if the ultrasmall grains, are substantially aligned. However, a recent theoretical work by Draine and Hensley (2016) suggests that quantum effects in ultrasmall grains suppress alignment mechanisms, thus leading to a negligible polarization level of $< 0.0001\%$ above 10 GHz. Observations agree with this prediction, with current upper limits of $< 1\%$. Even though AME does not appear to be a major concern for CMB polarization measurements, new and more precise measurements of its polarization level are necessary in view of next-generation ultra-high sensitivity CMB experiments (Remazeilles et al., 2016).

2.1.5   Impact of foregrounds on CMB observations

We have seen in previous paragraphs that the most worrisome foregrounds for CMB polarization measurements are synchrotron radiation and thermal dust emission. In terms of absolute intensity, foreground emission is mostly concentrated on the Galactic plane and therefore, for CMB temperature observations, one can use a Galactic mask to remove the annoying regions from the cosmological analysis. However, this is not the case for polarization measurements: Figures 2.1 and 2.2 show the structures of foreground emissions in polarization extend at high Galactic latitudes, implying that they can contaminate the CMB observations even when looking far away from the Galactic plane.

Figure 2.3 shows the level of foreground contamination in terms of RMS polarization amplitude as a function of frequency and compared with the CMB one. For each component, the full sky map (output of component separation) has been smoothed to $40\,\mathrm{arcmin}$ and the RMS of the pixels has been computed as a function of frequency, in order to measure the overall amount of anisotropies. While for temperature anisotropies there is a frequency window (50–110 GHz) where CMB signal dominates over Galactic foregrounds, this plot show that, in polarization, the foregrounds dominates over the CMB signal at all frequencies, with a minimum of the emission close to 70 GHz. For this reason, frequency channels monitoring foreground emission, on both low and high frequency, are mandatory for all the experiments aiming at observing CMB polarization, even more so if they aim to observe the primordial GWs signal.

In particular, synchrotron emission is currently the foreground known with more uncertainty and more measurements would be of extreme importance for current and future experiments. Low frequency ($\lesssim 30\,\mathrm{GHz}$) surveys, given the high brightness of the emission, can reach high signal-to-noise ratio, providing fundamental information about the characteristics of the signal itself, precious to build realistic sky models. However, data in this frequency range are currently lacking. New data at intermediate frequencies (30–50, GHz) would be also very useful in order to better characterize the synchrotron spectral energy distribution and better constrain spatial variation and frequency dependence (i.e. possibility of steepening and/or flattening of the spectrum) of the spectral index.

2.2   Experimental challenges

A second critical aspect for CMB observations is the technological challenge to reach extremely high sensitivities. This is true for observations of temperature anisotropies (which we recall are of the order of $10^{-5}\,K$), but
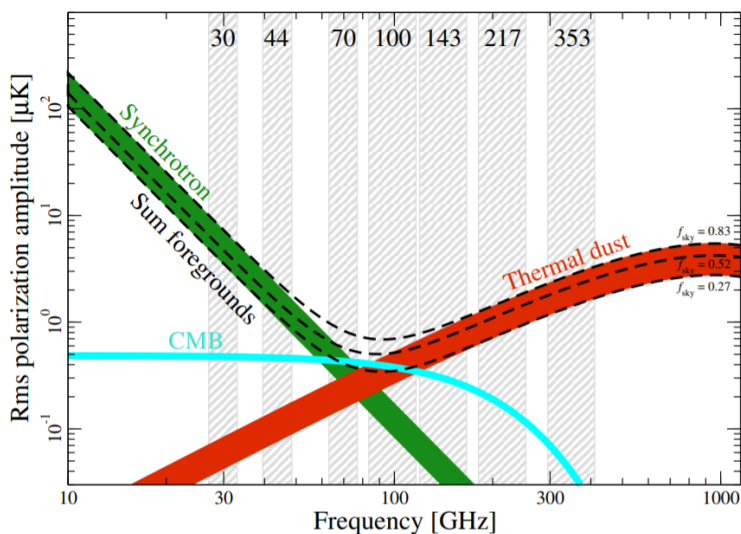
Figure 2.3: Polarization amplitude RMS as a function of frequency and astrophysical components. The green band indicates polarized synchrotron emission, and the red band indicates polarized thermal dust emission. The cyan curve shows the CMB RMS for a ΛCDM model with $\tau = 0.05$, and is strongly dominated by E-mode polarization. The RMS is calculated on maps at angular resolution of 40 arcmin on sky fractions of 27%, 52% and 83%. The widths of the synchrotron and thermal dust bands are defined by the largest and smallest sky coverages. Grey bars indicate Planck frequency channels (Planck Collaboration, 2018).

the situation is even more dramatic for observations of the polarized signal and in particular of the B-modes spectrum, with required sensitivities of fractions of μK per degree on the sky map. To reach such high sensitivity we need complex instruments composed by large arrays of detectors, together with a good control of systematic effects which can contaminate the measurements.

2.2.1   Dealing with noise

The sensitivity of a radio receiver is determined by the instrinsic statistical noise which affects the output of any detector. There can be external or internal sources of noise. Examples of external sources of noise include thermal signals from the antennas and the telescope structure, atmospheric noise, and so on. Internal noise is generated by components inside the receiver. This noise is the result of random processes such as the flow of charges in a device, or at a more fundamental level, the thermal vibrations

in any component at a temperature above absolute zero. All components of radio-receivers, passive (such as resistors), or active (such as amplifiers) generate noise. The noise in active components actually limits the useful operating range of the device.

We can identify two types of noise: *white* and *1/f* noise. White noise, also called uncorrelated noise, is a random signal having equal intensity at different frequencies, giving it a constant power spectral density (see the top panel of Figure 2.4):

$$S(\nu) = \sigma^2 \qquad [\mathrm{K}^2/\mathrm{Hz}] \tag{2.4}$$

White noise is easy to deal with, as it can usually be described using Gaussian statistics, with mean $\mu = 0$ and a characteristic σ. White noise can be expressed in terms of a temperature, called *noise temperature* T_{noise}. In practice, given a certain noise power P, T_{noise} it is the temperature that would produce the same level of thermic noise:

$$\frac{P}{\Delta\nu} = k_B T_{\mathrm{noise}}, \tag{2.5}$$

where $\Delta\nu$ is the total bandwidth over which noise power is measured and k_B is the Boltmann constant. Noise temperature is one of the factor that determines the sensitivity on an instrument.

Given an array of N receivers, the sensitivity is given by the radiometer equation:

$$\delta T = k \frac{T_{\mathrm{sys}}}{\sqrt{N}} \sqrt{\frac{1}{\Delta\nu\tau} + \frac{\delta G}{G}}, \tag{2.6}$$

which provides the error in the estimate of the temperature T for a given pixel in the sky. In this equation $T_{\mathrm{sys}} = T_{\mathrm{signal}} + T_{\mathrm{noise}}$ is the total input of each receiver (the sum of signal entering the instrument plus any noise), $\Delta\nu$ is the bandwidth in which the receiver is sensitive, τ is the observation time and $\delta G/G$ quantifies the stability of the amplifiers used in the system. We can easily see that there are several ways to improve the sensitivity of an instrument:

- Increase the number of detectors. Missions like Planck implemented $\sim 10^2$ detectors, while future experiments like CMB-S4 (see Section 2.3) will implement $\sim 10^5$ detectors.

- Increase the bandwidth $\Delta\nu$. Typical bands in CMB experiments are of the order of the 10%–30% of the central frequency.

- Decrease T_{sys}. Since white noise is mostly due to thermal fluctuations, this means that the instruments must work at cryogenic temperatures.

- Increase the integration time. This can be easy for ground-based experiments and space missions, where the typical time is few years, but can be a serious limit for balloon-borne experiments.

- Make the instrument as stable as possible, in order to minimize $\delta G/G$. Since gain fluctuations are typically due to thermal instabilities, this can be achieved by keeping the detectors at cryogenic temperatures. The level of $\delta G/G$ is generally of the order of 10^{-2}–10^{-3}.

Besides white noise, real receivers, are affected by another type of noise, the so-called *1/f noise*. It is correlated noise consisting in fluctuations on long timescales of the signal, and it has a frequency spectrum such that its Power Spectral Density (PSD) is inversely proportional to the frequency of the signal (from which the name). The PSD of a generic receiver, affected by both white and *1/f* noise, can be effectively described as:

$$S(\nu) = \sigma^2 \left[1 + \left(\frac{\nu_{\text{knee}}}{\nu} \right)^\alpha \right], \tag{2.7}$$

where the white noise is described by a constant with value σ^2 and the *1/f* noise as a straight line with slope α. *1/f* noise dominates at low frequencies, while white noise dominates at high frequencies. The so-called *knee frequency* f_{knee} is the frequency at which the two noise contributions are equal. A depiction of the typical output of a real receiver, together with its PSD, is reported in the bottom panel of Figure 2.4).

With respect to white noise, *1/f* noise is more troublesome to deal with, as it generates unwanted structures on the sky map that alters the statistical properties of the cosmic signal, which is particularly relevant for CMB anisotropy. It can be partly reduced by making use of radiometers with pseudo-correlation differential design, as done for the LSPE/STRIP instrument (see Section 4.1.2). The residual noise can be further reduced during the map-making process [1] via software algorithms to be applied on the data. Several map-making agorithms have been implemented and tested in the last decades with the purpose of minimizing 1/f noise. One particularly interesting method is the *destriping* algorithm, which has been prominently used in the analysis of Planck data. The destriping algorithm will be extensively described in Section 5.2, as its implementation in the data analysis pipeline for the LSPE/STRIP experiment has been one of the main activities of this PhD thesis.

---

[1] The term "map-making" refers to the process of building a sky map from the data stream collected by a telescope.
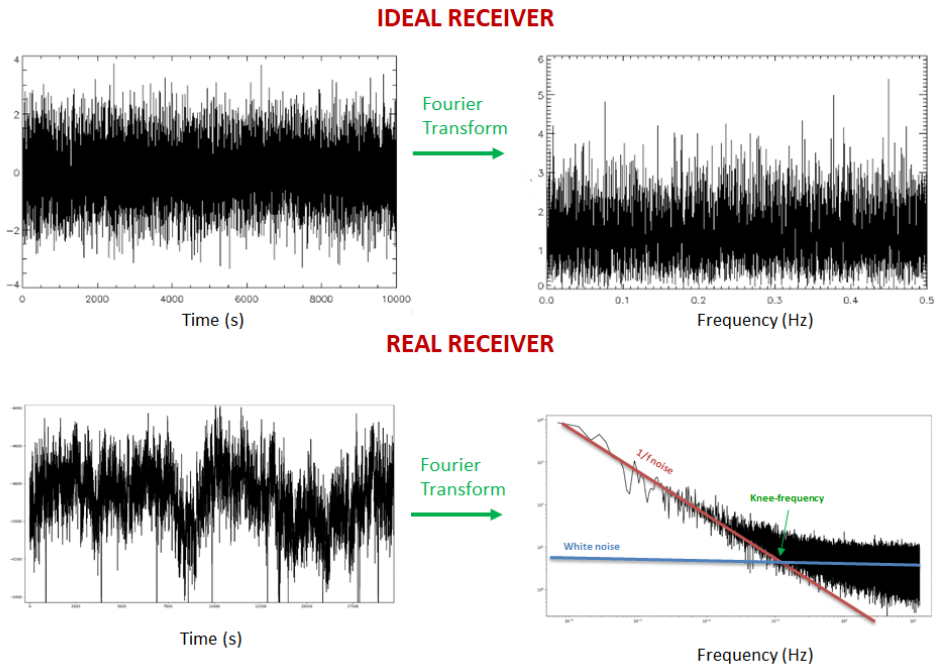
Figure 2.4: Output example of an ideal and a real device. The data timestream is reported, together with its power spectral density (PSD). The ideal receiver output is affected just by Gaussian white noise and its PSD is flat, meaning that the power is spread evenly among all the frequencies. A real receiver, however, is affected also by long period fluctuations, which cause a *1/f* trend in the PSD.

2.2.2 Detector technologies

To measure electromagnetic radiation in the microwave range, a few technologies are available. Traditionally, CMB experiments have used either radiometric receivers or bolometers, but in the last years new technologies, such as Kinetic Inductance Devices (KIDs), have been succesfully tested. In the following, we provide a brief overview of the detector technologies used by current CMB experiments.

Radiometric receivers

Microwave radiation can be measured using radiometric receivers based on HEMTs amplifiers. The radiation is first amplified and filtered and then it is converted into a voltage and measured by an Analog-to-Digital (ADC) electronic component. These kind of devices are called *coherent receivers*, as they are able to measure both the phase and the amplitude

of the electromagnetic wave. The most widely used amplifier for CMB experiments is the High Electron Mobility Transistor (HEMT), for it provides high gain with relatively low noise with respect to other types of amplifiers. The ability of measuring the phase allows radiometric receivers to be used for direct measurement of Stokes Q and U, as we will see in Section 4.1.2. However, the preservation of the full amplitude and phase information in the incoming signal has the cost of a limit on the minimum achievable noise, set by quantum fluctuations. The system noise temperature of a radiometric receiver working at frequency ν is in fact (Lawrence et al., 2009):

$$T_{\text{sys}} = \frac{h\nu}{k \log 2} \Rightarrow \frac{T_{\text{sys}}}{1\,K} = \frac{\nu}{20\,\text{GHz}}, \qquad (2.8)$$

which implies that they work better at low frequencies. For CMB measurements, the limit is typically below $50 \div 100\,\text{GHz}$. At higher frequencies, other technologies, like bolometers, are more performant.

Bolometers

A bolometer is a detector made of an absorptive element, such as a thin layer of metal, connected to a thermometer and a thermal reservoir (a body of constant temperature) through a thermal link. Any radiation impinging on the absorptive element raises its temperature above that of the reservoir, and this is measured by the thermometer, placed on the absorptive element. The thermometer can be either a traditional thermometer or a Transition-Edge Sensor (TES). The role of the reservoir is to dissipate the excess heat absorbed by the element. The return to thermal equilibrium, and thus the ability to proceed with another measurement, however, takes some time and depends on the *time constant* of each bolometric detector. To obtain the very high sensitivities needed by CMB experiments, both radiometric receivers and bolometers should work at cryogenic temperatures. Temperature stability is crucial to minimize electric and thermal fluctuations. However, while HEMTs show low noise at $10^{-2}\,\text{K}$, bolometers require much lower temperatures (100–300 mK), more difficult to reach.

Bolometers are directly sensitive to the energy left inside the absorber. For this reason they can be used not only for ionizing particles and photons, but also for non-ionizing particles, any sort of radiation, and even to search for unknown forms of mass or energy (like dark matter).

The fact that the energy of an incoming electromagnetic wave is converted into thermal energy implies that any information about its phase is lost. On one hand, this means that there is no quantum lower limit on the noise achievable by a bolometer, on the other it means that a single bolometer cannot be able to directly measure the Stokes parameters Q and

U. To measure the polarization of radiation with bolometers, one must necessarily put a polarization filter in front of the bolometer. Two typical choices are:

- using more than one bolometer, each one associated with a polarized filter. The most common configuration is to use 4 bolometers and to align the filters at angles $0°$, $45°$, $90°$, $135°$. This provides enough information to esitmate I, Q and U.

- using an half-wave plate (HPW), that is to say a polarization filter in continuous or stepped rotation, so that the time stream of measurements of a single bolometer can be used to quantify both Q and U (Kusaka et al., 2014). This technology also allow a better control of systematics.

Kinetic Inductance Devices (KIDs)

KIDs are a novel kind of detectors that measure the flux of radiation incident on a strip of superconducting material by detecting the breaking of Cooper pairs (Day et al., 2003). The kinetic inductance of the superconducting strip, in fact, is inversely proportional to the density of Cooper pairs, and thus the kinetic inductance increases upon photon absorption. The strip is combined with a capacitor to form a microwave resonator whose resonant frequency changes with the absorption of photons. KIDs are well suitable for developing large detector arrays and their response is usually faster than bolometric detectors by one order of magnitude or more. KIDs are currently used in the NIKA2 experiment (Calvo et al., 2016) and in the GroundBIRD experiment (Choi et al., 2018).

2.2.3 Systematics effects

In this Section we review the main systematic effects impacting on CMB measurements. Of course, a detailed analysis of instrumental systematics depends on the specific instrument used to perform the measurement. The purpose of this section is to give an idea of the most common criticalities that a CMB experiment has to face (Aghanim et al., 2014). The evaluation of the impact of the first two systematics effects, *1/f* noise and bandpass mismatch, on the LSPE/STRIP instrument performance has been one of the activities of my PhD and it is reported in Chapter 6.

1/f **noise**

Long term instabilities in the amplification of the signal are a source of *1/f* noise in the data stream, as explained in Section 2.2.1. This kind of

noise generates unwanted structures in the sky map and it is considered a systematic effect.

Bandpass mismatch

Receivers are sensitive only in a limited range of frequencies. The transmission of a system as a function of frequency is described by a function, called *bandpass response $I(\nu)$*. Ideally, all detectors in a certain channel of a CMB instrument should, in principle, have the exact same bandpass response in order to reconstruct a single map of the sky. If, however, the detectors that are meant to be identical have slightly different bandpasses, artifacts are introduced into the map obtained by combining the signals from several detectors. That is simply because detectors with different bandpass response are more or less sensitive to different signals from the sky. Such effect is called "bandpass mismatch".

Spurious fluctuations

The signal detected can be contaminated by the presence of fluctuations that do not depend on the observed sky emission. They can have many different orgins: thermal fluctuations of the focal plane, electronic fluctuations in the amplifier bias voltages, spurious cross-talk between different channels etc. They can be periodic and affect long data streams, or they can be fast and sudden, causing spikes in the timelines. In bolometers, spikes can also arise from cosmic rays hitting the absorber.

Side lobes contamination

The optical response of an antenna is quantified by the so called *beam pattern $\gamma(\theta, \phi)$*, which express the power received (or emitted) by the antenna as a function of the pointing direction (θ, ϕ). Given an input brightness temperature T_{sky}, the temperature T measured by an instrument depends on its beam pattern according to the following formula:

$$T(\theta\phi) = \frac{\int_{4\pi} T_{\text{sky}}(\theta', \phi')\gamma(\theta', \phi')d\Omega'}{\int_{4\pi} \gamma(\theta', \phi')d\Omega'} \tag{2.9}$$

The beam pattern $\gamma(\theta, \phi)$ of an ideal directional antenna would be a Dirac's delta in the pointed direction. In real life, the radiation pattern of most antennas shows "lobes" at various angles, directions where the signal strength reaches a maximum, separated by "nulls", angles at which the signal strength falls to zero (see Figure 2.5). In a directional antenna in which the objective is to receive the electromagnetic waves in one direction, the lobe in that
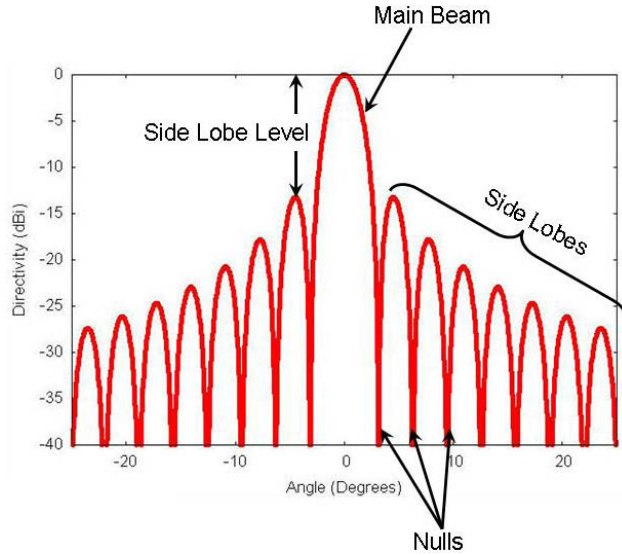
Figure 2.5: A typical beam pattern $\gamma(\theta, \phi)$ of a directional antenna. Most of the radiation is contained in the main beam, centered at zero. Note that the vertical axis is experessed in dB (logarithmic scale).

direction (called *boresight*) is designed to have a larger signal strength than the others; this is the "main lobe". The angular width of the main lobe at half its maximum height is called the Full Width Half Maximim (FWHM), and it is one of the most used parameters to characterize the resolution of an instrument. The other lobes are called "side lobes", and usually represent unwanted radiation in undesired directions. The side lobes should be carefully taken into account to recover the correct beam function and properly deconvolve the observed signal. Polarization measurements, in particular, require extreme purity in the optical response of the instruments. For instance, the beam should be as much symmetric as possible around the boresight direction in order not to introduce spurious polarization. A proper characterization of the beam properties is essential and can be achieved during the instrument test phase and also during calibration on site, by observing specific point sources.

ADC non linearities

The typical output of a CMB instrument is a time stream of voltages, which is then digitalized by an an analog-to-digital converter (ADC). A wide dynamic range of the ADC is needed in CMB instruments, which aim to measure both the CMB and the Galactic foregrounds. The ADC linearity requires that the voltage step sizes between successive binary outputs are

constant over the entire input dynamic range. If these steps are not constant we have a non-linearity in the ADC response that leads to calibration errors.

Imperfect photometric calibration

Typically, for an experiment not interested in polarization, calibration is performed observing radiation coming from bright sources (e.g., planets, Moon etc.) or using the CMB Dipole, caused by the motion of the Solar System with respect to the CMB rest frame. For polarization, bright and well characterized polarized sources in the sky are needed, such as the Crab Nebula. Errors in calibration can lead to uncertainties in the polarization angle of the detectors and in the normalization factor of the reconstructed angular power spectra. They can be due to incorrect assumptions regarding the calibration signal, incorrect treatment of the calibration signal (e.g. during deconvolution of the calibration signal with the detector beam), incorrect reconstruction of gain fluctuations.

Pointing uncertainties

Errors in the reconstruction of the real pointing direction are translated into uncertainties in pixel total intensity and polarization measurements. If pointing uncertainties are not constant in time, then the statistics of the sky anisotropy measurements is not preserved, with a consequent impact on power spectrum and cosmological parameters. Typically, this effect is more worrisome for small angular scales. Pointing uncertainties are generally caused by uncertainties in the telescope pointing determination or uncertainties in the focal plane geometry reconstruction.

Leakage effects

Several non-idealities in the instrument architecture can cause what is normally referred to as leakage effects, i.e. a transfer of power from total intensity to polarized signal ($I \rightarrow Q/U$) or a mixing between the Stokes Q and U signals ($Q/U \rightarrow U/Q$). $I \rightarrow Q/U$ leakage, in particular, can have a relevant effect impact on the measurement of polarization (both of CMB and foregrounds), as the signal emitted in total intensity is much larger than the polarized one.

$Q/U \rightarrow U/Q$ is mainly due to uncertainties on the polarization angle of the detectors. As mentioned before, the values of Q and U depend on the chosen reference frame. Each detector measures Q and U in its own reference frame, and therefore the precise knowledge of the detector polarization angle is essential to report all the measurements in a unique coordinate system. If Q and U are the values of the Stokes parameters in

the astronomical coordinate frame, and Q' and U' are the values measured in the coordinate system of a certain detector, we have:

$$\begin{pmatrix} Q \\ U \end{pmatrix} = \begin{pmatrix} \cos 2\theta & -\sin 2\theta \\ \sin 2\theta & \cos 2\theta \end{pmatrix} \begin{pmatrix} Q' \\ U' \end{pmatrix}. \tag{2.10}$$

where θ is the polarization angle. It is clear, therefore, that an uncertainty in θ could lead to $Q/U \rightarrow U/Q$.

Atmospheric emission

Atmosphere is an unavoidable foreground in any measurement with a ground-based telescope and can constitute an important limitation to its ultimate performance. The atmospheric transmission windows for CMB observation are typically < 15, 30–50, 75–110, 120–180, and 190–320 GHz bands. The atmospheric constribution in this frequency range is dominated by oxygen and water vapor, whose emissions increase the detectors optical-load and, therefore, their overall white-noise level. The atmospheric impact is related to the observed frequency and to the pointing altitude, as it depends on the thickness of the atmospheric layer observed. Being T_z the atmospheric brightness temperature seen by a telescope at zenith (minimum atmospheric thickness), the T_{atm} seen with an elevation angle θ from zenith will be:

$$T_{\mathrm{atm}} = T_z \cdot \sec \theta. \tag{2.11}$$

In addition, the inhomogeneous distribution of water vapor molecules is driven by complex mechanisms, which depend on the properties of the atmosphere above a given observation site, and results in both temporal and spatial variations of the received optical power. If treated as an additional noise-like component, this atmospheric contamination results in an additionally spatially correlated signal in the time stream of any detector. Modeling atmospheric effects is complex. Fluctuations of the atmospheric optical depth generate emission with amplitude and scale which depend on both the scanning strategy, and the properties of the atmosphere (dryness, air density, temperature, pressure, etc.). Moreover, wind can displace atmospheric structures, introducing hard to model non-stationary effects. An example of atmospheric model and its application on POLARBEAR first season data can be found in Errard et al. (2015).

The atmospheric emission is expected to be largely unpolarized. However, atmospheric emission may in general contribute to the detected polarized signal due to the polarization leakage introduced by instrumental non-idealities. In addition, ice crystals in upper tropospheric clouds scatter

thermal radiation from the ground and can produce a horizontally-polarized signal. Takakura et al. (2019) suggests in situ measurements of the clouds with an extra instrument (e.g. a webcam) to perform a correlation analysis with the measured polarized signal and mitigate the contamination. Another approach might be to perform foreground separation in the time domain. The cloud signal, in fact, has frequency dependence markedly different from that of the CMB and the other astrophysical foregrounds. Therefore, it would be possible to separate the cloud signal in measurements with multi-frequency bands.

2.3 Current and future experiments

The field of CMB polarization measurements is extremely crowded: there are tens of experiments located all around the World, using different technologies and looking at different frequencies. In the following, we breafly overview the main current and future experiments, grouping them according to the kind of site chosen for their operation. Their frequency coverage, years of operation and detector technology is also schematically depicted in Figure 2.6. For comprehensive list of past, ongoing and future experiments we address to the Legacy Archive for Microwave Background Data Analysis (LAMBDA, https://lambda.gsfc.nasa.gov/product/expt/).

2.3.1 Ground-based experiments

With respect to space-borne instruments, ground-based experiments are much easier to deal with: they can deploy larger primary mirrors in order to reach higher angular resolution, they can have a larger focal plane hosting many detectors and their integration time can be made arbitrarly large, which helps improving the sensitivity. However, only a fraction of the 4π sky is visibile from Earth (typically no more than 70%) and they are affected by atmospheric emission. In order to have an atmospheric signal low enough not to prevent the measurement, one wants high-altitude dry sites, with very good weather conditions during the whole year. The most used locations are:

- the Atacama Desert in Chile: ACTPol (ACTPol collaboration, 2016b), Polarbear (Keating and PolarBEAR collaboration, 2011), CLASS (CLASS collaboration, 2016), Simons Array (Ade et al., 2019);

- Antarctica: SPTpol (Benson and SPT collaboration, 2014), BICEP/Keck (collaboration, 2016);

- Tenerife: QUIJOTE (Rubiño-Martín et al., 2012), GroundBIRD (Choi et al., 2018);

- Argentina: QUBIC (QUBIC collaboration, 2016).

Two peculiar cases are the C-BASS experiment (Jones et al., 2018), which exploits two telescopes, one in the northern hemisphere (California) and one in the southern (South Africa), to produce a full sky map of the synchrotron emission at 5 GHz, and the Large Scale Polarization Explorer (LSPE), which will exploit the sinergy of a ground-based telescope (at Tenerife) and of a balloon-borne experiment, looking at the same sky region. A full description of the LSPE experiment is provided in Chapter 3.

For what concerns the most promising next-generation ground-based experiment, we spend a few words about three of them:

- the **Simon's Observatory** (SO), leaded by the United States, will be located in the Atacama Desert and will begin observations in the early 2020s. It will measure CMB temperature and polarization in six frequency bands (27, 39, 93, 145, 225 and 280 GHz) with 60 000 cryogenic bolometers, with the aim to constrain the tensor-to-scalar ratio at a level of $r < 0.003$.

- the **Ali CMB Polarization Telescope** (AliCPT) is a chinese project in Ali area of Tibet. The first stage telescope is designed to have about 7000 TES bolometers at 95 and 150 GHz. The second stage is to have a more sensitive telescope, with more than 20 000 detectors. By about 10-year observation, the raw sensitivity of r will reach ~ 0.001, as AliCPT project being carried out and upgraded (Li et al., 2018).

- **CMB-S4** (Stage-4) will be composed of several telescopes operating at the South Pole, at the high Chilean Atacama plateau, and possibly at (not yet defined) northern hemisphere sites (Abazajian et al., 2016), in order to reach a $\sim 70\%$ sky coverage. Like SO, it is an experiment with United-States leadership. CMB-S4, foreseen for late 2020s, is intended to to be the "definitive ground-based experiment" and its aim is to reach the cosmic variance limit for all angular scales accessible from ground ($l \lesssim 10$). Regarding B-modes, the goal is constrain r down to 0.002 at 95% C.L., over an order of magnitude stronger than current limits. The technologies to be used for the thousands S4 detectors have not been decided yet, but will probably TES bolometers for high frequencies and KIDs for low frequencies.

2.3.2   Space experiments

Experiments from space have the obvious advantages of a 100% coverage of the sky sphere and of being completely free from atmospheric contamination. However, they are much more complex and expensive than ground-based and balloon-borne experiments. So far, there have been four CMB experiments from space: RELIKT-1 (Klypin, Strukov, and Skulachev, 1992), COBE (Mather et al., 1991), WMAP (Bennett et al., 2003), and Planck (Planck Collaboration, 2016).

A new space mission, LiteBIRD has been recently (May 2019) approved by the Japanese space agency. LiteBIRD will be the first space mission specifically focused to test inflation with an all-sky survey of CMB polarization, with an uncertainty on the tensor-to-scalar ratio fo the order of 10^{-3}. It will observe in 15 bands between 34 and 448 GHz with about 3000 TES bolometers. LiteBIRD is planned to be launched in late 2020s for three years of observations at the Sun-Earth Lagrangian point L2.

2.3.3   Balloon-borne experiments

To strongly reduce the atmospheric contamination, but with much lower cost with respect to space missions, one can rely on stratospheric balloons. The main disadvantages of balloons are their limited observing time (generally about two weeks), the limit of the mass to be carried and the difficulty of retriveing the data at the end of the flight. Notable examples are OLIMPO (OLIMPO collaboration, 2005), SPIDER (SPIDER collaboration, 2010), EBEX (EBEX collaboration, 2013), PIPER (PIPER collaboration, 2017), and LSPE/SWIPE (de Bernardis et al., 2012).
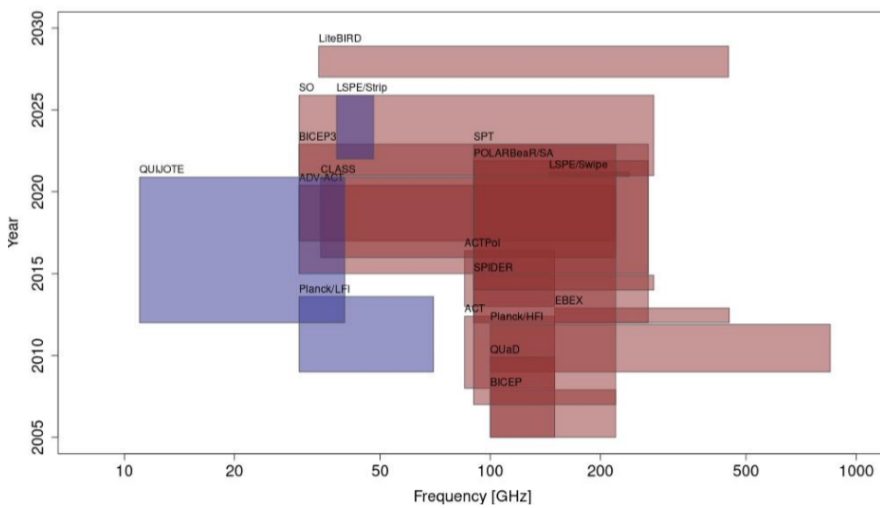
Figure 2.6: Overview of the most significant current and future CMB experiments. The years of (presumed) activity are shown along the vertical axis, while the frequency coverage spans the horizontal axis. The colors identifies the technology used for the detectors (blue for radiometric HEMTs receivers, red for bolometers). Figure by Maurizio Tomasi.

Chapter 3

The Large Scale Polarization Explorer

The *Large Scale Polarization Explorer* (LSPE) is an international experiment with italian leadership designed to measure the polarization of the Cosmic Microwave Background at large angular scales. Its primary aim is to constrain the B-modes component of the polarization, improving the limit on the tensor-to-scalar ratio down to $r = 0.03$, at 99.7% confidence level[1] As mentioned in Section 1.6.2, looking at large angular scales is crucial in order to detect primordial B-modes, as the small angular scales of the CMB B-mode spectrum is dominated by gravitational lensing. A second target is to produce wide maps of the Galactic polarized foregrounds, neamly synchrotron radiation and interstellar dust emission, enabling us to map the galactic magnetic fields and to study the properties of the ionized gas and of the diffuse interstellar dust in the Milky Way. Other targets of the mission includes an improved measurement of the CMB optical depth τ (measured from E-modes spectrum at large angular scales), the investigation of the so called *low-l anomaly* (Planck Collaboration et al., 2016), improved limits of cosmic birefringence (Pogosian et al., 2019).

LSPE will observe 25% of the sky in the Northern hemisphere relying on the synergy of two indipendent instruments, SWIPE and STRIP, complementary for frequency coverage and technology. SWIPE will survey the sky at 145, 210 and 240 GHz from a spinning stratospheric baloon, launched

---

[1]As seen in section 1.6.3, the current best limit is $r < 0.07$ (95% confidence level).

from Svalbard Islands, in a long duration flight (~ 15 days) during the Artic winter. STRIP is instead a ground-based experiment observing the sky for two years at 43 and 95 GHz from the Teide Observatory in Tenerife (Canary Islands). Figure 3.1 offers a schematic view of the LSPE experiment, showing the sky-region of interest, the location of the two instruments and a glimpse of the scanning strategy. The sky coverage of STRIP and SWIPE is separately shown in Fig. 3.3, together with their overlap.

Since the CMB polarization signal is expected to be smaller than the polarized foreground from our Galaxy, a wide frequency coverage is needed to carefully monitor the foregrounds at frequencies where they are dominant, in order to subtract them during data analysis. Figure 3.2 shows the frequency coverage of LSPE in comparison with the polarization spectra of CMB and of its major foregrounds, namely synchrotron and dust. STRIP will characterize the synchrotron emission, prominent at low frequencies, where the atmospheric transmission and noise are favorable to a ground-based experiment. On the other hand, SWIPE's two high frequency channels will accurately measure the interstellar dust emission in addition to the cosmological channel at 145 GHz. Table 3.1 delineates basic performance parameters for SWIPE and STRIP in the baseline configuration, while a more detailed description of the two instruments is reported in the following sections.

3.1   SWIPE: the high frequency instrument

The general idea under SWIPE conception is to maximize the sensitivity to CMB polarization at large angular scales using a very wide focal plane populated with multi-moded bolometers (de Bernardis et al., 2012). The spectral coverage of SWIPE has been optimized to be sensitive to CMB polarization with one wide-band channel in correspondence of the peak of CMB brigthness (145 GHz, 30% bandwidth), and to characterize the signal from interstellar dust with two ancillary channels at 210 and 240 GHz. These two channels have narrower bands (20% and 10% respectively), in order to accurately measure the slope of interstellar dust brightness.

3.1.1   The balloon flight

The SWIPE instrument will fly in a circumpolar long duration flight (of approximately two weeks) on a spinning stratospheric balloon during the Artic night. The launch is foreseen for probably Winter 2021. Stratospheric balloon altitudes (about 35 km above the sea level) are crucial in order to reduce the effect of atmospheric emission, which is quite important at 140 GHz and much more relevant at higher frequencies. A winter launch guarantees the possibility to cover a large fraction of the sky, allowing us
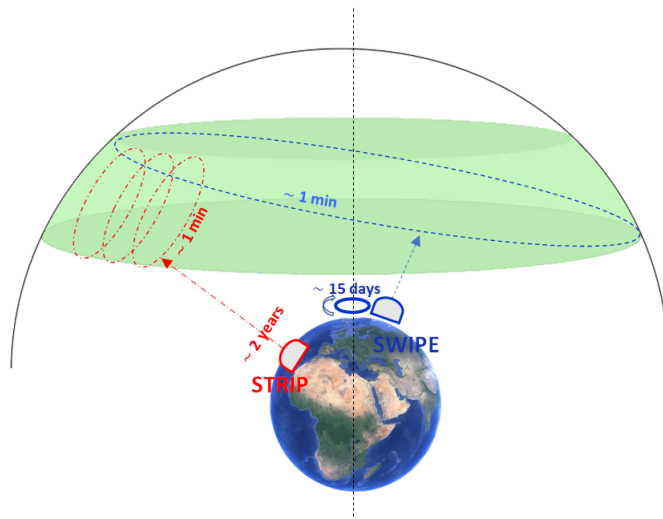
Figure 3.1: Schematic overview of the LSPE experiment. The two instruments will observe the same sky region in the Northern emisphere. SWIPE from a spinning atmospheric baloon in a long duration flight (~ 15 days) during the Artic winter and STRIP from the Teide Observatory in Tenerife (Canary Islands) with a 2-years observation campaign.

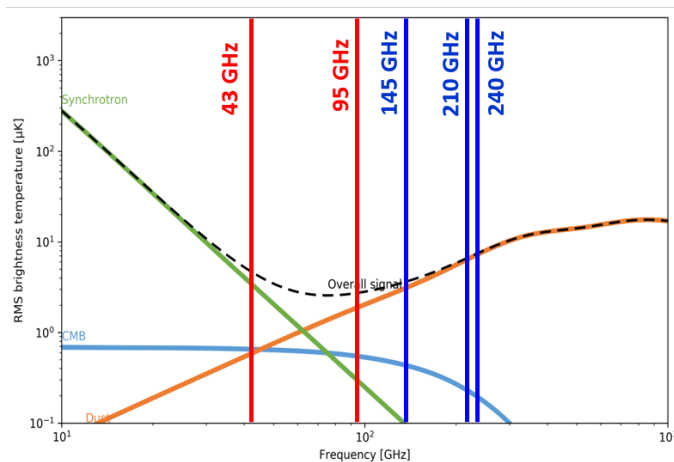**Figure 3.2:** Scheme of the LSPE frequency coverage (with STRIP zenith distance of 20°). The thick solid lines represent the central frequency of SWIPE and STRIP channels, respectively in blue and red. The frequency behavior of the most important diffuse foregrounds for CMB polarization, namely dust (in orange) and synchrotron (in green) is shown, together with the CMB polarization spectrum (in cyan).
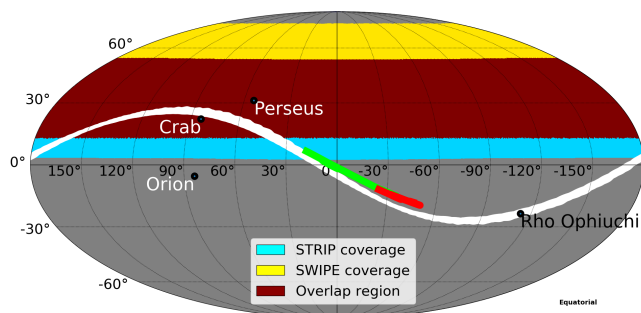
Figure 3.3: Map in equatorial coordinates of STRIP and SWIPE sky coverage. The yellow area represents SWIPE sky coverage, the cyan area represents STRIP sky coverage, the red area is the overlap. The map also show the positions of candidate calibration sources: the Crab and Orion nebulas, of the Perseus molecular cloud and the trajectories of Jupiter (in green), Saturn (in red) and the Moon (white) as calculated for the year 2019. The sky fraction observed by STRIP depends strongly on telescope elevation, e so does its sensitivity.

to explore large angular scales with enough sensitivity. At the moment, launches in the polar night are only possible from the northern hemisphere, due to logistic difficulties in accessing Antartic regions during winter. The most credited launching station for SWIPE is Longyearbyen in Svalbard Islands (Norway): with a latitude of $78.2°$, it represents an ideal location to guarantee total darkness during operation. Longyearbyen is a well-established site: several balloon launches have been done from there over the last few years, both in Summer and in Winter. An alternative would be the Esrange Space Center, near Kiruna (Sweden), although at southern latitudes ($67.8°$ N). Using the Earth as a giant solar shield, the SWIPE payload will spin in azimuth at constant speed, keeping a fixed elevation. A long duration winter flight, while having the advantage of thermal stability, away from solar illumination, is very challenging in terms of power system because of the extreme thermal conditions. The absence of solar radiation, in fact, requires a power system fully based on batteries, which are significantly less efficient at low temperatures (external temperature is expected to reach $-90°$ C). A series of technological tests flights has been carried out over the last years, as reported by Iarocci et al. (2008), Peterzen et al. (2008), Peterzen, Masi, and Debernardis (2010), and de Bernardis, Masi, and OLIMPO and LSPE Teams (2013). All istrumental parts of SWIPE are designed to cope with temperatures as low as $-90°$ C, except for the batteries and part of the electronics, which are contained in a thermally insulated box, designed to work above $-40°$ C. The batteries are kept warm by heaters, and thermal

insulation is based on an Aerogel layer. A prototype of this power system was successfully tested on a winter Artic balloon flight in December 2017 (Piacentini et al., 2018) and more tests are planned for the future.

3.1.2 Optical system

The optical system of SWIPE is sketched in the left panel of Figure 3.5. It consists in a single-lens, 490 mm aperture refractor telescope which focuses the incoming radiation on two large curved focal planes, after being split by a wire-grid polarizer tilted at 45° with respect to the instrumental optical axis. As shown in the right panel of Figure 3.5, each focal plane is populated with 326 TES bolometers split in three frequency bands (145, 210 and 240 GHz). Detectors are fed by multi-mode feedhorns, which are parabolic Winston horns: each feed-horn is a smooth-walled antenna that couples several propagation modes to the underlying bolometric absorber. Unlike single-mode horns, Winston horns can achieve high efficiency in the main beam and ensure high suppression of stray radiation through the incoherent superposition of the propagated modes at large angles. The greatest advantage of multi-mode optics, however, is in its capacity to significantly boost the instrument sensitivity at higher levels. In fact, for a given number N of efficiently coupled radiation modes at a given frequency, the photon-noise limited S/N ratio improves as $\sqrt{N}$ (Gualtieri, 2016). This means that collecting tens of modes for each detector makes possible to achieve a sensitivity equivalent to that of hundreds of single-mode horns. The system is cooled-down by a custom-made cryostat, a toroidal ^{4}He tank supported by a stiff structure of fiberglass tubes and surronded by two vapor cooled shields, at 170 K and 40 K. This L^{4}He tank, of about 259 liters of volume, cools down the system to 1.6 K. In addition, a ^{3}He sorption fridge is used to cool-down the detectors arrays at 0.3 K (Coppi et al., 2016).

3.1.3 Polarization modulation

As mentioned before, the magnitude of the B-modes signal is known to be less than 1 μK. Detecting such a small signal from the ground or from a stratospheric balloon is challenging because of variable atmospheric trasmission and instrumental *1/f* noise. A rapid modulation of linear polarization by an half-wave plate (HWP) is a common tecnique to reduce these unwanted effects. By rapidly changing the polarization angle to which the detectors are sensitive, in fact, we actually move the polarization signal from the low-frequency part, dominated by the *1/f* noise, to higher frequencies allowing thus to sample the Stokes parameters Q and U in the white noise regime. Additionally, the HWP enables the time-stream of measurements

Instrument	STRIP		SWIPE		
Site	Tenerife		balloon		
Freq (GHz)	43	95	145	210	240
Bandwidth	16%	8%	30%	20%	10%
Angular resolution FWHM (arcmin)	20	10	85		
Detectors technology	HEMT		TES multimoded		
Number of detectors N_{det}	49	6	162	82	82
Detector noise equivalent temperature ($\mu K_{CMB}\sqrt{s}$)	539	1347	12.7	15.7	30.9
Mission duration	2 years		8 - 15 days		
Duty cycle	35%		90%		
Sky coverage f_{sky}	37%		38%		
Map sensitivity $\sigma_{Q,U}$ ($\mu K_{CMB} \cdot$ arcmin)	122	874	10	17	34
Noise power spectrum $(\mathcal{N}_\ell^{E,B})^{1/2}$ ($\mu K_{CMB} \cdot$ arcmin)	201	1436	16	28	55

Table 3.1: LSPE baseline instrumental parameters.

of one bolometer, which is sensitive to a single linear polarization state, to be used to quantify both Q and U Stokes parameters. The temperature of SWIPE's half-wave plate (1.6 K) is optimized to minimize the background power on the detector and the effect of spurious signals due to non-idealities of the HWP itself (Columbro et al., 2019).

3.2 STRIP: the low frequency instrument

Initially designed to be a balloon experiment sharing the same gondola as SWIPE (Bersanelli et al., 2012), STRIP has been recently converted into a ground-based experiment (Franceschet et al., 2018). STRIP consists of an array of 49 coherent polarimeters operating at 43 GHz (Q-band) for the characterization of Galactic synchrotron emission and 6 polarimeters operating at 95 GHz for atmospheric monitoring. The receivers array is cooled down to 20 K by a cryostat facing the focal plane of a dual-reflector Cross-Dragone telescope of 1.5 m aperture. STRIP will be installed at the Teide Observatory in Tenerife in mid-late 2021.
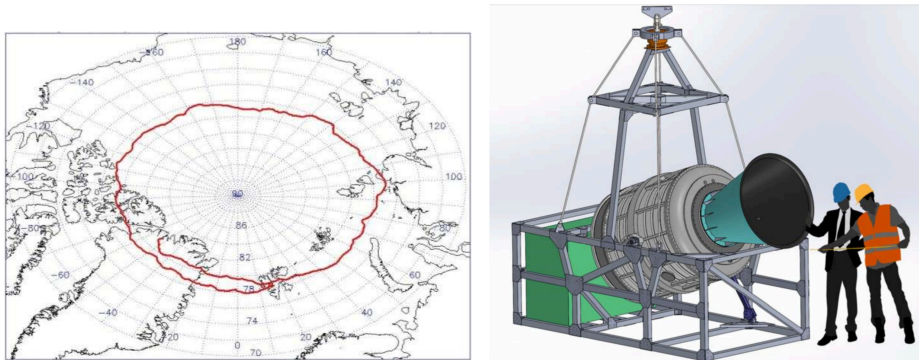
Figure 3.4: *Left*: Complete circumpolar trajectory of a balloon launched from Svalbard. The flight lasted 17 days, until the impact of the payload on the northern Greenland Ice Sheet (Peterzen, Masi, and Debernardis, 2010). *Right*: SWIPE overview: the instrument will be mounted on a frame (called "gondola"), providing also a control system, the instrument power system and electronics.
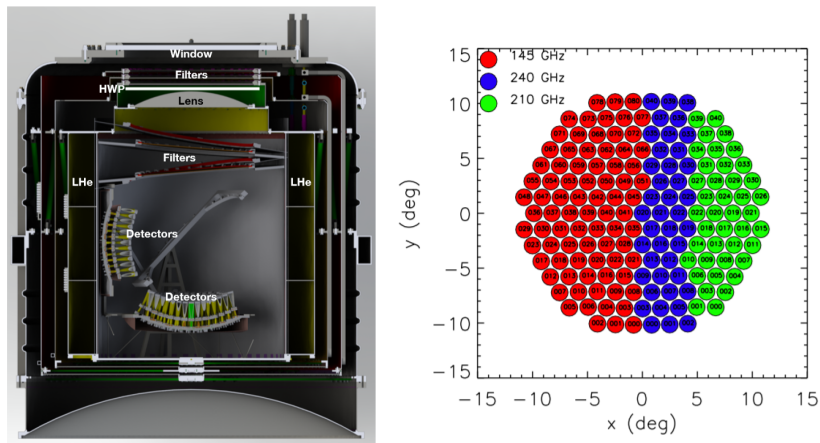

Figure 3.5: *Left*: a section of the SWIPE cryostat and polarimeter. The main components are labelled in figure. *Right*: SWIPE distribution of detectors in one of the two equivalent focal planes. The axes represent the position of the detectors projected in the sky.

3.2.1   Observation Site

The Teide Observatory is an astronomical observatory on Mount Teide (at 2390 m above the sea level) located on Tenerife (Canary Islands, Spain) and it is one of the most important astrophysical observation sites in the northern hemisphere. Run by the Spanish Instituto de Astrofisica de Canarias (IAC) since its inauguration in 1964, this site provides excellent observing conditions and has been well-tested for astronomical observations for more than 30 years. In particular, it is home to Europe's finest solar telescopes and has also a long tradition in CMB research, remembering past experiments like the Tenerife radiometers (Gutiérrez et al., 2000), the IAC-Bartol experiment (Femenía et al., 1998), the JBO-IAC 33 GHz Interferometer (Harrison et al., 2000), the COSMOSOMAS experiment (Fernández-Cerezo et al., 2006) and the Very Small Array interferometer (Watson et al., 2003). The Teide Observatory is a dry site, with a median precipitable water vapour of 3.5 mm and the inversion layer lying below the obervatory for approximately 80% of times (Castro-Almazán et al., 2016). The ambient temperature at the site usually remains between 0 and 24° C and the wind speed is on average 20 km/h, with occasionally wind gusts that can reach 200 km/h speed in extreme weather conditions. The STRIP telescope will be installed in the aluminium ground screen formerly used by the main array of the VSA. The basement will be adapted to the larger size and weight of the STRIP telescope and the entire structure will be eventually protected by a sliding roof, which will cover the whole enclosure in case of too strong wind or bad weather.

STRIP will share the observing site with other two CMB polarization experiments: QUIJOTE and GROUNDBIRD. The QUIJOTE experiment (Rubiño-Martín et al., 2012) consists of two telescopes of 2.25 m aperture following a Cross-Dragone optical configuration like STRIP, but it measures signals at medium angular scales ($\sim 1°$). The first QUIJOTE telescope, hosting a multi-frequency instrument (11, 13, 17 and 19 GHz), is in operation since 2012 and has already produced scientific results on the intensity and polarization of the microwave emission from Perseus, W43, W47 and Taurus Molecolar Clouds (Génova-Santos et al., 2015; Génova-Santos et al., 2017; Poidevin et al., 2019). In addition, its measurements has been used to complement and characterize galactic contamination in the maps obtained by the Planck satellite. The second telescope is in operation since 2016 and it is equipped with detectors at 30 and 40 GHz.

The second experiment is GroundBIRD, a fast-spinning (30 rpm) small-aperture (30 cm) telescope (Choi et al., 2018). Its focal plane consists in $\sim$450 microwave kinetic inductance detectors (MKIDs) cooled at 0.21 K. Like STRIP, GroundBIRD will make a large scale survey ($\sim$40% of the sky),

Figure 3.6: The Teide Observatory in Tenerife. In the background there is mount Teide, the active volcano that gives the name to the Observatory.

but will observe at higher frequencies (145 and 220 GHz). GROUNDBIRD has been deployed at the Teide Observatory at the end of Summer 2019.

All three Tenerife projects (QUIJOTE, LSPE-STRIP and GroundBIRD) aim to observe approximately the same area of the northern sky, opening the possibility of a future joint analysis, exploiting the redundancy for useful cross-checks of systematic effects. Their cooperation will be extremely convenient in order to significantly improve the characterization of the foregrounds (both in intensity and in polarization) in a wide range of frequencies.

3.2.2 Telescope structure and Optical system

The optical layout of STRIP telescope is based on a dual-reflector crossed-Dragone design, which has been recognized as an excellent choice for CMB polarimetry: providing low aberrations, cross-polarization and simmetry over a wide focal plane, it allows to feed a large number of detectors without requiring additional focusing optics, which may introduce additional systematic effects (Tran et al., 2008). STRIP has a parabolic primary mirror with an aperture of 1.5 m and an hyperblic secondary mirror, providing an angular resolution of $\sim 20'$ in the Q-band and $\sim 10'$ in the W-band.

The main requirements on the optics are a cross-polar discrimination better than -30 dB and a level of sidelobes rejection of -55 dB and -65 dB for near and far sidelobes respectively. The detectors array is placed in the focal region, ensuring no obstruction of the field of view. The telescope will be surrounded by a co-moving baffle made of aluminum plates lined with a millimetre-wave absorber, in order to reduce the contamination due to

the sidelobes The optical assembly has been modelled with the GRASP[2] software, including the reflectors, the focal plane unit and the shielding structures as shown in Fig.3.7.

Figure 3.8 provides an overview of the STRIP telescope structure: the optical assembly is installed on top of an alt-azimuthal mount, designed in origin for the CLOVER experiment (K. Grimes et al., 2009), which allow the STRIP optics and receivers to be pointed at any direction in the sky, giving great flexibility to the scanning strategy. The telescope mount, in fact, is a two-axis system that can fully rotate in azimuth and can span elevation angles from 0° to 89.5°. An integrated rotary joint will transmit power and data to the movable parts telescope and the instrument, allowing a continuous spin.

3.2.3 Focal Plane

The focal plane of STRIP consists of an array of 49 coherent polarimeters at 43 GHz (Q-band) and 6 polarimeters operating at 95 GHz (W-band). The receivers, based on the design developed for the QUIET experiment (Cleary, 2010), have the distinctive characteristics of being able to measure the two Stokes parameters Q and U at the same time. The Q-band channel will be used to characterize the synchrotron radiation of the Milky Way, while the W-band channel will be used as atmospheric monitor, especially to track the amount of water vapour. Figure 3.9 offers an overview of the integrated STRIP focal plane.

As depicted in Figure 3.10 each Q-band polarimeter is connected to an optical chain including a circular corrugated feedhorn, a polarizer and an orthomode transducer (OMT). The 49 detectors are arranged into seven independent exagonal modules placed in the focal plane of the telescope and cooled-down to 20 K by a cryostat.

The antenna at the beginning of each radiometer chain is a corrugated feedhorn, which is a well-performing antenna for CMB polarization measurements, given its beam simmetry, its impedance matching over wide frequency bands and its capability to reduce cross-polarization. The feedhorns have been built via the "platelet technique", which consists in constructing the mechanical profile by stacking aluminum plates, each of them providing a tooth and a grove to build the feedhorn corrugation.

Each feedhorn is connected to a septum polarizer that converts linear polarization in circular polarization. The two orthogonal components of the electric field (E_x, E_y) (where the x and y axis orientations are defined by the septum) are converted into right and left circular polarization components
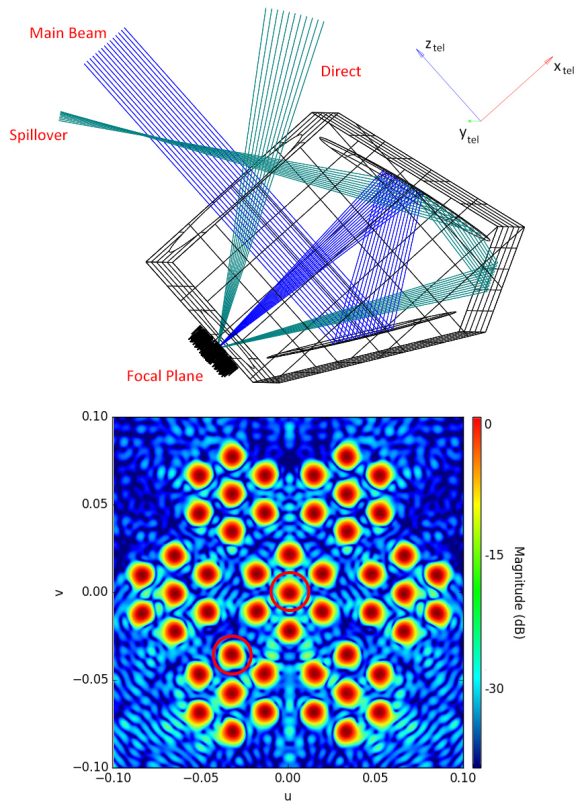
---

[2]https://www.ticra.com/software/grasp/

Figure 3.7: *Left*: STRIP telescope and shields geometry with GRASP simulated ray-tracing. The main beam (in blue) and the two main sources of sidelobes (in green) are represented: the "direct contribution", generated by the rays hitting the focal plain without any interaction with the reflectors and the "spillover", due to rays reflected by the secondary mirror and by then by one of the shields (Franceschet et al., 2018). *Right*: footprint of the STRIP focal plane (with Q-band only) on the sky as seen by an observer looking towards the telescope along its optical axis.
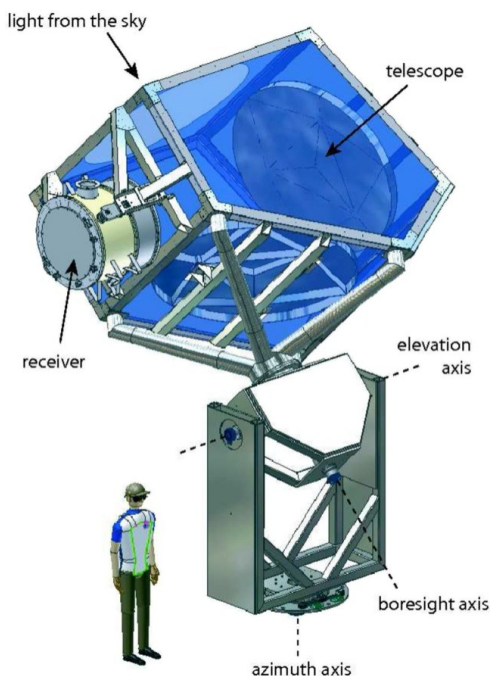
Figure 3.8: STRIP optical system and mount overview.

$(E_x - iE_y)/\sqrt{2}, (E_x + iE_y)/\sqrt{2}$, which are routed by the OMT to two different waveguides connected to the polarimeter module. The polarizer and OMT designs have been carried out in order to achieve high electrical performance (transmission $\gtrsim -0.5\,\text{dB}$, reflection $\lesssim -25\,\text{dB}$, cross-talk $\sim -40\,\text{dB}$ and leakage from intensity to polarization $\sim -30\,\text{dB}$) while containing the cost. More details about the polarizer can be found in Peverini et al., 2015.

Finally, the two circular polarization orthogonal components propagate through a polarimeter module, which amplifies and correlates the signals enabling the detection of the Q and U Stokes parameters. The design of the STRIP polarimeters is the same as the one proposed for the QUIET experiment (QUIET Collaboration et al., 2011), based on cryogenic High Electron Mobility Transistor (HEMT) low noise amplifiers and on high-performance waveguide components integrated in Monolithic Microwave Integrated circuits (MMIC). The STRIP Q-band channel is a combination of the original 19 QUIET Q-band modules and 30 units that were developed following the same design. The architecture and operation mode of polarimeters will be described more in detail in the next chapter.

The six W-band receivers have a very similar structure. The only difference is that the radiation from each feed horn enters a septum polarizer (Bornemann and Labay, 1995), which does the same job of the Q-band
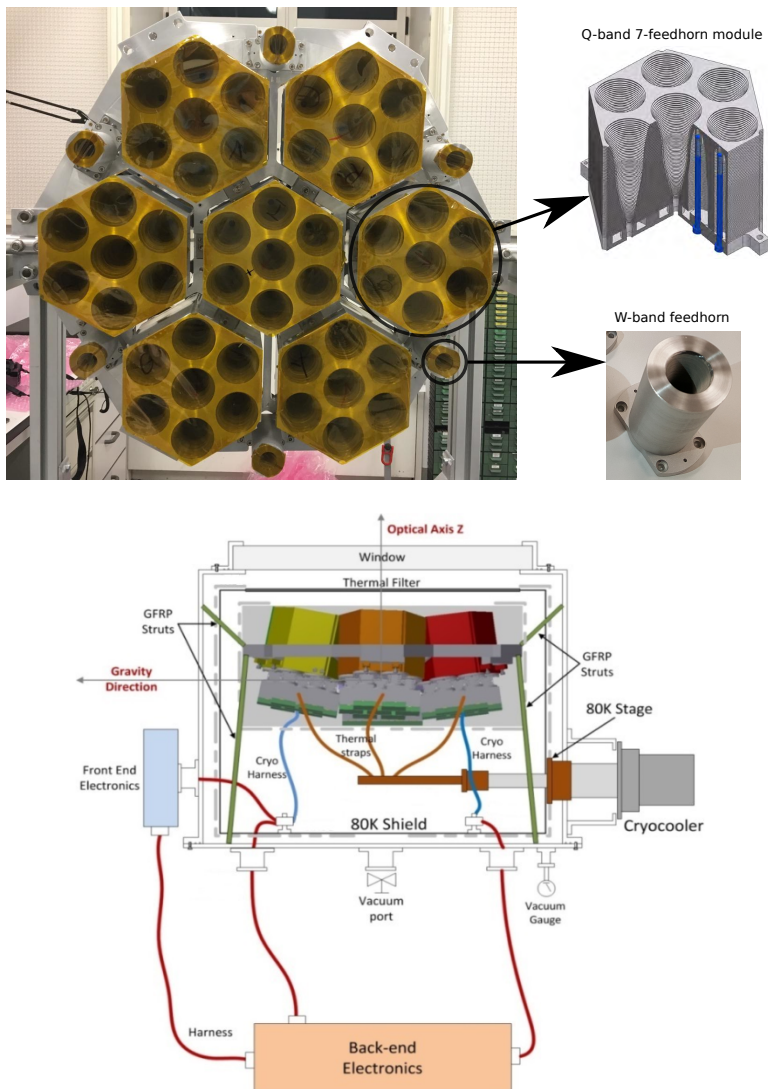
Figure 3.9: *Left*: overview of the STRIP fully integrated focal plane: the seven Q-band modules and the six W-band horns assembled in in the focal plane mechanical structure. The right panel shows a cutaway of one Q-band module (*top*) and the detailed view of one of the six W-band feedhorns (*bottom*). *Right*: Schematics of the STRIP instrument. The focal plane array is placed inside a cryostat surrounded by a 80 K shield.
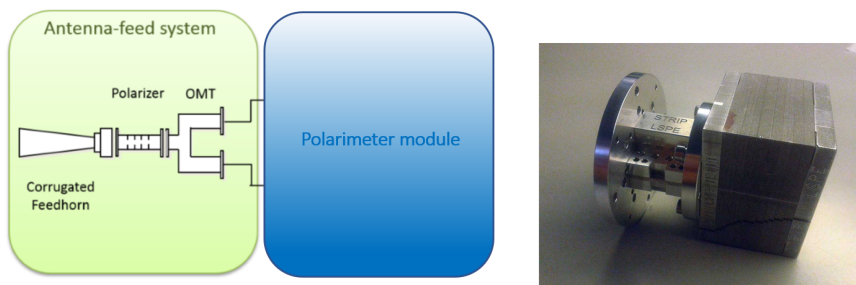
Figure 3.10: *Left*: Configuration of each Q-band receiver of the STRIP instrument. As explained in the text, the W-band receivers obtain the conversion from linear to circular polarization and the splitting of the two circular components by means of a septum polarizer, instead of the polarizer and OMT assembly. *Right*: Picture of the polarizer and the orthomode transducer assembled together (Franceschet et al., 2018).

polarizer and OMT sub-assembly: it separates the incoming radiation into left- and right-circularly polarized components. STRIP W-band channel uses the six original QUIET polarimeters used for the second season of observations (QUIET Collaboration et al., 2012), selected among those with the best performances.

3.2.4 Cryostat

The STRIP cryostat is designed to cool down the focal plane unit down to 20 K, with an external temperature typically in a range from 0°C and 24°C, and an average pressure of 760 mbar. As schematically displayed in the right panel of Figure 3.9, this is obtained by means of two-stage mechanical cryo-cooler. The first stage cools down to 80 K, a radiative shield which obstructs the parasitic heat leaks due to external radiation, harness or mechanical structures. The second-stage, the coldest one, allow cooling of the detectors array to 20 K, by means of copper thermal straps connecting the focal plane and the second-stage cooler cold head. The vacuum pressure required by the cryostat is $P \leq 10^{-4}$ mbar. The cryostat aperture is a polyethylene window with ultra-high molecular weight, followed by IR filters to reduce the radiative contribution from the 300 K environment.

One of the main issues of the cryostat design is the minimization of the parasitic heat leaks to the colder stage, which can be reached through an optimization of the material selection and the mechanical configuration. More details can be found in Franceschet et al. (2018).

3.2.5 Electronics

Seven twin boards drive and aquire the data of forty-nine Q-band and six W-band polarimeters. Each unit controls eight polarimeters, providing the biasing (48 HEMT LNAs, 16 phase-shifters and 32 GaAs detectors) and handing data aquisition. The acquisition board is equipped with logic (FPGA) to perform pre-analysis on the acquired data (high frequency demodulation, see next Chapter for explanation) and locally store the data.

3.2.6 Calibration

For STRIP there will be two calibration sub-systems: a near-field calibrator and a star tracker.

The near-field calibrator will provide a stable calibration signal for the entire duration of the mission. It will be produced by a couple of oscillators with electrically tunable frequency, one for the Q-band and one for the W-band. Each signal will be fed into a horn and placed in the region between the two telescope mirrors, directly illuminating the focal plane. Given the high power level of the oscillators (of order of 10–12 dBm), the sources will be suitably isolated and attenuated in order to avoid receivers saturation.

The telescope pointing accuracy, instead, will be addressed by a star tracker mounted on the baffle of the telescope. Observing the apparent position of a number of bright stars in the optical/IR band will allow us to accurately reconstruct the transformation matrix from the reference frame of the telescope (i.e. the relative motor positions) into the celestial sky frame. The star-tracker will consists in a high-speed camera coupled to a refractive telescope, resulting in a field of view of about 3°-5°.

Photometric calibration will be also performed on site, by means of a controlled power source operated on a flying drone that will allow us to reach a high signal-to-noise ratio, and by means of known astrophysics sources with a significantly polarized emission. Primary calibrators will be the Moon and the Crab Nebula. The Crab Nebula, in particular, is an ideal source for STRIP, being the brightest polarized point source in the sky and in the field of view of STRIP on each day of observation.

3.2.7 Scanning Strategy

The definition of the nominal scanning strategy of STRIP has been driven by several requirements: maximize the overlap with SWIPE sky coverage without compromising the sensitivity, homogenize the number of hits per pixel as much as possible over the covered sky area, minimize the radiation pickup from ground and check for availability of polarized calibration sources during observation (such as planets, the Crab Nebula, the Moon,
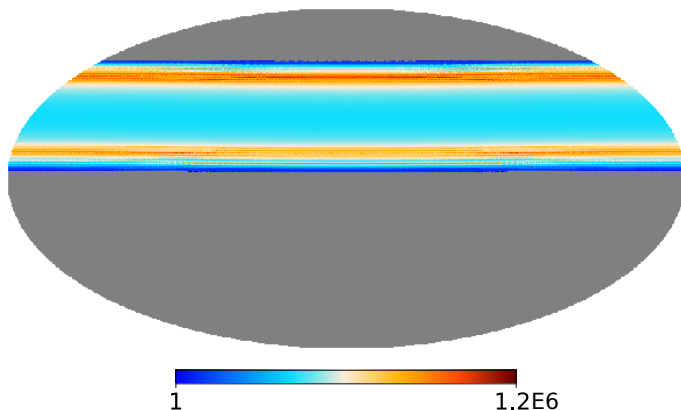
Figure 3.11: STRIP hitmap for the nominal scanning strategy: two years of observations with 35% duty cycle, 20°of elevation and spin period of 1 r.p.m.. Figure by Federico Incardona.

Perseus molecular complex and Orion nebula).

As a baseline, STRIP will scan the sky for two years with a continuous azimuthal spin at 1 r.p.m., while keeping the boresight elevation of a fixed angle (20°from the Zenith at Tenerife latitude). By combining the telescope spinning with the daily rotation of the Earth, STRIP will cover about the 37% of the Sky, with a 80% overlap with SWIPE as shown in Fig. 3.3. The area covered by both instruments will be about 25% of the Sky. The duty cicle will be of approximately 35%, taking into account the hours of the day when the Sun is too high for data taking and estimated days of bad weather occurring on average at the Teide Observatory. Figure 3.11 shows the simulated hitmap (in equatorial coordinates) for the baseline scanning strategy just destribed: thin stripes of highly populated pixels and lowly populated pixels at the edges, but a nice homogeneus coverage in the central area.

3.2.8   Sensitivity

There are several ways to express the instrumental sensitivity in CMB experiments, slight varations of the radiometer equation 2.6. The most common are:

- the **"1-second sensitivity"**, measured in $\mu K \sqrt{s}$, which gives the white noise standard deviation for a integration time of $1\,s$ for one radiometer. In other words, it is an estimate of the noise on a 1-second measurement by a single detector. For STRIP polarimeters (which measures Stokes parameters Q and U), the expression for the 1-second

sensitivity is:

$$\delta Q(U)_{1-\mathrm{sec}}(\mu\mathrm{K}\sqrt{\mathrm{s}}) = \frac{1}{\sqrt{2}} \frac{T_{\mathrm{sys}}}{\sqrt{\Delta\nu}} \tag{3.1}$$

where $\mathrm{T_{sys}}$ is the total intensity detected by the polarimeter and $\delta\nu$ is the receiver bandwidth.

- the **sensitivity per pixel**, measured in $\mu\mathrm{K}$, which gives the standard deviation of the white noise measured by the complete array of radiometers per observed sky pixel.

$$\delta Q(U)_{\mathrm{pix}}(\mu\mathrm{K}) = \frac{1}{\sqrt{2}} \frac{T_{\mathrm{sys}}}{\sqrt{\Delta\nu \cdot \tau_{\mathrm{pix}}}} \tag{3.2}$$

where τ_{pix} is the time spent on each pixel on average, assuming an approximately uniform scanning strategy. τ_{pix} can be computed as $\tau_{\mathrm{pix}} = \tau_{\mathrm{tot}}/\mathrm{N_{pix}}$, where τ_{tot} is the total mission duration and $\mathrm{N_{pix}}$ is the total number of pixels covered by the scanning strategy.

Basically, the 1-second sensitivity expresses the noise amount in the time domain, while the sensitivity per pixel expresses it in the map domain. The factor $1/\sqrt{2}$, present in both equations, results from the polarimeter correlation architecture (Bischoff et al., 2013). Table 3.2 shows the up-to-date estimations of the various contributions to the system temperature of STRIP polarimeters: sky signals (CMB and atmospheric emissions), emissions from the telescope components (mirrors, windows, feed system) and receiver noise temperature. The atmospheric emission has been computed by using the models ATM ("Atmospheric Transmission at Microwaves"; R. Pardo, Cernicharo, and Serabyn, 2002), and AM, developed by Scott Paine at Harvard University ((Paine, 2019))[3] The reported estimate for polarimeter noise temperature is the mean value of the noise temperatures of all 49 STRIP polarimeters, measured during unit tests, and it is therefore just a representative value. Summing all the contributions, we obtain $T_{\mathrm{sys}} = 60.9\,\mathrm{K}$ for the Q-band modules and a $T_{\mathrm{sys}} = 134.7\,\mathrm{K}$ for the W-band modules. Using equation 3.1 with these values, we get a 1-second sensitivity per polarimeter of $539\,\mu K \sqrt{\mathrm{s}}$ for the Q-band and $1347\,\mu K \sqrt{\mathrm{s}}$ for the W-band. By using equation 3.2, we can also calculate the sensitivity per arcmin pixels, obtaining $122\,\mu K \cdot \mathrm{arcmin}$ and $874\,\mu K \cdot \mathrm{arcmin}$ respectively for the Q- and the W-band.

---

[3]Actually, a recent more precise computation, done after the conclusion of this PhD thesis, suggests a slightly lower value for the atmospheric temperature at the Zenith, of about 16.5 K for the Q-band and 19 K for the W-band. We reports the older values, as all the studies performed in this thesis refers to them.

Table 3.2: White noise properties of the STRIP instrument

	43 GHz	95 GHz
Sky signals in antenna temperature		
Atmospheric emission along the Zenith [K]	18.0	21.0
CMB [K]	1.8	1.1
Noise contributions		
Mirrors emission [K]	3.0	3.0
Windows [K]	4.0	5.0
Feed system [K]	0.5	0.5
Polarimeter noise [K]	33.6	104.2
System temperature (T_{sys}) [K]	60.9	134.7

Chapter 4

STRIP Polarimeters unit tests

4.1 STRIP Polarimeter modules

Both Q-band and W-band channels of the STRIP instrument are based on coherent polarimeters built on a design originally developed for the QUIET experiment (QUIET Collaboration et al., 2011). They are based on cryogenic High Electon Mobility Transistors (HEMT) low noise amplifier (LNA) with phase-sensitive technique, following the tradition of polarization-sensitive experiments such as CBI (Padin et al., 2002), PIQUE and CAPMAP (Barkats et al., 2005), COMPASS (Farese et al., 2004), WMAP (Jarosik et al., 2003) and Planck-LFI (Bersanelli, M. et al., 2010). Unlike those experiments, however, QUIET and STRIP use a miniaturized design suitable for large arrays, replacing many waveguide components with a Monolitic Microwave Integrated Circuit (MMIC) device. As shown in Figure 4.1, all electrical components are contained in a compact package, which is coupled to a waveguide for signal input and feedthrough pins for biasing and redout. Thanks to this great compactness effort, the polarimeter modules have a footprint of just $5\,\mathrm{cm}\times5\,\mathrm{cm}$ (Q-band) and $2.5\,\mathrm{cm}\times2.5\,\mathrm{cm}$ (W-band).

Another great advantage of the QUIET/STRIP polarimeter scheme is that a single module can simulaneosly measure both Stokes parameters for linear polarization. Past experiments such as Planck-LFI, primarily designed to measure CMB temperature anisotropies, were able to detect just the total power of the two linear polarization components, $|E_x|^2, |E_y|^2$. Stokes Q was then obtained by making the difference $|E_x|^2 - |E_y|^2$, but to get Stokes U a second receiver rotated by 45° was inevitably needed. By meausuring
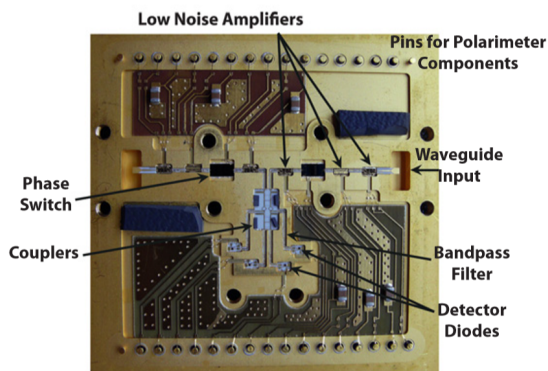
Figure 4.1: Internal view of a $5\,\mathrm{cm} \times 5\,\mathrm{cm}$ Q-band module. All components are integrated in a single MMIC device.

both Stokes Q and U at once, STRIP modules effectively double the number of detectors sensitive to polarization and introduce additional systematics checks, since the measurement of Q and U share the same microwave circuit.

4.1.1   Components

Figure 4.2 shows a schematic of a STRIP polarimeter module together with the input waveguide elements (feed-horn, septum polarizer and OMT) described in the previous chapter. The septum polarizer-OMT module splits the signal collected by the corrugated feed-horn into its left and right circular polarization components and link them to the polarimeter. The disctinctive feature of the module is the schematic division of the signal into two legs for amplification, which is afterwards combined again to perform correlation. In the following, a brief description of the main components of the polarimeter modules is provided.

4.1.1.1   Low noise Amplifiers

The six low-noise amplifiers used in STRIP modules are indium-phosphide HEMTs, deployed in series on the two aplification legs (three on one leg and three on the other). In Figure 4.2 they are indicated as H1, H2, H3, H4, H5, H6. The three amplifier in cascade form a single amplification stage with the resulting gain equal to the product of the three amplifiers. The amplifying chain of one leg is therefore denoted just by one gain term, g_A for legA and g_B for legB. Being active electronic components, the amplifiers will add noise to the microwave signal. In order to minimize the noise, STRIP

modules operates at the cryogenic temperature of 20 K. The amplifier gain ($\sim$25 dB) is sufficiently large that to the overall module noise is ultimately determined only by the first stage amplifier.

To turn on an amplifier, one should provide bias current to the transistor drains and bias voltage to the gates. These biases must be carefully tuned for each module to get the best possible performance from the device, that is to say highest possible gain and lowest possible noise.

4.1.1.2 Phase Switches

Between the second and third stage of amplification on each leg there is a phase switch. It is basically a fork that splits the signal path into two branches (*v1* and *v2* in Figure 4.2). One has ideally no phase delay and the signal passes unaltered, while the second one (*v2*) follows a longer optical path that injects a 180°phase shift in the electromagnetic wave. If the input signal splits equally between the two branches and then is recombined, it will result in a strongly attenuated output, because of destructive interference. In normal operation, however, the input signal passes through only one leg or the other. Given the association "1: open branch" and "0: closed branch", we can have four possible states: the 11 and 00 states both results in a strongly attenuated signal, while the 10 and 01 states both transmit signal, unaltered and delayed by 180°respectively.

4.1.1.3 Hybrid Coupler

After the amplification and phase-switch stages, the signals of the two legs are coupled again by a 180° hybrid coupler, which outputs the sum (0° phase-shift) and the difference (180° phase-shift) of the input signals. These two signals are then passed through a power splitter, in order to obtain four different outputs: two are immediately diverted to the *Q1* and *Q2* detector diodes to calculate the Q Stokes parameter, the other two signals pass through a 90°hybrid which again sums the input signals, but with relative phase shifts of 90° and 270°. The resulting outputs finally goes to the *U1* and *U2* diodes, to measure the U Stokes parameter.

4.1.1.4 Bandpass Filters

Bandpass filters are located between the hybrid coupler outputs and the detector diodes and also between the phase switches and the first stage amplifiers. These filters are used to exploit the maximum range of frequencies where the module has good sensitivity, but to remove signals outside the range of good performance of the LNAs, which would only contribute with extra noise.

4.1.1.5   Detector Diodes

After being filtered, each of the four outputs is terminated on a detector diode. A diode is able to turn the input RF power to a DC voltage by virtue of its non-linear I-V curve. Diodes have a quadratic response: in the small signal limit, the measured voltage is proportional to the square of the amplitude of the RF signal. STRIP module diodes are zero-bias at room temperature, but a voltage supply has to be provided at cryogenic temperature as the diode I-V curve changes dramatically when cooled. As we will see in the next Section, the outputs of *Q1* and *Q2* and of *U1* and *U2* can be directly combined to obtain Stokes Q and U parameters respectively.

4.1.2   Basic theory of operation

This section contains a brief description of how a STRIP module measure polarization. The reference is Colin Bishoff's PhD Thesis (Bischoff, 2010) from QUIET collaboration, which provides a more detailed description.
To account for the effect of every active component inside the polarimeter on the input signal, we use a matrix formalism. Let us write the two circular polarization components in input as a two-dimensional vector:

$$\begin{pmatrix} E_L \\ E_R \end{pmatrix} = \begin{pmatrix} \frac{E_x + E_y}{\sqrt{2}} \\ \frac{E_x + E_y}{\sqrt{2}} \end{pmatrix}.$$

The effect of the module components will be:

- Amplifiers and phase switches:

$$\begin{pmatrix} g_A \cdot e^{i\Phi_A} & 0 \\ 0 & g_B \cdot e^{i\Phi_B}, \end{pmatrix}$$

  where g_A and g_B are the gain factors for leg A and leg B respectively (lumping together the three amplifier in each leg), and Φ_A and Φ_B are the phase shifts introduced by the phase-switcher in each leg.

- Hybrid 180°:

$$\frac{1}{\sqrt{2}} \begin{pmatrix} 1 & 1 \\ 1 & -1 \end{pmatrix}.$$

- Hybrid 90°:

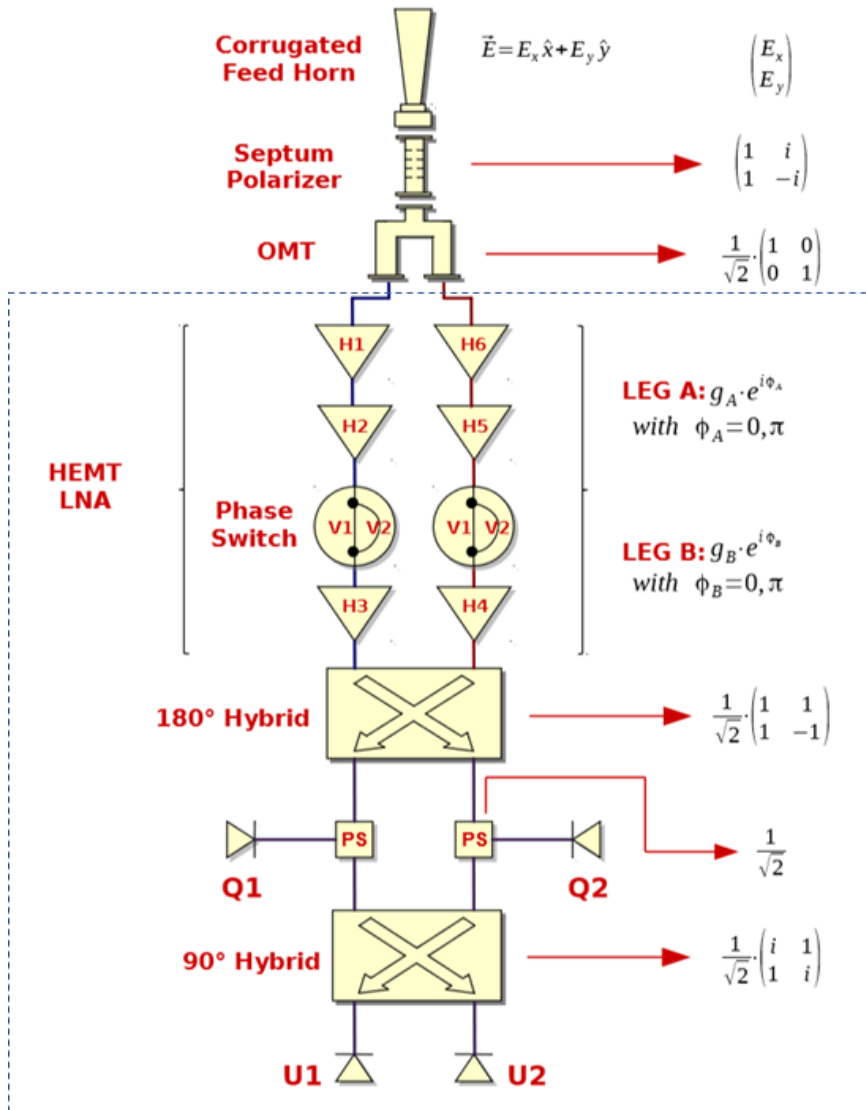$$\frac{1}{\sqrt{2}} \begin{pmatrix} i & 1 \\ 1 & 1 \end{pmatrix}.$$

Figure 4.2: Schematic diagram of a QUIET polarimeter module. The components labeled on the diagram are described in the body of the text. The dashed line encloses the components which are phisically integrated in the polarimeter module.

- Power splitter:

$$\frac{1}{\sqrt{2}} \begin{pmatrix} 1 & 0 \\ 0 & 1 \end{pmatrix}.$$

With a little algebra, one can calculate the output signal on each detector. For detector Q1, we get:

$$|E_Q 1|^2 = \frac{1}{4} |E_{legA} + E_{legB}|^2 \tag{4.1}$$

$$= \frac{1}{4} |g_A e^{i\Phi_A} E_L + g_B e^{i\Phi_B} E_R|^2 \tag{4.2}$$

$$= \frac{1}{4} [g^2 I + g_A g_B \cdot \cos \Delta\Phi \cdot Q - g_A g_B \cdot \sin \Delta\Phi \cdot U + \frac{g_A^2 - g_B^2}{2} \cdot V], \tag{4.3}$$

where $g^2 = \frac{g_A^2 + g_B^2}{2}$ and a $\Delta\Phi = \Phi_A - \Phi_B$, namely the phase difference between the two legs introduced by the phase switcher. I, Q, U and V are the Stokes parameters, defined as:

$$I \equiv |E_x|^2 + |E_y|^2,$$
$$Q \equiv |E_x|^2 - |E_y|^2,$$
$$U \equiv 2Re(E_x E_y^*) = E_x^* E_y + E_x E_y^*,$$
$$V \equiv 2Im(E_x E_y^*) = i(E_x^* E_y + E_x E_y^*).$$

Similarly, we can compute the expressions for the other detectors:

$$|E_{Q2}|^2 = \frac{1}{4} |E_{legA} - E_{legB}|^2$$

$$= \frac{1}{4} [g^2 I - g_A g_B \cdot \cos \Delta\Phi \cdot Q + g_A g_B \cdot \sin \Delta\Phi \cdot U + \frac{g_A^2 - g_B^2}{2} \cdot V],$$

$$|E_{U1}|^2 = \frac{1}{4} |E_{legA} - iE_{legB}|^2$$

$$= \frac{1}{4} [g^2 I + g_A g_B \cdot \sin \Delta\Phi \cdot Q + g_A g_B \cdot \cos \Delta\Phi \cdot U + \frac{g_A^2 - g_B^2}{2} \cdot V],$$

$$|E_{U2}|^2 = \frac{1}{4} |E_{legA} + iE_{legB}|^2$$

$$= \frac{1}{4}[g^2 I - g_A g_B \cdot \sin \Delta\Phi \cdot Q - g_A g_B \cdot \cos \Delta\Phi \cdot U + \frac{g_A^2 - g_B^2}{2} \cdot V].$$

In principle, Since $\Delta\Phi$ can just be 0 or π, then:

$$\sin \Delta\Phi = 0,$$
$$\cos \Delta\Phi = \pm 1$$

(+1 when $\Delta\Phi = 0$ and -1 when $\Delta\Phi = \pi$). This makes the U-leakage in the Q diodes and the Q-leakage in the U diodes signal disappear. We also assume a "perfectly balanced" polarimeter, that is to say equal gains for legA and legB:

$$g_A = g_B =: g. \tag{4.4}$$

With these assumptions the equations assume a very simple form:

$$|E_{Q1}|^2 = \frac{1}{4}g^2[I \pm Q], \tag{4.5}$$

$$|E_{Q2}|^2 = \frac{1}{4}g^2[I \mp Q], \tag{4.6}$$

$$|E_{U1}|^2 = \frac{1}{4}g^2[I \pm U], \tag{4.7}$$

$$|E_{U2}|^2 = \frac{1}{4}g^2[I \mp U]. \tag{4.8}$$

All the signals measured at the four detector diodes share the same first term, proportional to the total intensity of the input signal (Stokes I), multiplied by a gain factor. An important thing to note is that this term does not change sign when the phase switch state flips. The second term in these equations, instead, all do change sign with the phase switch state.

Given these equations, the Stokes parameters can be extracted automatically from the detector outputs by performing a **double demodulation**. The polarimeter module is designed to let the two phase switches work at two different frequency rates (4 kHz and 100 Hz), as shown in Figure .

The demodulation automatically carried out by the data acquisition sofware consists of two stages. During the first demodulation, the software simply subtract two signals acquired in two contiguous but opposite phase state of the fast modulated phase switch ($S_{A1} - S_{A0}$). During 40 cycles (40 data acquired with phase-switch state 0 and 40 with phase-switch state 1, that means 40 differences recorded) of the fast switch, the slow one remains in the same phase state. The software averages these 40 samples so that there is always one measurement for each slow switch phase state (S_{B0}). Subtracting two contiguous data (S_{B0} and S_{B1}), we get the final double demodulated data:
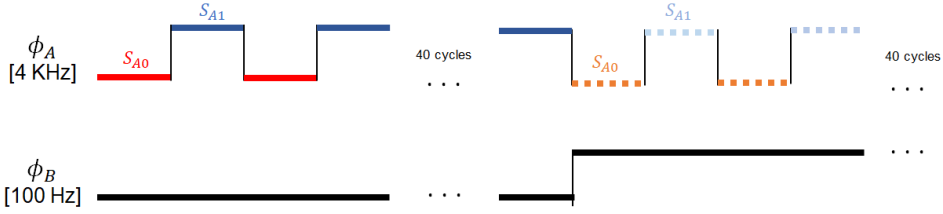
Figure 4.3: A brief description of how the double demodulation works. The two
phase switch work at two different frequency rates , 4 kHz and 100 Hz.
Blue and red (light blue and orange) lines stand for signal acquired at
one diode in two different states of the fast phase switch, while the slow
phase switch stands in a fixed state.

$$|E_{Q1}|^2_{\mathrm{DEM}} = \frac{1}{4}g^2[(I \pm Q) - (I \mp Q)] - [(I \mp Q) - (I \pm Q)],$$
$$= \pm g^2 Q,$$
$$|E_{Q2}|^2_{\mathrm{DEM}} = \mp g^2 Q,$$
$$|E_{U1}|^2_{\mathrm{DEM}} = \pm g^2 U,$$
$$|E_{U2}|^2_{\mathrm{DEM}} = \mp g^2 Q.$$

With the double-demodulation expedient, the $Q1$ and $Q2$ diodes and the
$U1$ and $U2$ diodes both directly measure the Stokes parameter Q and U
respectively, with a sign depending to the phase-switch state. By doing
a difference between the outputs of $Q1$ and $Q2$ (and of $U1$ and $U2$), we
finally get Q and U (multiplied by the same numeric term), removing the
dependence on the phase-switch state:

$$\frac{|E_{Q1}|^2_{\mathrm{DEM}} - |E_{Q2}|^2_{\mathrm{DEM}}}{2} = g^2 \cdot Q, \tag{4.9}$$

$$\frac{|E_{U1}|^2_{\mathrm{DEM}} - |E_{U2}|^2_{\mathrm{DEM}}}{2} = g^2 \cdot U. \tag{4.10}$$

If we instead compute the sum of the signals in different phase-switch states, we get:

$$|E_{Q1}|^2_{\text{PWR}} = \frac{1}{4}g^2[(I \pm Q) + (I \mp Q)] + [(I \mp Q) + (I \pm Q)]$$
$$= \pm g^2 I,$$
$$|E_{Q2}|^2_{\text{PWR}} = \mp g^2 I,$$
$$|E_{U1}|^2_{\text{PWR}} = \pm g^2 I,$$
$$|E_{U2}|^2_{\text{PWR}} = \mp g^2 I.$$

By summing all the outputs, we obtain:

$$\frac{|E_{Q1}|^2_{\text{PWR}} + |E_{Q2}|^2_{\text{PWR}} + |E_{U1}|^2_{\text{PWR}} + |E_{U2}|^2_{\text{PWR}}}{4} = I, \tag{4.11}$$

which means that STRIP polarimeters are able to measure both the total power of the input radiation and the polarized component.

Besides providing a direct measurement of the Stokes parameters, the double-demodulation approach brings other benefits:

- The amplifiers used in STRIP modules produce noise following an *1/f* spectrum. The power output of the LNAs is dominated by this noise tipically for frequencies less than few hundred Hz (for Q-band). Since the total intensity I is obtained from a sum of the signal over the two phase-switch states, it is affected by a high level of *1/f* noise, making STRIP polarimeters not suitable for total power measurements. However, the measure of Q and U results from a difference and cancels very efficiently *1/f* noise. A high demodulation rate ($\sim$ kHz) makes the suppression more effective. Figure 4.4 illustrates the vast difference in noise between the averaged and the demodulated data.

- Ideally, switching the phase-switch state affects only the phase of the signal, leaving its amplitude unchanged. In practice, non-idealities in the electronic components can make the phase-switch transmission amplitude different in the two states. This causes the appearance of a term proportional to Stokes parameter I in the 1°-demodulated signal, leaking the temperature signal into the polarization measurement (Bischoff, 2010). The I→Q and I→U leakage due to phase-switch imbalance can be eliminated through double demodulation.

We have seen that the architecture of STRIP polarimeters allows us to measure directly both Stokes parameters Q and U from a single measurement. We remind that this is true under some assumptions about the ideality of the electronic components of the modules, for example:
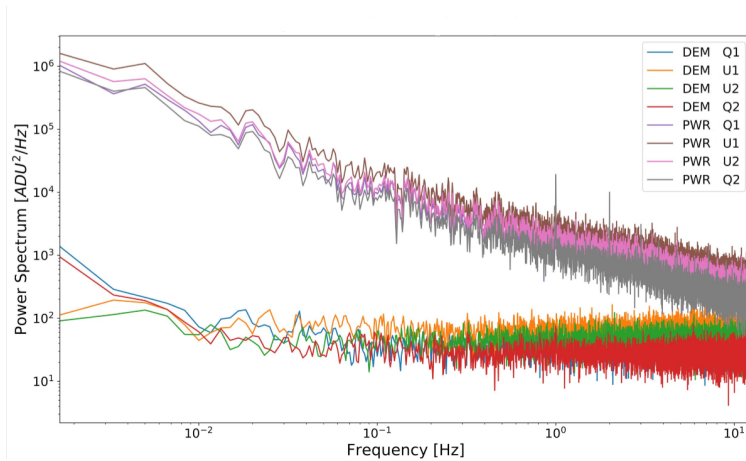
Figure 4.4: Noise power spectra for averaged and demodulated data taken by a
STRIP polarimeter during unit tests. The output of all four detectors
is shown. The fast demodulation suppresses the 1/f noise power by a
factor of nearly 10^5.

- The amplifiers do not introduce a phase difference between the two
  legs.

- The phase difference introduced by the phase switch is exactly 0 or
  exactly 180°.

- The two hybrid couplers do not introduce any attenuations or phase
  imbalance.

- The power splitter exactly splits the signal in two.

In presence of such non-idealities, the output signals of the four diodes
would contain leakage terms eliminable by the demodulation, causing
systematic errors in the measurement.

4.2   Unit tests

STRIP polarimeters (both Q-band and W-band) have been characterized
during the Unit Test Campaign, both at room temperature and in cryogenic
conditions to evaluate their functionality and performance. The tests took
place approximately from March 2017 to April 2018 at the Cryogenic Mil-
limetre Laboratory of the University of Milano-Bicocca. We had 70 Q-band
polarimeters available for testing: 19 QUIET modules, made available by
the QUIET team after the conclusion of the project, and 51 polarimeters
specifically built for STRIP at NASA JPL (Jet Propulsion Laboratory) in

Pasadena, California. On the other side, all the 10 W-band polarimeters we tested were the ones used in the QUIET experiment. Actually, only 56 polarimeters out of 70 available were tested: the others were affected by major malfunction of some harware components that made the characterization impossible. The number of polarimeters available was beyond the STRIP required number for both Q-band and W-band (49 and 6 polarimeters respectively), allowing us to choose the polarimeters to put on the focal plane from those with the best performance. All tests have been perfomed at the cryogenic temperature of 20 K, the working temperature at which STRIP will acquire data in Tenerife.

The characterization tests performed were the following:

- DC characterizations, first at room temperature to check the health of the active electronic components, and then at cryogenic temperature (20 K).

- Radio-frequency (RF) test, for bandpass response characterization.

- Y-factor test, for T_{noise} estimation.

- Long acquisition, for 1/f noise characterization.

Complete reports for each test are publicly available at `https://striptest.fisica.unimi.it/unittests/`, as well as analysis code on GitHub `https://github.com/lspestrip/striptun`.

During my PhD activity I actively participate to the STRIP unit test as an operator in the laboratory and also to the data analysis, focusing in particular on the analysis of the bandpass response, which will be described in detail.

4.2.1 Setup description

During the characterization tests, we put the polarimeter inside a vacuum chamber connected to an electronic board for biasing and data acquisition. The vacuum chamber housing the polarimeter under test is an aluminum chamber of internal dimensions $550 \times 450 \times 250$ mm. Vacuum is obtained by the joint action of a scroll primary pump and a turbo pump, able to reach the minimum pressure of 10^{-6} mbar. Cryogenic temperature is reached by a two-stage cryo-cooler, able to span a range of temperature from 4 K to 300 K.

Figure 4.5 sketches the experimental setup used during Bicocca's unit tests. A comparison with the scheme in Figure 4.2 reveals that the feed-horn, the septum polarizer and the OMT have been replaced by other electronic components: an RF generator, a cross guide, a magic-T and two resistive loads, both with controlled temperatures via heaters.

The cross guide allows to couple two signals, in this case respectively coming from one of the two loads and the other from the RF generator. The magic-T is substantially equivalent to a 180° hybrid coupler, therefore producing in output the sum and the difference of the input signals. The two outputs of the Magic-T are then connected to the input ports of the polarimeter. As we will see later on, the RF generator is necessary for the bandpass characterization test, while the two loads are needed to perform the T_{noise} measurement.

Since the components between the input loads and the polarimeter module have changed, the expression of the output signal of the four diodes in this experimental setup is not the same of equations 4.8, but becomes:

$$|E_{Q1}|^2 = \frac{1}{2}g^2[E_A^2 + E_{RF}^2], \tag{4.12}$$

$$|E_{Q2}|^2 = \frac{1}{2}g^2[E_B^2], \tag{4.13}$$

$$|E_{U1}|^2 = \frac{1}{4}g^2[E_A^2 + E_{RF}^2 + E_B^2], \tag{4.14}$$

$$|E_{U2}|^2 = \frac{1}{4}g^2[E_A^2 + E_{RF}^2 + E_B^2], \tag{4.15}$$

where we have assumed a perfectly balanced polarimeter and $\Delta\Phi = 0$. When $\Delta\Phi = \pm\pi$ the signal on Q_1 and Q_2 exchange each other.

Even if not strictly necessary for being able to measure the polarization, the LNAs were biased with the purpose to make the polarimeter as balanced as possible. In this way, we can directly refer to the simple equations 4.15, making the intepretation of the data much easier .

All the critical device temperatures (polarimeter, magic-T, cross guide and the two loads) are regulated by thermostats, which are able to stabilise them better than ± 0.001 K. Calibrated thermometers are used to monitor the temperatures inside the cryofacility. The load temperatures can be risen or lowered from the polarimeter working temperature (20 K).

A control software, developed using LabVIEW, allows the operator to supply the desired bias parameters to the detectors, to the HEMTS/LNAs and to the phase switch, to perform data acquisition, to read the outputs of the detectors and to write them in text files.

A complete battery of tests for each polarimeter lasted at least two days: one work day with an operator to perform the tests, a long acquisition during the night to characterize 1/f noise, one half-day to cool the cryo-chamber down to 20 K and another half-day to bring it back to room temperature.
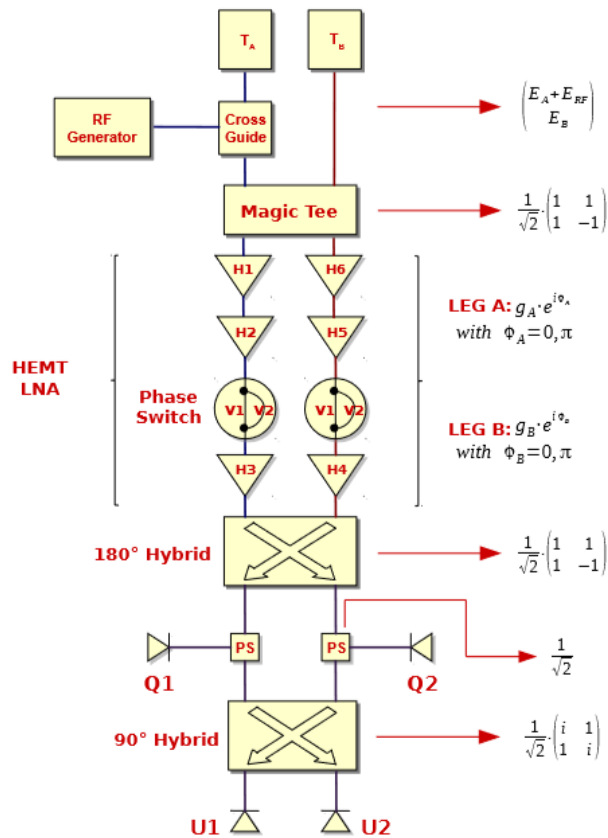
Figure 4.5: Schematic diagram of a QUIET polarimeter module. The components labeled on the diagram are described in the body of the text. The dashed line encloses the components which are phisically integrated in the polarimeter module.
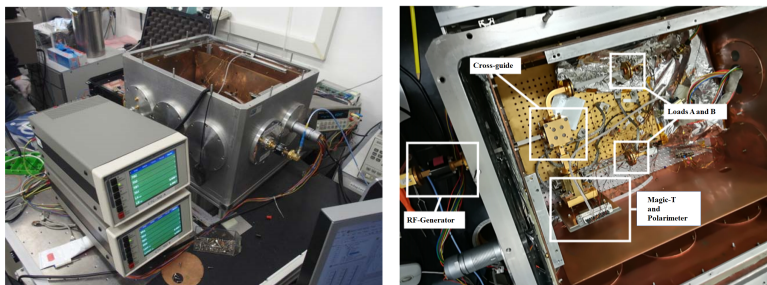

Figure 4.6: *Left*: the vacuum chamber (open) used for the unit tests. The two deviced on the left are used to monitor the temperature of the setup components and to change the two loads temperature during the Y-facto twst. *Right*: the test experimental setup inside the cryofacility.

4.2.2   DC characterization

DC tests are intended to evaluate the correct functioning of the active components of the polarimeter modules: low noise amplifiers, detector diodes and phase switches. The DC tests have been performed using a characterization system manufactured by Keithley (model 4200-SCS). It is a parameter analyzer for the characterization of seminconductor devices with a very high sensitivity and accuracy, allowing a great variety of characterization tests. Every electronic component of the module has been individually tested, verifying its behaviour over a range of input biases.

4.2.3   Bandpass response

This Section reports a detailed description of the bandpass response test and its data analysis, which has been one of the first activities of my PhD. This test aims to characterize the response of each polarimeter to input signals of different frequency. In particular, we used a RF generator to inject a single-tone signal into the receiver. We used frequencies in the range 38–50 GHz for Q-band [1] and 80–109.5 GHz for W-band, with steps of 0.1 GHz, and we measured the output signal as a function of frequency. Bandpasses were measured for each diode of each module, that is to say that we have four output signals for each bandpass test. Each test has been performed with a fixed phase-switch configuration (disabling the demodulation). We remember that the possible phase-switch configurations (i.e., those trasmitting signal) are:

- 0101: both phase-switches trasmit a signal delayed by $180°$ ($\Delta\Phi = 0°$);

- 1010: both phase-switches trasmit an unaltered signal ($\Delta\Phi = 0°$);

- 0110 and 1001: one of the two phase-switches trasmit an unaltered signal, and the other one trasmits a $180°$-delayed signal ($\Delta\Phi = 180°$).

Given a phase-switch configuration, one of the four detectors is "blind", namely not sensitive to the variation of the injected signal ($Q2$ for 0101/1010 and $Q1$ for 0110/1001). Therefore, in order to get information on all the detectors, the bandpass test has been repeated twice for each polarimeter, one time for each phase-switch configuration (0101 and 0110, the other two configurations are equivalent).

Before performing the complete bandpass test, we actually work on the LNAs biases in order to balance the polarimeter. Thanks to the strength of the RF generator signal, it is possible to verify if the gains are balanced in

---

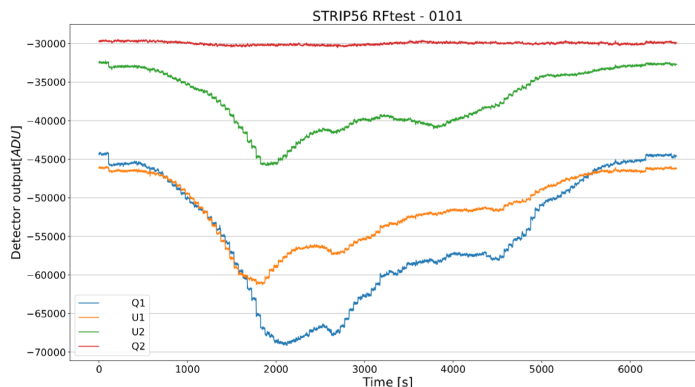[1] Actually, for the last ~ 20 polarimeter tested, the range was enlarged to 36–50 GHz

Figure 4.7: Raw output of the bandpass test for the STRIP56 polarimeter, performed with phase-switch configuration: 0101. The output signal of the four diodes is reported ($Q2$ is blind, as expected). The negative sign is just due to ADC conversion.

real time: since the RF signal is injected in only one of the two inputs (legA), Eq. 4.15 implies that when the phases are set either on 0101 or on 1010 state, $Q2$ would insensitive to the RF signal. This, however, happens only in case of perfect balance; otherwise, we would see both $Q1$ and $Q2$ sensitive to the extra signal injected by the RF generator. If the phases are set either on 1001 or on 0110 state, the roles of $Q2$ and $Q2$ would swap.

Figure 4.7 reports the raw output of the 0101 bandpass test for the STRIP56 polarimeter as an example. We can see from Fig. 4.7 that four detectors can produce very different output powers. This is mostly due to the presence of an electronic offset, set by hand by the operator in order to avoid saturation of the ADC. To correctly compute the bandwidth and the central frequency, we must carefully estimate the offset and subtract it from data. A tricky thing to take into account is the small "steps" that appear in the detector outputs at the switching on/off of the generator. These steps are due to the fact that the polarimeter is slightly sensitive even outside the 38-50 GHz range. After discovering this behaviour (for the last ~ 20 polarimeters tested) we extended the swept range to 36 GHz and the lower step disappeared. Unfortunately, it was not possible to test higher frequencies, since 50 GHz was the highest frequency allowed by our generator. To estimate the electronic offset for the four detectors, we took the mean value of the output before the switching on and after the switching off of the generator, we perform a linear fit between these to points and used it as offset. In this way, we automatically take into account possible drifts of the electronics during the test period. Figure 4.8 shows the output signal of the
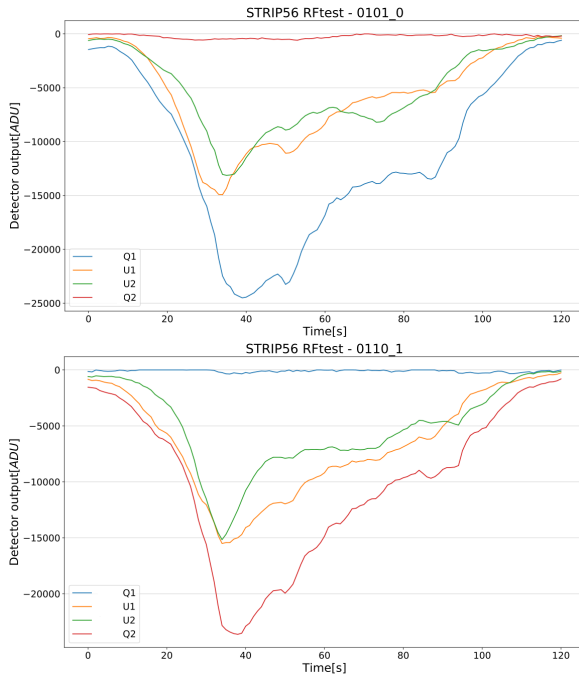
Figure 4.8: Output of the bandpass test for the STRIP56 polarimeter, after the subtraction of the electronic offset. *Up*: test performed with phase-switch configuration: 0101. *Down*: test performed with phase-switch configuration: 0110.

four diodes of the STRIP56 polarimeter after having removed the electronic offset. Both tests performed with different phase-switch configuration are reported.

The bandpass measurements can be used to calculate bandwidth and central frequency. We adopted the same definitions used for the characterization of QUIET modules (Newburgh, 2010):

$$BW = \frac{(\int I(\nu)\sigma(\nu)d\nu)^2}{\int (I(\nu)\sigma(\nu))^2 d\nu}, \tag{4.16}$$

$$\nu_c = \frac{\int \nu I(\nu)\sigma(\nu)d\nu}{\int I(\nu)\sigma(\nu)d\nu}, \tag{4.17}$$

where $I(\nu)$ is the response of the detector and $\sigma(\nu)$ is the spectrum of the source in thermodynamic temperature units. In our case, the frequency steps are discrete and constant ($\Delta\nu = 0.1\,\text{GHz}$), and the signal generator is considered ideal, with flat bandpass in our range of interest ($\sigma(\nu) = 1$). Thus, the formulas above can be simplified as follows:

$$BW = \frac{[\sum I(\nu)]^2 \Delta\nu}{\sum [I(\nu)]^2},$$ (4.18)

$$\nu_c = \frac{\sum I(\nu)\nu}{\sum I(\nu)},$$ (4.19)

which are the equations used in the Python analysis code.

In principle, we can apply the formulae described in the previous section to every output signal we have. In other words, we can compute a bandwidth and a central frequency value for each detector, in both tests. The final step of the analysis is to put together all the information that we have from different detectors and different tests in order to get the best estimate of the polarimeter band. To to that we take the three non-blind outputs from each test ($Q2$ excluded if phase-switch configuration is 0101, $Q1$ excluded if 0110) and we normalize them to the maximum. We take the median of the six output values at each frequency as the best estimate of the polarimeter band . Figure 4.9 reports all the normalized detector outputs for STRIP56 together with the best band, shown in black. We compute also an error bar for the best band, by taking the difference between the 97.5 percentile and the 2.5 percentile of the distribution of the six output values at each frequency, which corresponds to a 95% confidence level. Figure 4.9 shows also the best band for STRIP56 together with its error bar. Finally, we take as best estimate of the bandwidth and the central frequency the bandwidth and the central frequency of the best bend. To estimate the error, we take the distributions of the bandwidth and the central frequency values calculated for the six detectors and we take the difference between the 97.5 percentile and the 2.5 percentile of these distributions.

Results and Discussion

The analysis code has been applied on all STRIP polarimeters band-pass tests, providing an estimation of the bandpass shape, of the central frequency and bandwidth of all polarimeters. The modules show a clear non uniformity in the shapes of the bandpasses. Some of them have very irregular bandshapes, with multiple peaks and great variability in single detector outputs. Others, instead, shows very regular bandshapes, with a clear single peak and with uniform bandshapes from single detector outputs. Most of the polarimeters, however, shows intermediate characteristics. Irregularity in bandshape can be due to non-idealities in the experimental setup, malfunction of some electronic component of the polarimeter or non optimized biases of the LNAs. Figure 4.10 shows three examples illustrating the three cases: STRIP02 for the " bad" case, STRIP31 for the "good" case
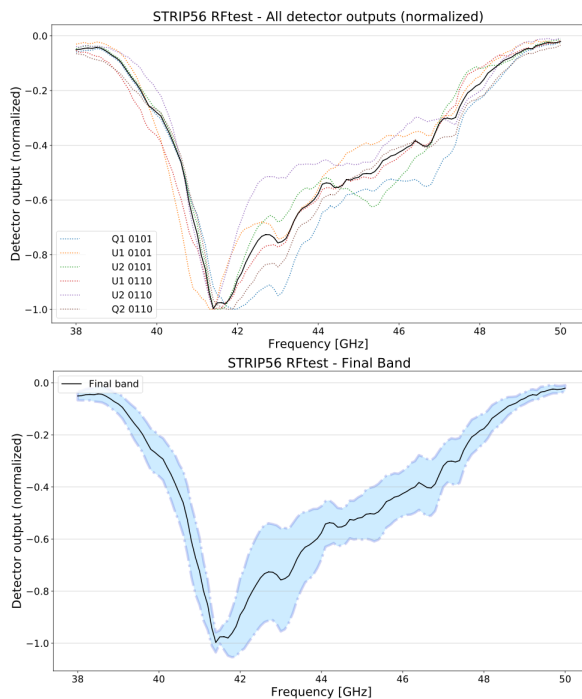
Figure 4.9: *Up*: all detector outputs from both bandpass tests (phase-switch config-
uration 0101 and 0110) for STRIP56 normalized to the maximum and
plotted together. The best estimate of the band is shown in black. *Down*:
the best estimate of the band for the STRIP56 polarimeter, together with
its error bar.

and STRIP37 for the "intermediate" case. The measured central frequencies
and bandwidths for all Q-band polarimeters are schematically reported in
the top panel of Figure 4.11. There is a clear dichotomy between the QUIET
polarimeters (from STRIP52 to STRIP70) and the other ones in terms of band-
width, as the former have a slightly larger $\Delta\nu$ ($\sim 8\,\text{GHz}$) with respect to the
others ($\Delta\nu \sim 6.5 \div 7.0\,\text{GHz}$). Having a larger bandwidth, QUIET modules
have a better sensitivity. On the other hand, all the polarimeters show a
remarkable agreement in the central frequency. The same plot, but for the
W-band, is shown in the bottom panel of Figure 4.11. The average central
frequency and bandwidth are $97\,\text{GHz}$ and $7\,\text{GHz}$ respectively, but with a
great variability of the bandwidth value from polarimeter to polarimeter.

4.2.4   Noise temperature

By increasing the temperature of one of the two matched loads, it is
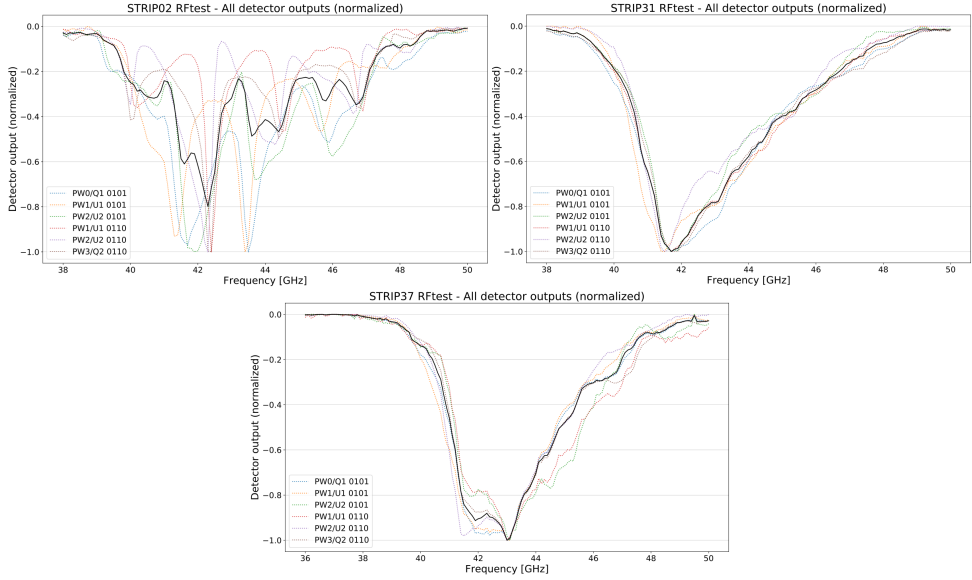possible to perform the standard technique called "Y-factor" to measure

Figure 4.10: *Up*: all detector outputs for STRIP02, STRIP31 and STRIP37, as examples of band, good and intermediate bandshape.

both the gain G (ADU/K) and the noise temperature T_{noise} of a polarimeter.

We can write the signal outputs due to two different input temperatures, T_1 and T_2, as:

$$V_1 = G(T_1 + T_{\text{noise}}),$$
$$V_2 = G(T_2 + T_{\text{noise}}).$$

If we define the Y-factor as the ratio between the voltages measured at the two different temperature steps, $Y = V_1/V_2$, we find an expression for T_{noise} and G depending on measured quantities:

$$T_{\text{noise}} = \frac{T_1 - Y T_2}{Y - 1}, \tag{4.20}$$

$$G = \frac{V_1 - V_2}{T_1 - T_2}. \tag{4.21}$$

The typical data for this kind of test is reported in Figure 4.12. Again, if the gains are well balanced, we expect that $Q1$ and $Q2$ exchange their roles when switching from phase state 1010 to 0101. When $Q1$ is sensitive $Q2$ is insensitive, and vice versa.

The STRIP polarimeters should exhibit the same level of noise temperature among the four output channels $Q1$, $Q2$, $U1$, and $U2$. However, to
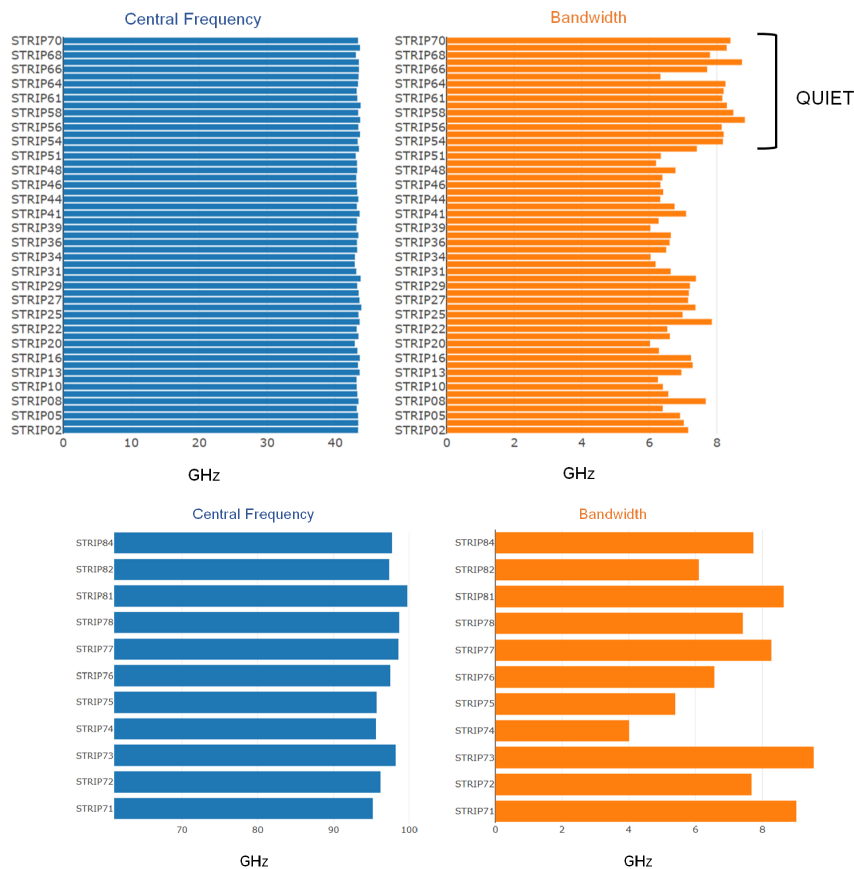
Figure 4.11: Central frequency and bandwidth of the tested polarimeters Results
for Q-band and W-band are shown in the *Top* and in the *Bottom* panel
respectively.

comply with the approach followed by the QUIET team, we decided that it
was better to concentrate the analysis on the two channels Q_1 and Q_2, as
these are the easiest to interpret.

For almost all the polarimeters, two noise temperature tests have been
performed: first the input load was warmed up, and then it was cooled
down again, stopping at the same temperature levels. This means that for
every polarimeter we have produced several noise temperature estimates.
For most of the polarimeters, at least 4 temperature steps were exercised, so
that there are 6 possible T_1, T_2 pairs for each detector $Q1$ and $Q2$ for each
test(warm-up or cool-down). Therefore, the overall number of samples is
of the order of 24 or more. In principle, all these measurementes should
produce the same estimate for T_{noise} using Eq. 4.20. In practice, this does
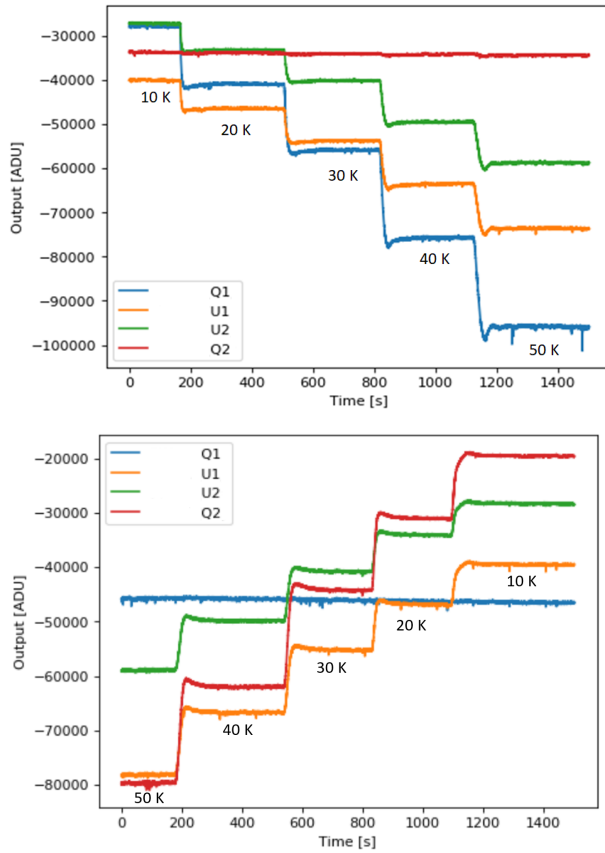not happen for our polarimeters because of many possible factors, such

Figure 4.12: Typical output of a Y-factor test performed with temperature steps of 10 K, 20 K, 30 K, 40 K, 50 K, on the *top* with rising temperature for phase state 0101, on the *bottom* with falling temperature for phase state 0110

as non-linearity in the detectors o imperfect knowledge of T_1 and T_2 (e.g. because of non-idealities in the polarimeters). In the performance table 4.1, the median value of the available T_{noise} is quoted as the best estimate and the 5° and 95° percentiles were used to fix the upper and lower error bars. So, for example, the number $41.3^{+7.0}_{-5.6}$ K means that 95 % of the estimates are within the range $[41.3 - 5.6, 41.3 + 7.0]$, and the median is 41.3 K. We were able to estimate the noise temperature for 54 polarimeters. The average value of T_{noise} is 43.6 K, which is however not representative as it includes more polarimeters than the ones that can be hosted in the focal plane. Taking the average of the 49 best noise temperatures, the average reduces to 33.6 K.

4.2.5 1/f characterization

To characterise *1/f* noise long acquisition in nominal operations was performed. Instead of blocking the phase shifters like in the other tests (Bandpass and T_{noise} tests) , they are let switch at the rates of $2\,\mathrm{kHz}$ and 50 Hz[2]. We took data for a certain amount of time with sampling rate of $25\,\mathrm{Hz}$, with the polarimeter observing two thermal loads at the temperature of $\sim 20\,\mathrm{K}$ and no signal injected by the RF generator. Depending on the time availability, long acquisitions can last for few hours (1-5) or for many hours (12-24). Unfortunaley, due to time constraints, this test was not performed on all available parameters, but just on a subset (42 modules for the Q-band).

Concerning the analysis, raw data $[\mathrm{ADU}]$ are first calibrated by subtracting the electronic offsets $[\mathrm{ADU}]$ and then dividing by the detector gains $[\mathrm{ADU/K}]$ obtained from the T_{noise} test. Then, the Power Spectral Densities (PSD) of the four detector outputs are estimated using Welch's method (Press, W. et al., 2007): the data stream is firstly divided into a number of chunks, then the PSD is computed for each chunk and finally the average PSD is calculated. In this way, lowest frequencies of the spectrum are lost but, in return, it is possible to obtain a more precise estimation of the white noise level and of the slope (α) of the *1/f* spectrum. The white noise level is estimated by computing the median value of the high frequency part of the spectrum, while the slope of the *1/f* spectrum is extracted through a linear fit of the low frequency part of the spectrum. Finally, by doing the intersection between the linear fit and the median, we get the knee frequency. The PSD for detector $Q1$ of polarimeter STRIP33 is reported in Figure 4.13 together with the analysis fit as an example. From the bottom panel of the same picture, showing the PSD of the Stokes parameters I, Q and U, we can appreciate the great noise reduction on the polarization signal performed by the demodulation technique.

4.2.6 Final results and discussion

Table 4.1 lists all the parameters derived from the unit tests performed in Bicocca for each polarimeter, namely T_{noise}, bandwidth, central frequency, white noise level $\Delta Q/U_{\mathrm{rms}}$, knee frequency and *1/f* slope. Polarimeters with empty line are modules that showed hardware mulfunctioning, making it impossibile to carry out the tests. The adopted criterion to choose the 49 modules, among the functioning and successfully tested polarimeters, to actually put on the STRIP focal plane was just the T_{noise} measurement. That is to say that the polarimeters with the worst T_{noise} (STRIP10, STRIP21,

---

[2]As mentioned in Section 4.1.2, the phase-switch rates during data acquisition in Tenerife will be higher, namely $4\,\mathrm{kHz}$ and $100\,\mathrm{Hz}$
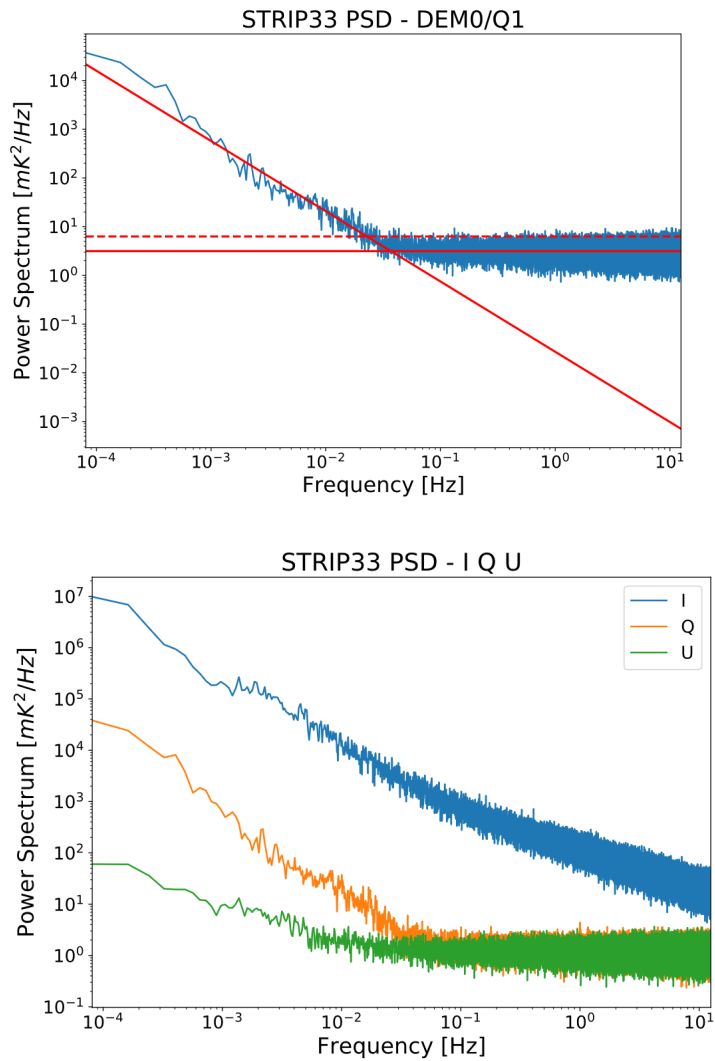
Figure 4.13: PSD of the output of detector Q1 of polarimeter STRIP33 (*top*) and of the Stokes parameters I, Q and U (*bottom*).

STRIP26, STRIP44), were discarded and kept as backup. STRIP68 was also rejected, as it began to show mulfunction after the test was performed (probably a component broke during operations). The final disposition of the polarimeters (both Q- and W-band) on the focal plane of STRIP is shown in Figure 4.14.

Looking at Table 4.1, we can see that the parameters estimated from the *1/f* test (white noise level, knee frequency and *1/f* slope) show very large uncertainty in some cases. This is an indication that the fit of the long acquisition data was not good. One possible explanation, valid for some tests, is simply the fact that they did not lasted long enough to clearly see the *1/f* rise. Another possibility is that some electric instabilities, that we know sometimes affected the power supply of the laboratory during the campaign, negatively affected data. Unfortunately, the acquisition software was not designed to acquire the housekeeping values (LNAs biases, temperatures etc.) over time, making it impossible to disentagle, in retrospect, the origin of the eventual badness of data: whether due to an intrinsic instability of the polarimeter or due to external causes.

The values of T_{noise} sometimes show huge error bars, even reaching negative values in some cases. As explained in section 4.2.4, for each polarimeters we had several estimates for the T_{noise}, as we performed the Y-factor test using several temperature steps. The error bars have not a real statistical meaning, but represents the variability of the available measurements. The sometimes negative values of T_{noise} are imputable to the fact that the ADC offset has not been characterized. The Y-factor equation 4.20, in fact, is valid only if we assume that the signal in ADU is proportional to the signal in Volt, which is not necessarily true. In general, the relation between ADU and Volt is more complex:

$$\mathrm{ADU} = g(V - V_0) + \mathrm{ADU}_0 \tag{4.22}$$

where g and ADU_0 are respectively the gain and the offset of the ADC. While V_0 is manually settable, g and ADU_0 are not known a priori and should be experimentally characterized. The presence of an additive factor can cause the Y-factor test to output a negative T_{noise}. The characterization of the ADC will be one of the numerous activities that will be performed during the system level tests campaign.

Besides for choosing which polarimeters to keep as spare units and which ones to integrate in the focal plane, the results of the unit tests have been used to decide how the 49 polarimeters had to be paired with each position in the seven 7-horn modules, taking into account a number of considerations regarding the scanning strategy and the noise characteristics of the polarimeters. Several combinations have been studied (e.g. most

performant polarimeters concentrated in the centre of the focal plane, uniform distribution according to the T_{noise} etc.) but no significant difference has emerged in the estimated overall instrument sensitivity per pixel. It was decided, therefore, to use a random receiver/horn pairing. The final disposition of the polarimeters on the focal plane is schematically presented in Figure 4.14 and a photo of the integrated focal plane is reported in the upper panel of Figure 4.15.

4.2.6.1 System level test campaign

The integration of the focal plane has began in April 2019 at the CNR of Bologna and will proceed with the system level tests, that are foreseen to last until Summer 2020. The campaign covers many activities, starting from the integration of the focal plane, followed by the functional verification of the polarimeters, of the electronics and of the acquisition software, then proceeding to the optimization of the polarimeters T_{noise} and finally to the evaluation of the final performances. A picture of the experimental setup is shown in the bottom panel of Figure 4.15. We underline that, during the unit tests, we chose the LNAs biases to balance the polarimeter, in order to assure the validity of the simple equations 4.15 and make the interpretation of the data more straightforward. During the system level tests, on the contrary, the goal will be to optimize the performance of the polarimeters as much as possible, and the biases will be chosen in order to obtain the lowest possible value of T_{noise}. The system tests will finally end with the shipment of STRIP focal plane to Tenerife. We underline that the purpose of the unit tests was to verify the functionality of the available polarimeters and to get general idea of the properties of each polarimeter. The numbers reported in Table 4.1 are not optimized and they are not the final ones, as they will be overwritten by the system level tests results.

	T_{noise} [K]	$\Delta\nu$ [GHz]	f_0 [GHz]	$\Delta Q/U_{\mathrm{rms}}$ [mK $\times \sqrt{s}$]	f_{knee} [mHz]	α
STRIP01	–	–	–	–	–	–
STRIP02	$31.5^{+4.7}_{-7.2}$	7.15 ± 0.38	43.36 ± 0.03	1.4 ± 0.8	80.0 ± 10.0	0.5 ± 0.1
STRIP03	–	–	–	–	–	–
STRIP04	$51.9^{+15.9}_{-18.6}$	7.02 ± 0.16	43.38 ± 0.05	1.0 ± 0.1	35.0 ± 5.0	1.0 ± 0.1
STRIP05	$28.1^{+5.9}_{-7.1}$	6.91 ± 0.01	43.35 ± 0.14	0.9 ± 0.4	6.9 ± 0.8	2.0 ± 0.2
STRIP06	–	–	–	–	–	–
STRIP07	$22.7^{+6.3}_{-4.4}$	6.40 ± 0.15	43.16 ± 0.01	0.9 ± 0.3	205.0 ± 105.0	0.8 ± 0.2
STRIP08	$37.0^{+8.8}_{-11.9}$	7.65 ± 0.31	43.57 ± 0.07	–	–	–
STRIP09	$27.7^{+119.9}_{-92.7}$	6.56 ± 0.15	43.25 ± 0.02	0.7 ± 0.3	150.0 ± 50.0	1.3 ± 0.3
STRIP10	$76.9^{+38.2}_{-109.8}$	6.11 ± 0.02	43.19 ± 0.02	1.7 ± 0.9	45.0 ± 5.0	0.6 ± 0.2
STRIP11	–	–	–	–	–	–
STRIP12	$28.2^{+5.7}_{-8.0}$	6.60 ± 0.01	43.15 ± 0.01	0.9 ± 0.2	65.0 ± 5.0	0.5 ± 0.2
STRIP13	$45.8^{+8.6}_{-6.1}$	6.95 ± 0.12	43.59 ± 0.07	1.1 ± 0.3	11.7 ± 2.3	2.3 ± 0.2
STRIP14	–	–	–	–	–	–
STRIP15	$53.1^{+19.3}_{-11.6}$	7.02 ± 0.06	43.41 ± 0.01	–	–	–
STRIP16	$40.8^{+12.7}_{-7.9}$	7.23 ± 0.10	43.61 ± 0.07	–	–	–

STRIP17	$50.1^{+9.8}_{-17.5}$	6.28 ± 0.01	43.27 ± 0.01	1.3 ± 0.5	65.0 ± 5.0	1.0 ± 0.1
STRIP18	–	–	–	–	–	–
STRIP19	–	–	–	–	–	–
STRIP20	–	6.06 ± 0.04	42.90 ± 0.03	–	–	–
STRIP21	$109.7^{+40.8}_{-71.8}$	6.61 ± 0.08	43.41 ± 0.08	6.3 ± 3.2	4.0 ± 1.0	1.0 ± 0.2
STRIP22	$40.6^{+8.3}_{-6.3}$	6.53 ± 0.56	43.15 ± 0.01	–	–	–
STRIP23	–	–	–	–	–	–
STRIP24	$52.1^{+23.1}_{-25.0}$	7.85 ± 0.24	43.59 ± 0.07	–	–	–
STRIP25	–	6.98 ± 0.00	43.41 ± 0.02	–	$(5.3 \pm 0.8) \times 10^3$	0.5 ± 0.1
STRIP26	$107.5^{+75.6}_{-127.8}$	7.36 ± 0.03	43.84 ± 0.04	1.7 ± 1.0	3.0 ± 1.0	1.1 ± 0.1
STRIP27	$55.0^{+19.4}_{-14.9}$	7.15 ± 0.12	43.57 ± 0.06	–	–	–
STRIP28	$36.0^{+13.3}_{-16.1}$	7.17 ± 0.14	43.43 ± 0.01	1.4 ± 0.7	10.5 ± 0.5	1.2 ± 0.3
STRIP29	$36.7^{+11.2}_{-11.1}$	7.16 ± 0.09	43.36 ± 0.08	–	–	–
STRIP30	$36.4^{+8.5}_{-8.9}$	7.38 ± 0.16	43.74 ± 0.18	1.2 ± 0.4	31.0 ± 4.0	0.9 ± 0.1
STRIP31	$42.7^{+14.4}_{-12.0}$	6.63 ± 0.06	43.09 ± 0.01	–	–	–
STRIP32	–	–	–	–	–	–
STRIP33	$23.6^{+5.5}_{-4.2}$	6.17 ± 0.10	42.88 ± 0.02	0.8 ± 0.2	40.0 ± 18.0	1.1 ± 0.4
STRIP34	$29.6^{+15.6}_{-65.2}$	6.03 ± 0.02	42.90 ± 0.03	0.9 ± 0.2	19.0 ± 1.0	1.1 ± 0.2
STRIP35	$40.2^{+16.0}_{-17.2}$	6.50 ± 0.01	43.27 ± 0.05	1.2 ± 0.5	80.0 ± 0.1	0.8 ± 0.1
STRIP36	$51.1^{+16.4}_{-29.8}$	6.60 ± 0.02	43.19 ± 0.07	1.1 ± 0.3	350.0 ± 50.0	0.6 ± 0.1
STRIP37	$33.2^{+6.8}_{-8.7}$	6.63 ± 0.09	43.40 ± 0.10	1.0 ± 0.4	65.5 ± 54.5	1.4 ± 0.1
STRIP38	–	–	–	–	–	–
STRIP39	$29.4^{+6.6}_{-8.6}$	6.03 ± 0.16	43.11 ± 0.05	0.9 ± 0.2	14.5 ± 1.5	1.5 ± 0.3
STRIP40	$28.1^{+6.2}_{-5.7}$	6.83 ± 0.01	43.40 ± 0.02	0.9 ± 0.4	4.2 ± 0.5	1.5 ± 0.2
STRIP41	$39.5^{+13.0}_{-21.4}$	7.08 ± 0.05	43.59 ± 0.04	–	–	–
STRIP42	–	–	–	–	–	–
STRIP43	$31.0^{+7.7}_{-10.7}$	6.75 ± 0.10	43.18 ± 0.02	0.7 ± 0.4	15.0 ± 5.0	2.2 ± 0.1
STRIP44	$178.1^{+154.4}_{-3371.0}$	6.32 ± 0.19	43.39 ± 0.11	2.2 ± 1.6	325.0 ± 275.0	0.4 ± 0.1
STRIP45	$30.8^{+8.1}_{-4.1}$	6.41 ± 0.06	43.24 ± 0.05	0.8 ± 0.3	22.5 ± 5.5	2.0 ± 0.2
STRIP46	$31.1^{+7.6}_{-4.7}$	6.33 ± 0.05	43.12 ± 0.05	0.9 ± 0.2	5.5 ± 1.5	1.1 ± 0.3
STRIP47	$41.5^{+11.4}_{-17.7}$	6.38 ± 0.20	43.09 ± 0.07	–	–	–
STRIP48	$68.8^{+18.4}_{-57.3}$	6.77 ± 0.18	43.22 ± 0.01	–	–	–
STRIP49	–	–	–	–	–	–
STRIP50	$35.6^{+4.3}_{-1609.2}$	6.20 ± 0.04	43.20 ± 0.02	–	–	–
STRIP51	$27.3^{+7.9}_{-4.5}$	6.34 ± 0.03	43.01 ± 0.01	0.9 ± 0.3	7.0 ± 3.0	1.1 ± 0.2
STRIP52	$31.9^{+5.9}_{-6.2}$	7.40 ± 1.25	43.48 ± 0.26	0.8 ± 0.2	240.0 ± 170.0	0.6 ± 0.2
STRIP53	–	–	–	–	–	–
STRIP54	$50.8^{+21.3}_{-15.9}$	8.18 ± 0.06	43.29 ± 0.05	1.0 ± 0.3	160.0 ± 70.0	1.5 ± 0.1
STRIP55	$29.5^{+2.1}_{-13.1}$	8.20 ± 0.04	43.64 ± 0.04	–	–	–
STRIP56	$40.7^{+12.6}_{-18.3}$	8.14 ± 0.02	43.39 ± 0.05	1.0 ± 0.4	70.0 ± 20.0	1.1 ± 0.7
STRIP57	$31.3^{+8.5}_{-20.7}$	8.83 ± 0.09	43.67 ± 0.05	0.9 ± 0.2	75.0 ± 15.0	0.9 ± 0.3
STRIP58	$24.3^{+6.1}_{-4.4}$	8.48 ± 0.40	43.37 ± 0.02	0.6 ± 0.2	75.0 ± 55.0	1.3 ± 0.1
STRIP59	$29.1^{+6.8}_{-5.6}$	8.29 ± 0.12	43.73 ± 0.04	0.7 ± 0.1	110.0 ± 60.0	0.6 ± 0.2
STRIP60	–	–	–	–	–	–
STRIP61	$21.2^{+5.4}_{-4.1}$	8.16 ± 0.24	43.25 ± 0.01	0.7 ± 0.2	805.0 ± 95.0	1.3 ± 0.1
STRIP62	$58.1^{+23.7}_{-35.6}$	8.60 ± 0.19	43.66 ± 0.03	1.0 ± 0.2	170.0 ± 130.0	0.6 ± 0.1
STRIP63	$26.8^{+6.5}_{-4.9}$	8.20 ± 0.07	43.15 ± 0.03	0.7 ± 0.2	70.0 ± 20.0	1.2 ± 0.1
STRIP64	$33.6^{+9.8}_{-5.5}$	8.25 ± 0.52	43.35 ± 0.11	1.1 ± 0.5	$(1.1 \pm 0.2) \times 10^3$	0.7 ± 0.1
STRIP65	$32.9^{+7.2}_{-4.5}$	6.33 ± 0.12	43.42 ± 0.03	0.8 ± 0.3	125.5 ± 12.5	1.6 ± 0.1
STRIP66	$29.3^{+6.9}_{-33.1}$	7.71 ± 0.23	43.48 ± 0.06	0.7 ± 0.2	350.0 ± 250.0	0.5 ± 0.3
STRIP67	$27.9^{+7.9}_{-54.6}$	8.74 ± 0.01	43.47 ± 0.03	0.7 ± 0.2	16.0 ± 0.1	1.7 ± 0.4
STRIP68	$31.6^{+8.1}_{-6.2}$	7.79 ± 0.03	43.03 ± 0.03	1.2 ± 0.5	$(5.5 \pm 0.2) \times 10^3$	0.4 ± 0.1
STRIP69	$37.2^{+7.5}_{-4.7}$	8.29 ± 0.31	43.64 ± 0.01	2.1 ± 1.1	100.0 ± 0.1	0.5 ± 0.1
STRIP70	$41.3^{+7.0}_{-5.6}$	8.40 ± 0.05	43.35 ± 0.01	0.9 ± 0.2	17.5 ± 7.5	1.3 ± 0.2
STRIP71	$68.1^{+22.8}_{-20.1}$	9.01 ± 0.27	95.19 ± 0.22	1.8 ± 0.9	$(2.0 \pm 1.9) \times 10^3$	1.1 ± 0.6
STRIP72	$91.7^{+32.6}_{-30.5}$	7.68 ± 0.65	96.23 ± 0.16	1.7 ± 0.6	25.0 ± 8.0	1.9 ± 0.6
STRIP73	$114.6^{+27.5}_{-20.5}$	10.34 ± 1.42	98.75 ± 0.57	1.6 ± 0.7	$(1.5 \pm 1.2) \times 10^3$	1.0 ± 0.1

STRIP74	$108.4^{+64.7}_{-25.4}$	4.01 ± 0.36	95.61 ± 0.34	2.2 ± 1.3	$(5.5 \pm 2.5) \times 10^3$	1.0 ± 0.1
STRIP75	$80.2^{+38.6}_{-17.2}$	5.39 ± 0.03	95.71 ± 0.23	1.2 ± 0.4	$(1.6 \pm 0.1) \times 10^3$	1.1 ± 0.1
STRIP76	$105.9^{+18.1}_{-14.2}$	6.56 ± 0.54	97.47 ± 0.11	7.7 ± 7.5	26.5 ± 19.5	0.9 ± 0.3
STRIP77	$299.2^{+4815.2}_{-648.1}$	8.27 ± 0.42	98.56 ± 0.13	6.1 ± 3.5	0.8 ± 0.2	1.6 ± 0.3
STRIP78	$102.5^{+6795.4}_{-38.2}$	7.41 ± 0.74	98.67 ± 0.01	1.0 ± 0.2	67.5 ± 1.5	3.6 ± 0.2
STRIP79	–	–	–	–	–	–
STRIP80	–	–	–	–	–	–
STRIP81	$108.4^{+61.1}_{-34.4}$	8.64 ± 0.57	99.76 ± 0.40	1.7 ± 1.1	15.5 ± 4.5	1.2 ± 0.2
STRIP82	$183.2^{+252.1}_{-55.1}$	6.10 ± 0.40	97.33 ± 0.10	3.3 ± 1.6	19.5 ± 3.5	1.2 ± 0.1
STRIP83	–	–	–	–	–	–
STRIP84	–	–	–	–	–	–
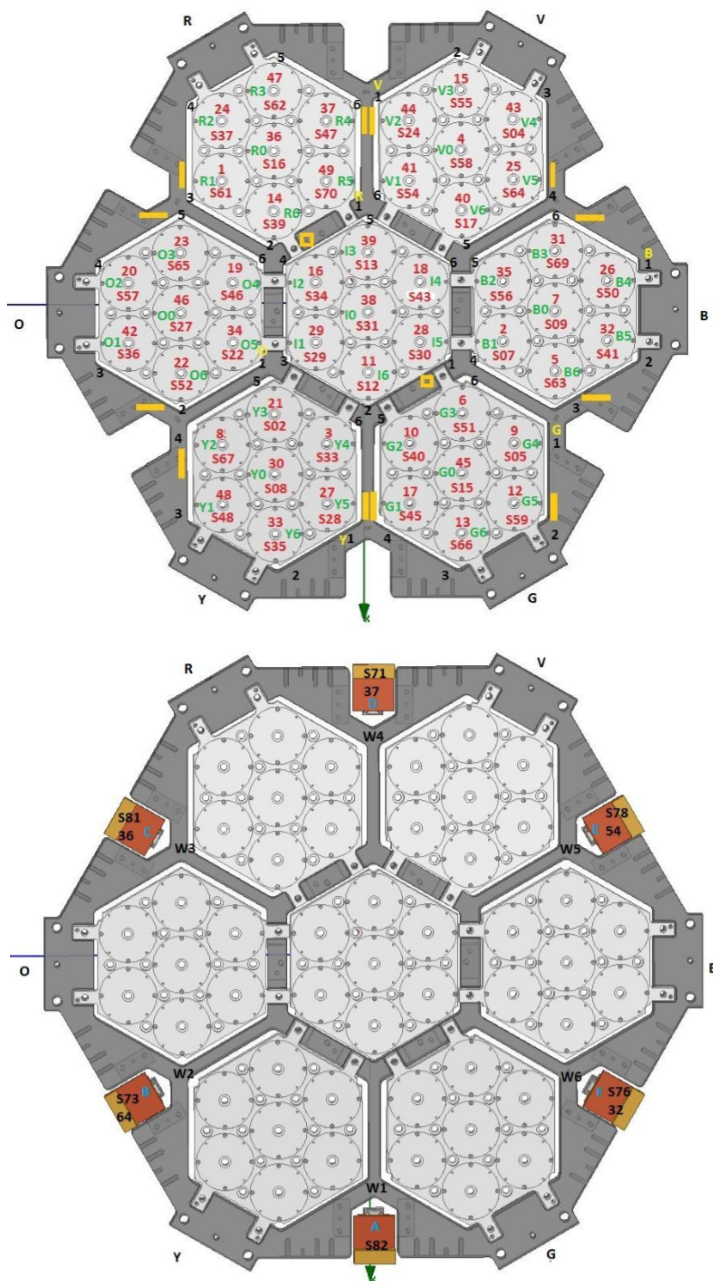
Figure 4.14: Final disposition of the STRIP polarimeters on the focal plane. The *top* panel shows the disposition of the Q-band polarimenters while the *bottom* panel shows the disposition of the W-band polarimeters. Each polarimeter is identified with the letter "S" followed by its identification number (e.g. "S37" stands for "STRIP 37").
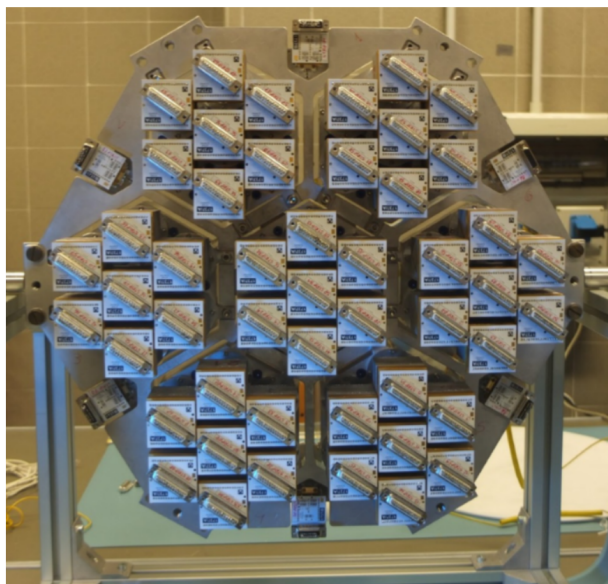
Figure 4.15: *Top*: photo of the integrated STRIP focal plane. *Bottom*: photo of the system level test setup at the CNR of Bologna.

Chapter 5

A simulation pipeline for STRIP

5.1 Data analysis in CMB experiments

Most people think that a telescope taking an image of the sky works much like a normal camera: the instrument is pointed to an object, an optical system focuses the light on an array of detectors and, after exposing them for a short while, a "picture" of the object is taken. This idea is quite close to reality if we talk of optical telescopes, but when going to lower frequencies, this mode of operation becomes impractical: the size of detectors scales in proportion to the wavelength of the radiation to measure, reducing the number of pixels that can be put in the focal plane. For CMB experiments, in fact, the typical number of detectors goes from tens to tens of thousands, compared to hundreds of millions for optical telescopes. To overcome this limitation, microwave and radio telescopes, *scan the sky* using their detectors as a paintbrush, moving the boresight across the sky and doing many individual observations of small areas of the sky to build up a larger image.

The direct output of a CMB telescope is not a single value per sky pixel, but instead a time series of values (the sky temperatures) for each detector, called the **time-ordered-data (TOD)**.

Knowing the TOD and the details of the telescope's scanning pattern, it is possible to reconstruct an image of the sky in a process called "map-making". The recontructed map is actually an intermediate stage in information processing between the data acquisition by the instruments, very large

time-ordered-data streams, and the ultimate stage of cosmological analysis, typically estimating a set of physical parameters of interest. The main steps of a typical data analysis pipeline for a CMB experiment are shorty described in the following. The general idea is to compress the raw data by many orders of magnitude (from the TOD to the map, to the power spectrum and finally to the cosmological parameters), while preserving the relevant cosmological information.
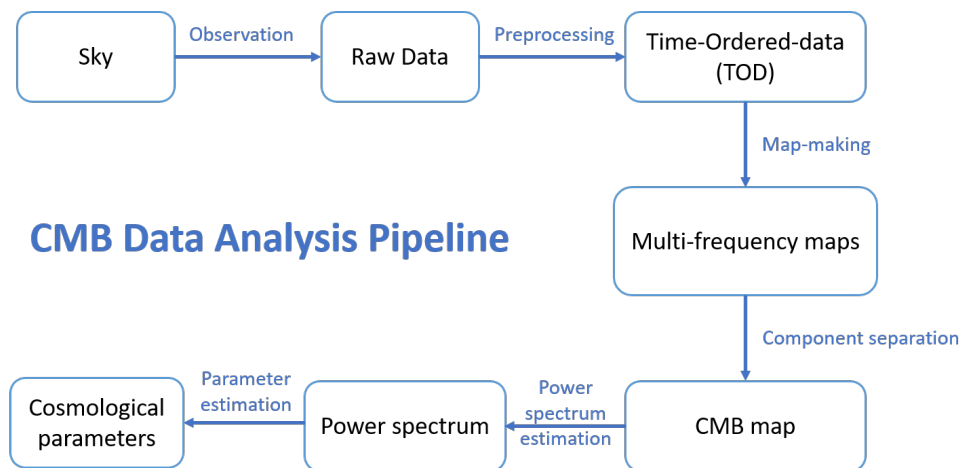
Figure 5.1: Typical data analysis pipeline for a CMB experiment

5.1.1 From raw data to TOD

As a first step, raw data measured by the telescope are cleaned and calibrated. Data taken during bad weather conditions, or with too much sunlight, or during any other instrument mulfunction are "flagged" and, in turn, excluded from the analysis. The cleaned data are then calibrated, which means that they are converted from instrumental units (i.e. voltages) to physical units (i.e. temperatures). Calibration constants are obtained from well known bright sources. The result of processing the raw data is the time-ordered-data, that is to say the list of the measured temperatures of all the sky pixels observed, in chronological order.

5.1.2 Map Making

TODs are usually huge sequences made of billions of samples and thus very difficult to analize. Knowing the time sequence of pointings, it is possible to compress the cosmological information from the TOD to a much smaller data set, the map. The output map contains typically $10^5 \div 10^7$

pixels, which means that map-making can be seen as a data-reduction analysis which decrease the volume of data by three orders of magnitude and more. The results of the map-making process are the sky maps, one for each frequency channel of the instrument under consideration. The best map-making method should retain all the cosmological information from the TOD, so that the cosmological parameters can be measured just as accurately from the map as from the full TOD. A detailed description of the map-making problem and of the most used approaches will be provided in Section 5.2.

5.1.3 Component separation

The sky map produced by an instrument usually contains contribution not only from the CMB, but also from the Galactic foregrounds we have seen in Section 2.1. To remove the foreground contamination in the CMB data, one can use prior information of the foreground signals to reduce their impact on the data. The idea behind *component separation* is the fact that CMB and foreground emissions have different frequency dependencies and are expected to be uncorrelated. The CMB, in fact, has a black body spectrum, while the foregrounds have their own frequency behaviour, as presented in Section 2.1 (power law for synchrotron emission and modified black body radiation for thermal dust emission). For this reason, multi-frequency observations of the same sky area are essential to isolate the CMB signal. The typical output of a CMB experiments are in fact several maps, each one at a different frequency and with a different "dominant" component (synchrotron at low frequencies, dust at high frequencies and CMB at intermediate frequencies[1]).

There are mainly two approaches to perform the component separation (Krachmalnicoff, 2015). One is *template fitting*. In this case, one makes assumptions on the characteristics of the different emissions, parametrizing their frequency spectra. We can write the observed map m_ν at frequency ν in the form:

$$m_\nu = As_\nu + n_\nu \qquad (5.1)$$

where s_ν is the vector containing the unknown values of the Stokes parameters I, Q, U (if the instrument is sensitive to polarization) for CMB and each foreground component and n_ν is the instrumental noise. A is the "mixing matrix", parametrized by a set of unknown parameters (e.g. spectral indices and amplitude of the various astrophysical components), which varies from

---

[1]Actually, as we have seen in Section 2.1, in case of polarization there is not a frequency range in which the CMB is dominant over foregrounds. Generally, one choose a frequency in the range where the foregrounds are minimized (from ~ 70 to $\sim 140\,\mathrm{GHz}$)

pixel to pixel on the maps. The values of the parameters are then extracted with a standard Maximum Likelihood fit on the multy-frequency observations. In this way, maps of different foreground emissions are recovered and then removed by the measured sky maps, to isolate the CMB signal.

Another approach is the *minumum variance* method. In this case, the only assumption which is made concerns the spectral behaviour of the CMB, and no other prior on the foregrounds is considered. With a multi-frequency set of sky maps, the CMB signal is retrieved by performing a linear combination of them:

$$s_{\text{CMB}} = \sum_{\nu} w_{\nu} m_{\nu}, \tag{5.2}$$

where the w_{ν} are the weights assigned to each frequency map m_{ν}. Imposing the condition of a blackbody spectrum for the CMB radiation implies $\sum_{\nu} w_{\nu} = 1$. The weights are then obtained by minimizing the variance of s_{CMB}.

5.1.4   Power spectrum estimation

Once we have the CMB map, we can proceed to the power spectrum estimation. As discussed in Section 1.3.1, if the statistical properties of the CMB fluctuations are isotropic and Gaussian, all the cosmological information in a sky map is contained in its power spectrum. This means that all the information from a data set can be reduced to just a few thousand numbers. An important thing to remind is that the power spectrum is estimated from the sky map, which is a stochastic realization of the underlying true power spectrum. This means that even if we had a perfect experiment (i.e., with zero instrumental noise) we would not be able to recover a perfect power spectrum, but we would still be limited to an accuracy within the cosmic variance limit.

A straightforward expansion of the map in spherical harmonics is often complicated in real-life experiments, mostly for two reasons (Paykari and Starck, 2012):

1. the entire sky may not be available for the observation, due to the partial sky coverage of the scanning, the removing of bad data or the cut of the galactic plane region.

2. one wishes to give less weight to noisier pixels in order not to spoil cosmological information. The pixels are therefore weighted by a *window function*, that states the relative weight of each pixel.

Both of these facts spoil the orthogonality of the spherical harmonics, and a correlation between the l modes is introduced.

Several methods have been developed in order to extract the power spectrum from data. Some of them relies on the evaluation of the likelihood function $P(m|C_l)$, that is the probability to get a certain observed map, given a theory where C_l is the underlying CMB power spectrum. The likelihood evaluation is not computationally feasible at the full map resolution and hence different methods are used at low and high resolutions. Low-l codes (e.g. MANDCAP, Commander) use low resolution maps (if HEALPix maps, $N_{\text{side}} = 8, 16$) and determine the properties of the likelihood directly in the pixel space using Bayesian statistics. High-l codes, instead, work in the harmonic space.

Some codes, like MASTER and Polspice, actually don't go through the likelihood computation; instead, they directly perform a spherical harmonic transform of the CMB map. They are called "pseudo-C_l" algorithms, and they are able to provide an unbiased estimate $\hat{C}_l$ of the true spectrum C_l, which means that $\left\langle \hat{C}_l \right\rangle = C_l$. They are usually preferred to maximum likelihood techniques at high l (at low l they show a higher variance) because they are pretty quick and light from a computational point of view. The unwanted contribution of the instrumental noise, any necessary alteration of the sky map (introduced during the data analysis) can be calibrated in Monte Carlo (MC) simulations of the modeled observation and can then be removed or corrected for in the estimated power spectrum. The harmonic coupling induced by the incomplete sky coverage, can be analytically corrected to obtain an unbiased estimated power spectrum.

Polspice[2], in particular, has been a widely used software to estimate angular power spectra in the analysis presented in this thesis. Its peculiarity with respect to other methods is that, to estimate the spectrum, it exploits the 2 point angular correlation function $\xi(\theta)$ of the signal at a distance θ:

$$\xi(\theta) = \sum_l \frac{2l+1}{4\pi} C_l P_l(\theta), \tag{5.3}$$

where P_l is the Legendre polynomial.

Polspice is able to correct for the effects introduced by the partial sky and can deal with inhomogeneous weights given to the pixels of the map. It can also deal with polarized data, returns an un-biased estimator of the auto- and cross-power spectra $C(l)$ for T, E and B (given I, Q and U maps).

---

[2]`www2.iap.fr/users/hivon/software/PolSpice/`

5.1.5   Cosmological parameters estimation

The power spectrum computed from the data can be used to constrain cosmological models, as it depends on virtually all cosmological parameters. The most common method for estimating the cosmological parameters is based on a Markov Chain Monte Carlo. It is an iterative procedure, where, at each step, a sample of parameters θ in the parameters space is chosen, the likelihood $P(C_l|\theta)$ is computed and depending on the criterion is acceped of rejected. The chain stops when the convergence criterion is satisfied and the last set θ is taken as the measured cosmological parameters.

5.2   The map-making problem: the destriping technique

Map-making is the process of making a sky map out of a time-ordered-data stream. It is a difficult step of the data analysis pipeline, as it should compress all the information contained in a TOD of tens of billions of samples in a single map, while preserving the cosmological information. Moreover, it is a very crucial step for noise reduction. As mentioned before, to detect the faint CMB anisotropies signal (B-modes, in particular), a tight control of experimental systematics is required. One of these systematics is generated by instrumental long term noise drifts that are characterized by a *1/f* power spectrum and results in correlated noise in the time-streams (see Section 2.2.1). The best place to remove correlated noise and time-varying systematic errors is in the map-making step.

To preserve the cosmological information, the resulting map must have well-understood statistical properties, which in turn means that one needs to understand the properties of the TOD. As a consequence, to produce a map with a scanning telescope, one must first build an accurate model of how the telescope transforms the signal from sky to TOD, and then invert this model to reconstruct the sky from the TOD.

Forgetting noise for a moment, the most general possibile response function that gives a TOD from an "input" sky m is:

$$y(t) = f(t, m(t)), \tag{5.4}$$

where the TOD $y(t)$ can be the total intensity I or one of the Stokes parameters Q and U. In practice, one has to make few simplifying assumptions.

- Discrete TOD: the telescope does not provide a continuous time-stream, but a set of samples, acquired at the sampling frequency f_{samp} of the instrument.

- Discrete sky: the sky is modeled as a set of discrete pixels. In the field of CMB, the most used pixelation is the one provided by HEALPix

(Górski et al., 2005), in which the sky sphere is hierarchically tessellated into curvilinear quadrilaterals distributed on lines of constant latitude and covering equal areas. The resolution of the grid is expressed by the parameter N_{side}[3], which is related to the number of pixels as: $N_{\text{pix}} = 12 \times N_{\text{side}}^2$. Pixelation is supported down to a pixel size of 0.4 mas (milli-arcseconds), corresponding to potentially 3.5×10^{18} pixels on the sphere. Pixelization is a more and more strong approximation of the real sky as the resolution of the grid decreases, as it assumes that the signal in each pixel is constant. HEALPix also provides a mathematical structure supporting a suitable discretization of functions on a sphere, permitting a fast and accurate statistical analysis of CMB data.

- Constant sky: we assume that the sky does not change during our observation time: $m(t) \equiv m$. One should therefore mask the pixels containing variable sources, excluding them from the analysis.

- Linear response: we assume that the TOD is a linear function of the sky signal.

These assumptions allow us to write Equation 5.4 as a matrix multiplication:

$$y(t) = Pm \tag{5.5}$$

where m is the pixelized input sky map and P is the so-called *pointing matrix*, a rectangular matrix of size $M \times N$, where N is the number of elements in the TOD and M is the number of pixels in the map. The pointing matrix P for a temperature measurement is a matrix of ones and zeros: the value of the element P_{ip} is 1 if the i-th sample in the TOD has been measured while the telescope was pointing towards pixel p, otherwise it's zero. For polarization-sensitive experiments, the pointing matrix is in general more complex and contains terms $\sin \psi_t$ and $\cos \psi_t$ in order to reconstruct the values of Stokes Q and U from the total signal. ψ_t is the orientation of polarization sensitivity, dependent on the momentary orientation of the telescope and on each detector's orientation on the focal plane. For STRIP case, the situation is actually simpler. Since the polarimeters measures Q and U directly, polarization outputs are fully decoupled and map-making can be therefore performed independently on the two polarization outputs. The pointing matrix is therefore a matrix of ones and zeros, similarly to the temperature case.

---

[3]N_{side} defines the number of divisions along the side of the base-resolution pixel that is needed to reach a desired high-resolution partition
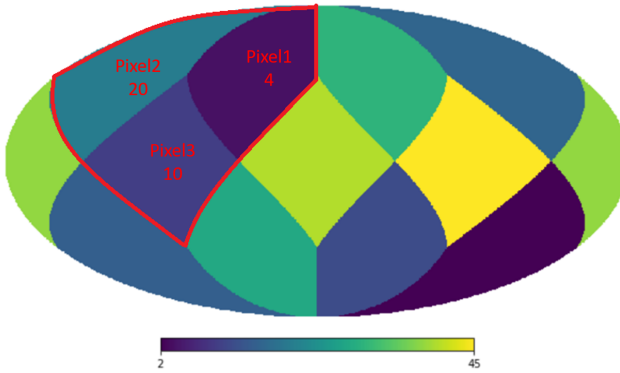
Figure 5.2: HEALPix map with $N_{\text{side}} = 1$ (12 pixels). In the simple example
described in the text, just the three pixels encircled by the red line are
considered.

For sake of clarity, we provide a minimal example. We consider an
experiment observing just three pixels of the sky map in Figure 5.2, so that
the input map is given by:

$$m = (4, 20, 10) \tag{5.6}$$

each element position represents the pixel number, while the value is the
temperature of the sky in that pixel. We assume a TOD of $N = 9$ samples,
with the following pointing matrix:

$$P = \begin{pmatrix} 1 & 0 & 0 \\ 1 & 0 & 0 \\ 0 & 1 & 0 \\ 1 & 0 & 0 \\ 0 & 1 & 0 \\ 0 & 0 & 1 \\ 0 & 0 & 1 \\ 1 & 0 & 0 \\ 0 & 0 & 1 \end{pmatrix}. \tag{5.7}$$

The resulting TOD is thus:

$$y = Pm = (4, 4, 20, 4, 20, 10, 10, 4, 10) \tag{5.8}$$

Without any kind of noise, we could in principle pass on each pixel of the
map just once, as the temperature observed would remain the same. What
happens if we consider noise contribution? If there is white noise w only,

things remain quite simple, since, under the assumptions of Gaussianity and stationarity, its expectation value is $\langle w \rangle = 0$. This means that, if we make enough measurements of each pixel we could just take arithmetic mean of the measurements made on each pixel. This produces a so-called "binned map".

However, in general, noise has also a correlated component, which definitely complicates the map-making process. Let's rewrite the TOD considering also the noise vector n:

$$y(t) = Pm + n. \tag{5.9}$$

There mainly three approaches to map-making for CMB experiments. The maximum-likelihood method (M-L) (Doré et al. (2001), Stompor et al. (2001), and de Gasperis et al. (2005)), TOD filtering (Hivon et al. (2001) and Poletti et al. (2017)) and destriping (Delabrouille (1998), Maino et al. (1999), Revenu et al. (1999), and Maino et al. (2002)).

Given the data model 5.9, the maximum-likelihood solution to the map making problem is:

$$m = (P^T C_n^{-1} P)^{-1} P^T C_n^{-1} y, \tag{5.10}$$

where C_n is the noise covariance matrix $C_n \equiv \langle nn^T \rangle$. Usually, M-L map-making assumes the noise to be stationary, meaning that its statistical properties do not change over the mission life time. This can be formally expressed by stating that the correlation between two samples depends only from their temporal distance, that is:

$$C_n^{ij} = f(|i - j|) \tag{5.11}$$

It is further assumed that the elements of the covariance matrix vanish when $|i - j|$ is larger than some threshold. This means that the noise correlation is significant only across a number of samples that is a tiny fraction of the total length of the TOD. With these approximations, the noise covariance matrix (and its inverse C_n^{-1} too) is band diagonal and well approximated by a circulant matrix, which can be written in a more compact form in Fourier space (Natoli et al., 2001). The M-L algorithms solve this equation exactly, producing optimal maps in the sense that the noise in the map is minimised without the loss of information (i.e. the sky signal in the maps is not distorted). However, M-L algorithms are extremely heavy from a computational point of view as they solve for the entire noise TOD, that can be of billions of samples.

As future data-sets become very large, the M-L algorithm becomes increasingly difficult to run. Applying the method to massively multi-detector experiments would require massive and expensive computing

platforms and very long computation times. Moreover, the last stages of
the CMB data analysis pipeline (i.e. the power spectrum estimation) often
require information on the noise power and correlation properties and the
propagation of systematic effects in the map, and this is effectively done
by running hundreds of Monte Carlo simulations through the map-making
pipeline (Sutton et al., 2009). The M-L algorithm is not suited for this
tasks, creating the need for faster methods that can be used on medium-
sized cumputing platforms over and over again, to simulate and remove
experimental systematics with enough precision to search for the small
B-modes signal in the CMB polarisation field.

An alternative method for map-making is to apply a high-pass filter
to the TOD, removing the correlated *1/f* part of the noise. The noise part
of the filtered TOD is uncorrelated, so the map can be obtained from a
simple binning. This method is very fast and well suited to Monte Carlo
simulations, but it can critically distort the signal part of the TOD. There are
methods to mitigate this effect, but, nevertheless, filtering introduces extra
variance into the power spectrum estimate, especially at low-l where the
B-modes signal is expected (Poletti et al., 2017).

The destriping method is being developed as a "third" way to CMB
map-making. The name "destriping" is due to the fact that correlated noise
usually generates stripes on the sky map, as we can see in Figure 5.3 for
the Planck satellite case. The stripes pattern depends on the details of the
scanning strategy. Unlike M-L algorithms, it does not solve the map-making
equation 5.10 in an exact way but it model the correlated part of the noise
as a sequence of baselines of length l_{base}. Destriping is much faster than
the M-L map making as it has much less variables to solve for (the array
of baselines can be orders of magnitude shorter than the TOD) and it is
therefore suitable for multiple Monte-Carlo applications. The algorithm is
tunable, i.e. the baseline length l_{base} can be varied and set to a value that
assures the best performances. The destriping performance also depends
on the distribution of the *crossing points*, i.e. the observations falling on
the same map pixels at different times. This property depends on the scan
angle, the beam position on the telescope field of view and the selected
scanning strategy.

The destriping technique has been proven to be very successful for a
number of scanning strategies; in particular, for the Planck case, destriped
maps were negligibly different in comparison to ones obtained with M-
L algoriths, but computed in a fraction of time (Poutanen et al., 2006).
Given its appealing characteristics, we chose to implement a destriper to
perform map-making in the simulation pipeline of STRIP and we tested
its performance in the STRIP experiment case (see Section 5.3). The next
Section presents the mathematical treatment for the destriping technique

before destriping

−1.4 ▬▬ 1.4 mK
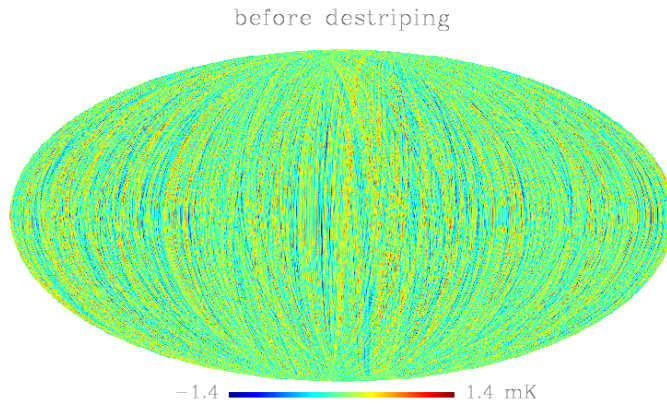
Figure 5.3: Map of white and *1/f* noise before destriping for the Planck experiment
case. Picture from Donzelli et al. (2009)

and a strategy for its implementation.

5.2.1 The destriping technique

The destriping technique is based on two assumptions:

1. the noise term is the sum of two independent components: a correlated
   component and a white noise component,

2. the correlated part is modeled as a sequence of constant values as
   depicted in Figure 5.4. In practice, we divide the TOD into n_{base}
   segments of equal length l_{base}; and for each segment we define an
   offset called *baselines*. The baselines model the *1/f* noise, that is the
   low-frequency correlated component. We approximate the rest of the
   noise as white.

Thus, our noise model in Equation 5.9 becomes:

$$n = Fa + w, \tag{5.12}$$

where he vector a (of length n_b) contains the baseline amplitudes. The matrix
F, of size ($n_{\text{TOD}}, n_{\text{base}}$), operates in the baselines space, fixing dimensions
while spreading the baseline vector into a TOD. Each column of F contains
l_{base} elements of 1 corresponding to the baseline in question, and the rest are
0. Let's go back to our simple example and consider a vector of 3 baselines
of equal length $l_{\text{base}} = 3$:

$$a = (1, -2, 1) \tag{5.13}$$
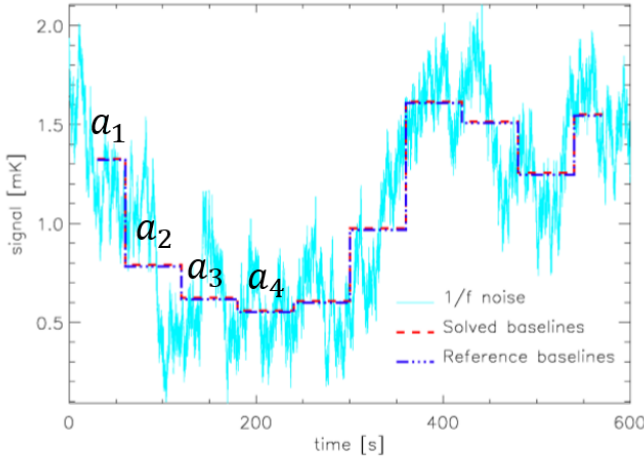
Figure 5.4: Example of a TOD of pure noise. In the destriping approach, the low-frequency modulations are modeled with a series of steps a, called *baselines*. The rest of the noise is considered as white noise. Figure from Kurki-Suonio et al., 2009.

the F matrix in our case would be:

$$
F = \begin{pmatrix}
1 & 0 & 0 \\
1 & 0 & 0 \\
1 & 0 & 0 \\
0 & 1 & 0 \\
0 & 1 & 0 \\
0 & 1 & 0 \\
0 & 0 & 1 \\
0 & 0 & 1 \\
0 & 0 & 1
\end{pmatrix}, \tag{5.14}
$$

and so the correlated noise vector $n_{\text{corr}} \equiv Fa$ would be:

$$
n_{\text{corr}} = (1, 1, 1, -2, -2, -2, 1, 1, 1), \tag{5.15}
$$

and the TOD y would become:

$$
y = (5, 5, 21, 2, 18, 8, 11, 5, 11). \tag{5.16}
$$

The vector w (of length equal to the TOD length, n_{TOD}) represents white noise, and it is assumed to be the result of a Gaussian random process, where the samples in w at different times are uncorrelated:

$$
\langle w_t w_{t'} \rangle = \sigma_t^2 \delta_{tt'} \tag{5.17}
$$

The white noise covariance matrix,

$$C_w = \langle ww^T \rangle = \begin{pmatrix} \sigma_t^2 & 0 & \cdots \\ 0 & \sigma_t^2 & \cdots \\ \vdots & \vdots & \ddots, \end{pmatrix} \qquad (5.18)$$

is thus diagonal, but not necessarily uniform as the white noise variance could in principle vary from sample to sample: the TOD can be a sequence of data streams acquired by different detectors (with differente noise temperatures) or there can be variations in the T_{sys} due to atmosphere temperature T_{atm} modulations, and so on.

Summarizing, the TOD is modeled by:

$$y = Pm + Fa + w \qquad (5.19)$$

where y are the measurements, P is known if we know the scanning strategy, and F is known once we have decided how to model $1/f$ (by fixing n_{base}). We assume also to know the noise variance C_w. We have thus two unknown quantities, the map m and the baselines vector a.

Given the input map m and the baseline amplitudes a, the likelihood of the data y is given by the white noise distribution (Keihanen and al., 2005):

$$P(y|m, a) = (\det 2\pi C_w)^{-1/2} \exp\left(-\frac{1}{2} w^T C_w^{-1}\right), \qquad (5.20)$$

where $w = y - Fa - Pm$. Maximizing the likelihood is equivalent to minimizing the logarithm of its inverse. We obtain the χ^2-minimization function:

$$\chi^2 = -2 \ln P = (y - Fa - Pm)^T C_w^{-1} (y - Fa - Pm), \qquad (5.21)$$

which we want to minimize with respect to both a and m.

Minimization with respect to m gives the maximum-likelihood map

$$\boxed{m = M^{-1} P^T C_w^{-1} (y - Fa)} \qquad (5.22)$$

for a given set of baselines amplitude a, where we have defined

$$M \equiv P^T C_w^{-1} P \qquad (5.23)$$

Subsituting Equation 5.22 back into Equation 5.21, we get the χ^2-function into the form:

$$\chi^2 = (y - Fa)^T Z^T C_w^{-1} Z (y - Fa), \qquad (5.24)$$

where we have defined:

$$Z \equiv I - PM^{-1}P^T C_w^{-1} \tag{5.25}$$

and I is the unit matrix. The matrix Z operates in the TOD space and is a projection matrix $Z^2 = Z$. Since $C_w^{-1}Z$ is symmetric, we can write:

$$C_w^{-1}Z = Z^T C_w^{-1} = Z^T C_w^{-1}Z. \tag{5.26}$$

Minimizing it with respect to a, we obtain the maximum likelihood estimate of the baseline amplitudes by solving the equation:

$$\boxed{(F^T C_w^{-1}ZF)a = F^T C_w^{-1}Zy} \tag{5.27}$$

where we have used Equation 5.26.

An important thing to note is that the solution to Equation 5.27 is not unique. We may add an arbitrary constant to a without changing the value of χ^2. This represents the inability to detect a constant offset of the entire noise stream n, because it has the same effect on y as a constant shift in the intensity of the map m (the monopole). This is actually of no concern, as the goal here is to measure the CMB polarization *anysotropy*, not the mean temperature of the CMB. To remove this ambiguity, we require that the sum of baselines is zero. This is equivalent to adding a term $J^T a$ to the left-side of Equation 5.27, where J denotes a matrix with all elements equal to one (Keihanen and al., 2003).

We can write the solution of Equation 5.27 as

$$a_{\text{out}} = A^{-1}F^T C_w^{-1}Zy, \tag{5.28}$$

where $A \equiv F^T C_w^{-1}ZF + J^T$. Finally, using the maximum-likelihood baselines a_{out} in Equation 5.22, we get the *destriped* output map:

$$m_{\text{out}} = M^{-1}P^T C_w^{-1}(y - Fa_{\text{out}}). \tag{5.29}$$

5.2.2 Implementation strategy

The real issue in the map-making process is of computational nature. We cannot really solve equation 5.28 as we cannot explicitly compute matrix A, save it into memory and invert it to get the baselines vector a. This also applies to the other matrices, especially those build up from the pointing matrix P, like Z. In real life experiments, those matrixes are indeed really huge. Let's take for example the pointing matrix P, which, we recall, it is a rectangular matrix $M \times N$, where N is number of elements in the TOD and M is the number of pixels in the map. Consider the LSPE/STRIP case:

the telescope will observe the sky for at least 2 years (35% duty cycle) with 49 detectors and a sampling frequency of 50 Hz, which means a TOD o about 54 billion samples. STRIP angular resolution corresponds roughly to a HEALPix map of $N_{\text{side}} = 128$, which means $M \sim 200\,000$[4]. Considering that each sample is 8 bytes wide, solving explicitly Equations 5.28 and 5.22, storing the matrixes in memory requires Terabytes of memory.

5.2.2.1 The conjugate gradient algorithm

Equation 5.27 is in the form $Ax = b$, where b is known and A is a positive-definite symmetric matrix. Equations of this kind can be solved by using the *conjugate gradient method* (Strikwerda, 2004). The interest of this method lies in the fact that it does not calculate the matrix A^{-1} explicitly, but it computes the products of A with other vectors. It is often implemented as an iterative algorithm, which converges to the solution of Equation 5.27.

We provide a short overview of the conjugated gradient algorithm in the following.

Since A is symmetric and positive-definite, we can define an inner product between two vectors u and v as:

$$\langle u, v \rangle_A \equiv u^T A v \qquad \forall u, v \in \mathbb{R}^n \tag{5.30}$$

Two vectors are conjugate if and only if they are orthogonal with respect to this inner product: $\langle u, v \rangle_A = 0$. The solution x of the linear system $Ax = b$ corresponds to minimum of the quadratic form:

$$Q(x) = \frac{1}{2} x^T A x - x^T b, \tag{5.31}$$

since $\nabla Q(x) = Ax - b$. It is therefore natural to proceed iteratively, starting from an initial solution x_0 and moving along directions $\{p_k\}_k^n$ that minimize the quadratic form. $\{p_k\}_k^n$ is a set of n mutually conjugate vectors (with respect to A), which means that at each step k of the loop, the direction p_k is chosen orthogonal to the previous directions ($\langle p_j, p_k \rangle_A = 0 \quad \forall j = 0, ..., k-1$).

At the k-th step, the solution is thus updated as:

$$x_{k+1} = x_k + \alpha_k p_k \tag{5.32}$$

where α_k is a positive number corresponding to the length of the descendent path. It is possible to demonstrate that the optimal choice for α_k, which

---

[4]For experiments with higher angular resolution, like Planck, the number of pixels can be even higher.

leads to the minimum of $Q(x_{k+1})$ is:

$$\alpha_k = \frac{r_k^T r_k}{p_k^T A p_k} \tag{5.33}$$

where $r_k = b - Ax_k$ is the residual of the system.

To calculate the descending directions p_k we can do:

$$p_{k+1} = r_{k+1} - \beta_k p_k \tag{5.34}$$

with $p_0 = r_0$. The optimal choice for β_k is :

$$\beta_k = \frac{r_{k+1}^T r_{k+1}}{r_k^T r_k} \tag{5.35}$$

The iteration ends at step k if the residual is below a certain threshold, or when the maximum number of iterations (fixed by the user) is reached. Since it is not granted that the sequence of s_k is monotonically decreasing, it is useful to make the code keep the lowest value for the residual and the corresponding a. If the loop ends because the maximum number of iterations has been reached, this is the configuration that will be returned to the caller.

5.2.2.2   Understanding the Map-making matrixes

We have seen that the conjugate gradient method prevents the need of the inversion of matrix A. However, it still involves many matrix-vector multiplications and therefore can be computationally expensive anyway. In order to solve the map-making equations in a computationally-light way, the smart thing to do is to understand what each matrix product mathematically does and implement functions that reproduce that effect, without actually writing the matrixes.

Let us review the different matrixes involved in the map-making problem:

- The transposed matrix P^T applied to a TOD, produce a *sum map*, where each pixel has a value representing a sum over observations that hit that pixel. In our simple example it would be:

$$P^T y = \begin{pmatrix} 1 & 1 & 0 & 1 & 0 & 0 & 0 & 1 & 0 \\ 0 & 0 & 1 & 0 & 1 & 0 & 0 & 0 & 0 \\ 0 & 0 & 0 & 0 & 0 & 1 & 1 & 0 & 1 \end{pmatrix} \cdot y = \begin{pmatrix} 5+5+2+5 \\ 21+18 \\ 8+11+11 \end{pmatrix}$$

- the product $P^T P$ is a square diagonal matrix where each diagonal element at position pp is equal to the numer of times pixel p has been observed. In our example:

$$P^T P = \begin{pmatrix} 4 & 0 & 0 \\ 0 & 2 & 0 \\ 0 & 0 & 3 \end{pmatrix}. \qquad (5.36)$$

- Since P^T produces a sum map and M counts the number of hits per pixel, the matrix $B \equiv M^{-1}P^T C_w^{-1}$ acts on a TOD producing from it a *binned map*, where each pixel is filled with the average of the measurements done looking to that pixel. It is actually a *weighted average*, as each sample is weighted by the inverse white noise variance $1/\sigma^2$. Let us have a look at Equation 5.22: $(y - Fa)$ is the TOD minus the *1/f* noise, that is sky signal plus white noise only. Thus, the maximum likelihood map is the binned map of the TOD, once wiped clean of the correlated noise.

- Matrix $Z = I - PM^{-1}P^T C_w^{-1} = 1 - PB$ operates on the timeline y and subtract the quantity PBy to it. This means that Z bins the TOD into a map, read a TOD out of this map and subtract it from the original TOD. In other words, Zy subtracts the sky TOD and the white noise from the timeline, producing a "*1/f*-noise-only" TOD.

- F^T applied to a TOD sums up the TOD samples of each baseline segment. In our example, this means:

$$F^T y = \begin{pmatrix} 1 & 1 & 1 & 0 & 0 & 0 & 0 & 0 & 0 \\ 0 & 0 & 0 & 1 & 1 & 1 & 0 & 0 & 0 \\ 0 & 0 & 0 & 0 & 0 & 0 & 1 & 1 & 1 \end{pmatrix} \cdot y = \begin{pmatrix} 5 + 5 + 21 \\ 2 + 18 + 8 \\ 11 + 5 + 11 \end{pmatrix}$$

$F^T C_w^{-1}$ also weights each sample by σ_t^{-2}.

- matrix $A \equiv F^T C_w^{-1} Z F$, like F, operates in the baselines space. Its effect on a baseline amplitude vector a is to spread it into a TOD Fa containing just *1/f* baselines, subtract the sky signal and make a noise estimate ZFa from this baseline TOD and finally calculate the weighted sum $F^T C_w^{-1} Z F$ of the noise TOD for each baseline. Thus, what Equation 5.27 is saying is that the best *1/f* noise model is the one that mostly resembles the noise in the data. Once we have an estimate of the baselines a_{out}, we subtract them from the TOD to produce the clean TOD $y - Fa_{\text{out}}$, which is binned to produce the output map.

An important part of my PhD activity has been devoted to the implementation of a destriper for the STRIP instrument. The entire code is available online at https://github.com/lspestrip/Stripeline.jl/blob/master/src/mapmaker.jl.

In particular, I implemented several functions reproducing the effect of the matrix products following the strategy described above:

- a function tod2map that, given the TOD, the time stream of the observed pixel and the resolution of the map, produces a binned map (or a weighted binned map if C_w is passed to the function). This function reproduces the effect of the matrix product By.

- A function baseline2map that, given the array of baselines, spreads it into a TOD and produces a binned map out of this TOD. This function reproduces the effect of the matrix product BFa.

- A function applyz_and_sum, which acts like the matrix product $F^T C_w Z y$: it bins the TOD into a map, produces a TOD out of this map, subtracts it from the original TOD and finally it sums all the samples belonging to the same baseline.

- A function applya which reproduces the effect of Aa: it spreads the baseline vector into a TOD, bins the TOD into a map, and, like the previous function, subtracts it from the original TOD and calculate the sum of the smples for each baseline.

- A function conj_grad which applies the conjugate gradient algorithm[5].

- A function destriped_map which computes the destriped map once having found the solution for the baseline vector, reproducing the product $B(y - Fa)$.

All these functions are called by the function destripe, that, given the TOD, the list of pixels observed and the resolution of the map, performs the destriping on the given data, returning the array of baselines and the destriped map. The only free parameter in the destriping procedure is the length of each baseline segment, l_{base}. The optimal baseline length to choose is $l_{\text{base}} \sim 1/(2 \cdot f_{\text{knee}})$, as derived by Kurki-Suonio et al., 2009. A higher f_{knee} favors shorter baselines, since the stronger *1/f* noise at relatively high frequencies needs to be modeled better. A lower f_{knee} (and hence a lower amount of correlated noise), instead, favors longer baselines, since short baselines would be dominated by white noise, increasing the uncertainty

---

[5]A conjugate gradient function is already provided by Julia libraries, but we decided to implement it from scratch to perform a more efficient parallelization.

on the baselines estimation. For sake of semplicity, all tests and simulations we will see later on have been performed with a fixed l_{base} (i.e. all baseline segments of equal length), but the code is enough generalised to perform the destriping even in the case of baselines with different lenghts.

The destriping technique has been already implemented and studied by several groups (Delabrouille (1998), Maino et al. (2002), Keihanen and al. (2005), Kurki-Suonio et al. (2009), Sutton et al. (2009), and Zonca et al. (2013)), but we decided to implement our own destriper, customized for the STRIP case. Our destriper is simpler than other destripers, as it exploits the fact that STRIP is able to measure Q and U independently. This results, for instance, in a simpler pointing matrix, as already mentioned. Moreover, it is the first time that a destriper is written in Julia, a quite new programming language that combines the compactness of high-level programming languages, like Python and R with the speed of low-level programming languages like C or Fortran. The destriper code has also been fully parallelized using MPI, in order to deal with very large TODs, succesfully tested and validated as it will be described in Section 5.4.

5.3   The STRIP simulation pipeline

Besides the map-maker, I made other relevant contributions to the simulation pipeline of the STRIP instrument, focusing in particular on the generation of the TOD. The full source code of the simulation pipeline is available on GitHub, with the project name **Stripeline** (`https://github.com/lspestrip/Stripeline.jl/`). The various sections of the pipeline are organised in different modules, whose functions can be directly called from an external program: the tod_splitter module efficiently splits the TOD production among different computing units, the scanning module generates the stream of telescope pointing direction, the noise_generation module generates the noise TOD and the map_maker module performs the destriping. Stripeline also includes a Instrument Database, containing a number of parameters relative to each feed horn in the STRIP focal plane (orientation, ellipticity, directivity, polarimeter matched etc.) and the properties of each polarimeter (bandshape, T_{noise}, f_{knee}, *1/f* slope etc.), as measured during the Bicocca unit tests. Modules instrumentdb and DBforsimulation holds several structures and functions to access the data in the database and effectively use them in the simulation. In particular, I personally developed the modules tod_splitter, noise_generation, map_maker and DBforsimulation.

The programming language chosen for the STRIP pipeline is Julia (`https://julialang.org/`). Julia is an new open-source programming language (first stable version Julia 1.0 released on 7 August 2018) that com-

bines the interactivity and syntax of "scripting" languages, such as Python, Matlab and R, with the speed of "compiled" languages such as Fortran and C. Julia is a high-level, high-performance, dynamic programming language. While it is a general purpose language and can be used in any field, it is conceived as a high-performance instrument destinated in particular to the world of numerical analysis and computational science. The most notable aspect of Julia's implementation is its speed, which is often an order of magnitude faster than Python or R, and sometimes even faster than a fully optimized C code. This makes Julia an extremely appealing code for CMB data analysis, that involves a great amount of data to be processed by iterative algorithms in the map-making process (also the other map-makig functions involves several loops). The result is a performing and easy-to-read pipeline, whose main steps are described in the following.

5.3.1   Splitting the TOD

Our pipeline will be applied to a large amount of data: as calculated before, STRIP will produce a TOD of about 54 billion samples for each Stokes paramenter Q and U, made from the concatenation of the TODs of 49 polarimeters. To that we should add the time stream of pointing angles (another 54 billion$\times 3$ samples) and ancillary information like flags used for instance to tag bad events. Storing all these data in memory would require Terabytes of memory. Moreover, just the loading of this long TOD by a single computing unit would require a large amount of time.

It is thus crucial, both for memory and speed reasons, that simulation and data analysis codes are conceived to work on different computing units at the same time. For this purpose we used Message Passing Interface (MPI[6]), a widely used communication protocol to perform parallel computing, to split the generation of the simulated TOD (or the loading, when we will have real data) among a number of computing units, so that each unit will generate only a subset of the whole data. In this way, a large problem is divided into smaller ones, which can then be solved at the same time.

Of course not every way of splitting is equivalent in terms of performance: one can split the TOD production among the available computing processes in many ways, more or less efficient. Consider for instance a 10 samples TOD, build up from the TODs of 2 different polarimeters, to be split among 4 processes. Figure 5.5 shows two different ways in which we could spit the TOD. The first solution is clearly non optimal, as the first process has much more data to process with respect to the others, meaning that the other processes will complete their tasks more quickly and will have

---

[6]https://www.open-mpi.org/
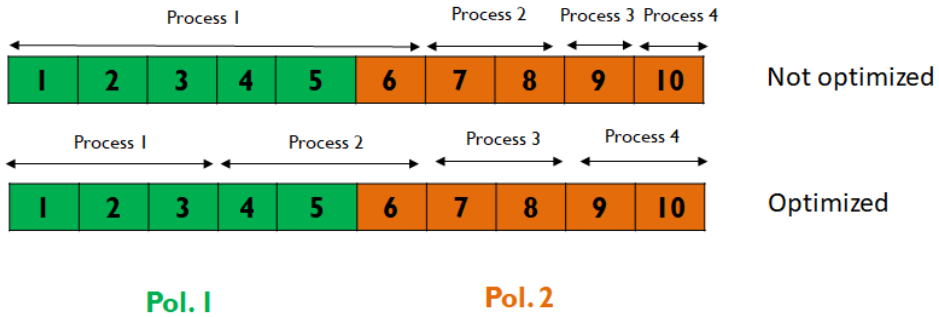
Figure 5.5: Example of TOD splitting among different computing units.

to wait. The best way is to evenly distribute the data among the processes, as proposed by the second solution depicted in the Figure.

Module tod_splitter contains a series of functions that efficiently split the TOD among the processes. The splitting is done not from the total number of samples, but from the total number of *1/f* baselines, so that each process has a finite number of baselines to deal with. This trick simplyfies the code implementation, in particular in view of the map-making process.

Given the observation time, the number of polarimeters to simulate, the baseline length and the number of MPI processes, the functions of tod_splitter conveniently split the job among the processes telling each MPI process exactly what part of the TOD it should simulate (which polarimeters from what time to what time and how many samples).

5.3.2 Scanning Strategy

As described in Section 3.2.7, the STRIP telescope will spin around the azimuth axis with constant elevation and angular velocity. In this way, the beam pattern associated to each horn will describe a circle in the sky whose radius depends on its elevation angle. Combining the motion of the telescope with the rotation of the Earth, STRIP will observe a sky-band with an amplitude that depends on the elevation of the instrument. Module scanning simulates STRIP telescope motion, returning the sky directions (declination and right ascension, in Equatorial coordinates) and the polarization angle for each time step, taking into account the different orientations of the various horns. The module also corrects for several effects like stellar aberration, Earth's nutation and precession. Default values correspond to the nominal STRIP scanning strategy, that is to say constant rotational speed of $\omega_{\text{spin}} = 1\,\text{rpm}$ (revolution per minute) and elevation angle of $20°$.

Regarding parallelization, each MPI process generates its own pointing timestream in a completely independent way from other processes, according to the TOD splitting described above.

5.3.3 Noise generation

The noise part of the TOD is modeled as a sum of white and correlated noise. We exploits the Julia module CorrNoise.jl, which employs pseudo-random number generators following the same algorithms used in the pipeline of the Planck/LFI instrument. White noise is generated from a Gaussian distribution with σ set to the desired white noise rms, while the correlated part is produced by a stochastic-differential-equation (SDE) method, that produces noise whose power spectrum is approximately of the form $P(\nu) \sim \nu^{-\alpha}$. Clearly, it is not in the form of Fa, but, as it happens in real life, contains a part that cannot be modeled with baselines. Figure 5.6 shows an example of noise TOD generated in this way. Figure 5.7 shows the PSD of a noise TOD generated with our pipeline (for a precise polarimeter) superimposed with the output of the corresponding *1/f* characterization done during the Bicocca unit tests. The overlap is very good and constitutes a validation for our noise simulation[7].

noise_generation module is able to manage the noise simulation when different MPI processes are involved. For a realistic simulation, it is crucial for the total noise TOD of a certain polarimeter to be generated from a single process. In fact, two TOD chuncks of the same polarimeter but produced separately by two different computing units are likely, once put together, to present an unphysical discontinuity at the binding.

The function that generates the noise behaves differently according to the number of processes used:

- If the number of processes is less than the number of polarimeters, Each partial noise TOD is generated by process 0 and then sent to the correspondent process.

- If the number of processes is greater than the number of polarimeters: the first "number of polarimeters" processes will simultaneously produce the noise, one process for one polarimeter (process 0 for polarimeter 1, process 1 for polarimeter 2 and so on). After that, the noise is redistributed between the computing units according to the initial TOD splitting strategy.

---

[7]To perform this validation test we have chosen a polarimeter, STRIP33, for which the *1/f* characterization during the unit tests was particularly good. This was not the case for several polarimeters, as explained in Section 4.2.5.
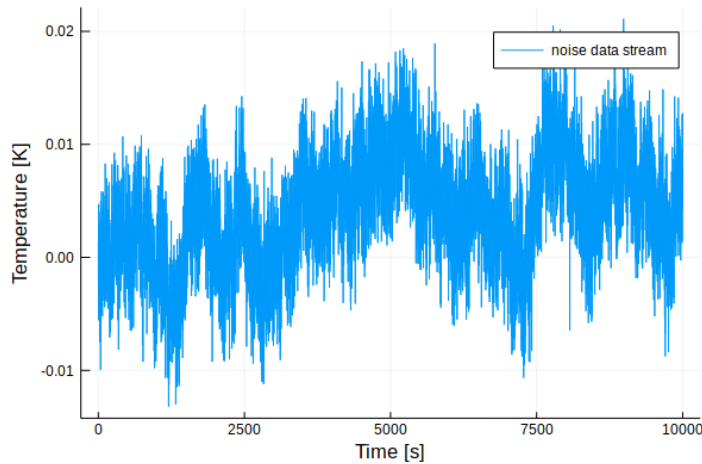
Figure 5.6: Example of noise TOD with a white noise component and a correlated component obtained with the following settings: $\alpha = 1.7$, $f_{\text{knee}} = 0.03\,\text{Hz}$, $\sigma = 0.003\,\text{K}$, $f_{\text{samp}} = 1\,\text{Hz}$.

Of course the first method is much slower than the second, but the idea is that an user running the simulation on few processes is not much interested in parallelization (e.g. if the simulated TOD is very short).

5.3.4   Map making

After each computing unit has its own partial noise TOD, it can eventually sum it to a signal TOD, obtained by scanning an input sky map chosen by the user.

At this point, the TOD and the time stream of pointings (in terms of HEALPix pixel indeces) are then passed to the map_maker module, described in 5.2.2.2, which performs the destriping and produce an output map. As pointed out before, the TOD is distributed uniformly among the available processors. When, for instance, the function performing the binning is called, each process produces a local map which involves just the pixels hit by its own section of the data, then the local maps are combined together to build a global binned map exploiting the MPI communication functions. In a similar way, after the conjugate gradient algorithm, each process will have just a section of the total array of baselines, which will be used to produce a partial destriped map. Finally, all the partial maps will be combined in a global output map.
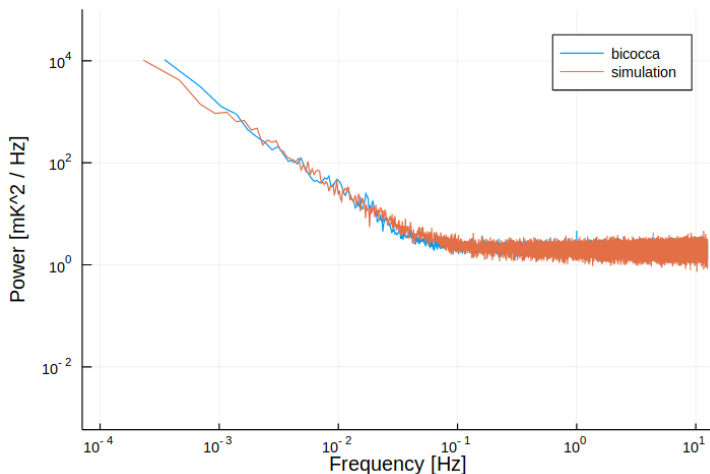
Figure 5.7: PSD of the Stokes Q TOD of polarimeter STRIP33 from the Bicocca unit characterization (light blue) superimposed with the PSD of a noise TOD generated with our pipeline (orange) using the parameters output of the test's data analysis (see Section 4.2.5) : $\alpha = 1.51$, $f_{\text{knee}} = 0.058\,\text{Hz}$, $\sigma = 0.005\,\text{K}$.

5.4 Tests and Validation

Several validation tests have been performed during the implementation of the STRIP simulation pipeline. In this Section we present the results of the most interesting ones.

First of all, some simple checks are included in the pipeline and performed every time the code is modified. The map-maker functions are called on very short TODs and the results are compared with correspondent analytical calculations. Similar tests have been also implemented for the other modules of the pipeline. Besides these short tests, I performed much longer and realistic simulations in several conditions and checked if the pipeline outputs behaved as expected. To perform heavy simulations, we used INDACO, a cluster of the University of Milan, which provides 3 nodes each with 1 TB of RAM and 32 cores, for a total of 3 TB subdivised in 96 processes.

As a representative example of the pipeline application, we present a STRIP-like simulation, obtained by scanning an input sky including all the expected polarized emissions: CMB, synchrotron, dust. This input map is a Stokes Q map at the fixed frequency of $43\,\text{GHz}$ (the average central fequency of STRIP polarimeters) and is shown in Figure 5.8. The map has

been produced with PySM[8], a python code that can be used to generate full-sky simulations of Galactic foregrounds in intensity and polarization relevant for CMB experiments and it is mostly based on the results of the Planck satellite. The settings of the simulation are listed below:

- *Observation time*: 256 days. This is the nominal observation time STRIP and corresponds to 2 years with 35% of duty cycle.

- *Sampling frequency (f_{samp})*: 50 Hz.

- *Resolution (N_{side})*: 128.

- *Baselines length (l_{base})*: 10 s.

- *Polarimeters*: all 49 polarimeters, considered identical in properties (except for the orientation angles): noise temperature $T_{noise} = 30\,K$, knee frequency $f_{knee} = 0.04\,Hz$, *1/f* slope $\alpha = 1$, bandwidth $\beta = 8\,GHz$.

Figure 5.9 and 5.10 shows the output binned map and destriped map respectively. We can see at first sight that the binned map is noisier than the destriped map, but it is by making the difference between the two maps (Figure 5.10) that we can clearly see that the destriper has removed the typical stripes due to *1/f* noise, which are instead present in the binned map. We can reach the same conclusion looking also to Figure 5.12. It shows the PSD of a 10-day section of the TOD (blue) together with the PSD of the same TOD after having subtracted the noise baselines output of the destriper (orange) and the cleaned TOD, obtained by scanning the destriped map (green). The destriper successfully suppresses the noise power of about four orders of magnitude at frequencies smaller than baseline length, in this case at 0.1 Hz (blue curve). For lower frequencies the noise is suppressed more, as baselines can model the lower frequencies better. The gap between the orange and green curve is due to white noise, since the cleaned TOD has been obtained by scanning the destriped (and therefore also binned) map. The peaks in the cleaned TOD are related to the scanning strategy: there is a peak at $\sim 1/(1min)$ corresponding to the spin frequency, the other are its harmonics. We can conclude that the destriper works reasonably well in removing *1/f* noise, given the STRIP scanning strategy and the representative values for the polarimeters performances listed above. The next step is performing more realistic simulations, customizing the noise production according to the characteristics of each single polarimeter as measured during the unit tests. Those realistic simulations have led to

---

[8]https://github.com/healpy/pysm

some preliminary sensitivity studies for the STRIP instrument, which will
be presented in the next Chapter.

Another interesting test I perfomed was the study of the computational
performance of the STRIP pipeline, checking how the computing time
of the various parts of the pipeline varies with an increasing number of
processes. I performed a 1 month simulation with all 49 STRIP polarimeters,
$f_{\text{samp}} = 50\,\text{Hz}$ and baseline length of 10 s, varying the number of processes
from 1 to 64. The results are shown in Figure 5.13. The code behaves as
expected: the time needed to generate pointings decreases as the number
of processes that splits the job increases. The noise generation takes much
more time when less than 49 processes (i.e. the number of polarimeters)
are used, as in this case the first method of noise generation is applied
(all noise TOD generated by process 0); if, instead, we use more than (or
equal to) 49 processes, the noise production is splitted among them and
is therefore much less time consuming. The destriper shows a decreasing
trend until about ~ 40 processes but then it shows a slight increase. This
is due to the fact that from a certain number of processes involved, the
time spent in communications and trasfers of data between the processes
becomes important. The Figure also shows the behaviour of the total
simulation. For complete STRIP simulations (2 years with 35% duty cycle,
49 polarimeters, $f_{\text{samp}} = 50\,\text{Hz}$, baseline length of 10 s and 90 processes)
typical times are: $\sim$20 minutes for the pointing generation, $\sim$17 minutes for
the noise generation and $\sim$13 minutes for the destriper. This means about
~ 50 minutes for a complete simulation.
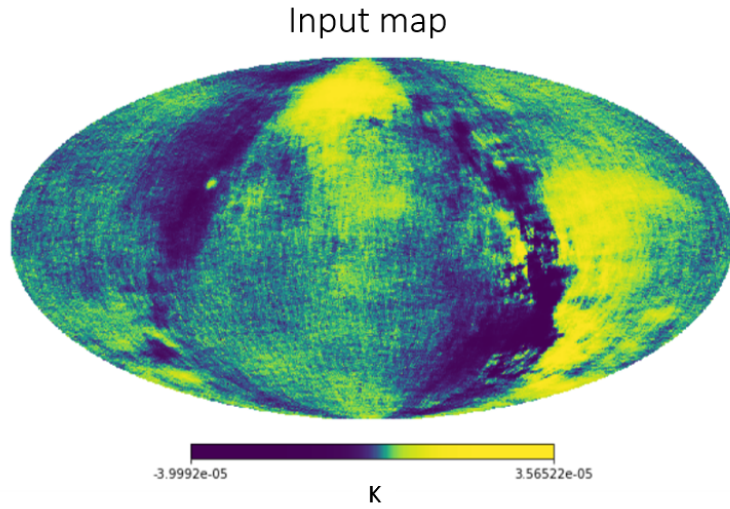
Figure 5.8: PySM map of Stokes Q in equatorial coordinates including the signal of CMB, synchrotron and dust at $43\,\mathrm{GHz}$.
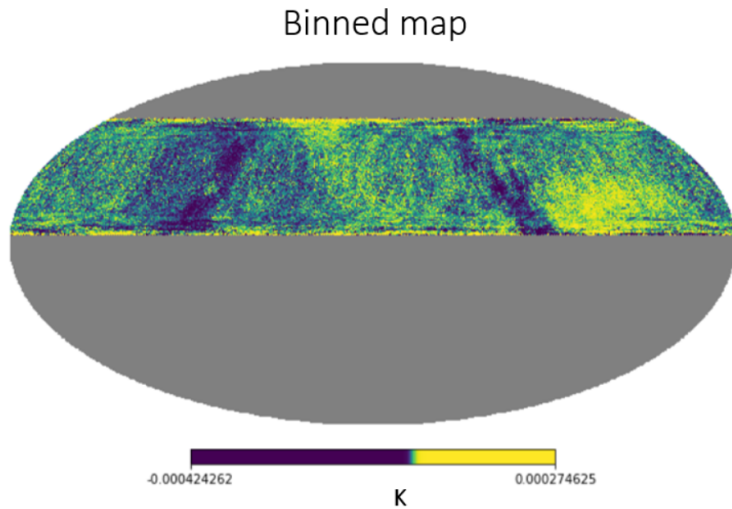
Figure 5.9: Binned map resulting from the simulation described in the text.
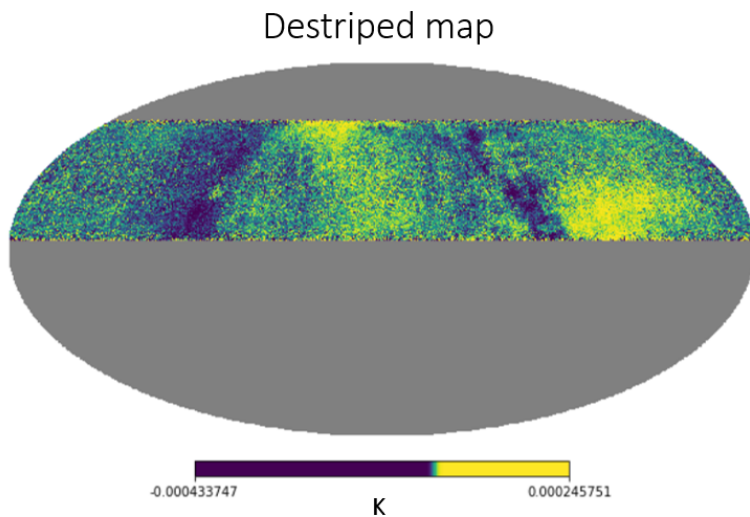
Figure 5.10: Destriped map resulting from the simulation described in the text.
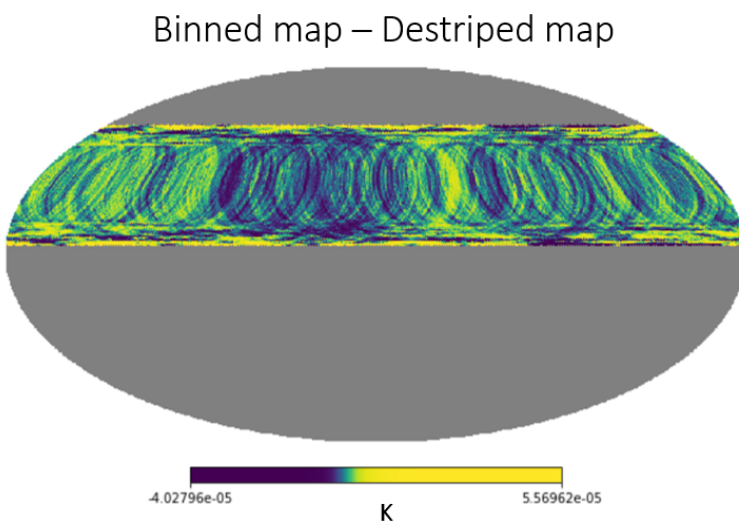
Figure 5.11: Difference between the binned and the destriped map, in order to isolate the *1/f* baselines reconstructed by the destriper.
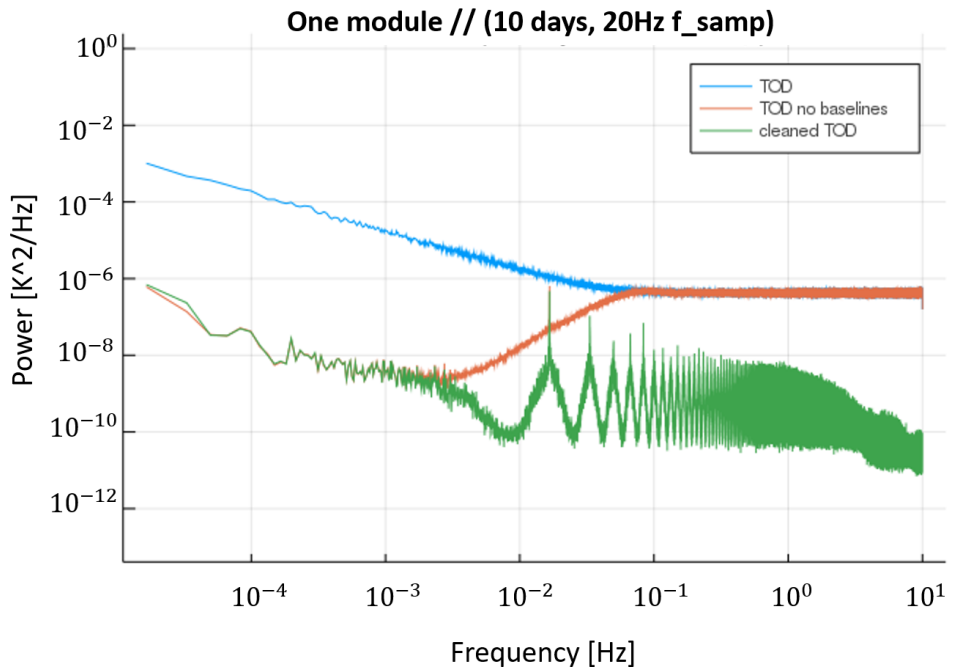
Figure 5.12: PSD of a 10-days TOD (light blue) measured by a single STRIP module (7 polarimeters) together with the FFT of the same TOD after having subtracted the *1/f* baselines (orange) and the cleaned TOD, obtained by scanning the destriped map (green).
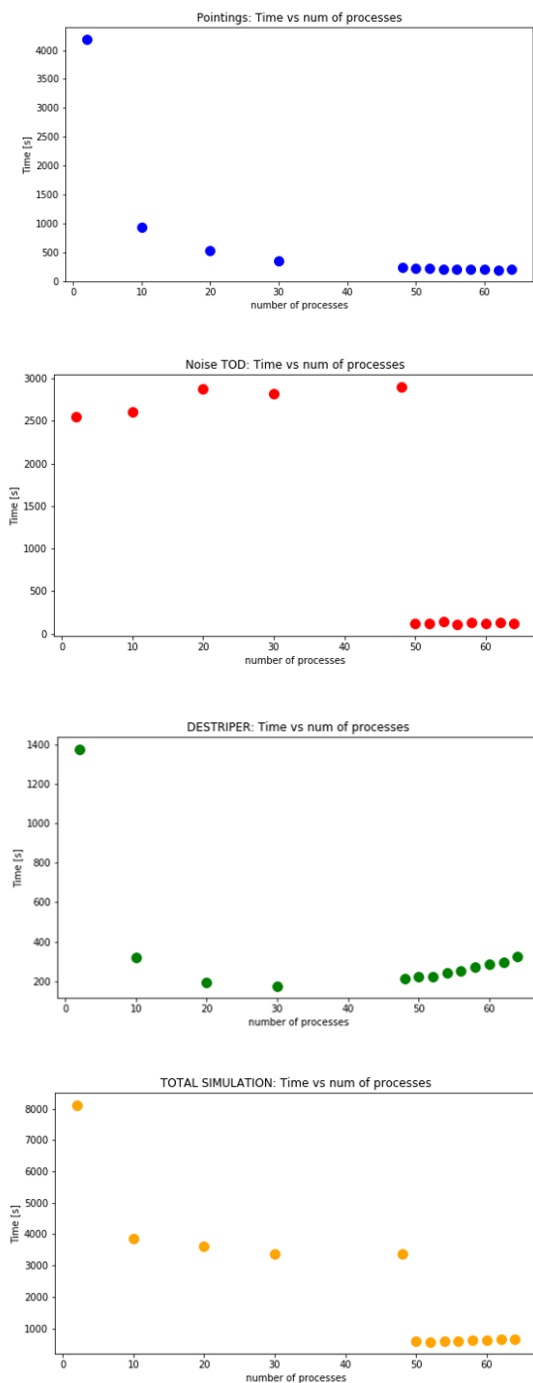
Figure 5.13: STRIP pipeline performances in terms of computational time vs. num-
ber of MPI processes involved. The performance of each part of the
pipeline (pointing generation, noise generation, destriper) is evaluated
separately. The behaviour of the total simulation is also shown.

Chapter 6

Sensitivity Studies

The last activity of this PhD thesis consisted in the exploitation of the simulation pipeline described in Chapter 5 to perform preliminary sensitivity studies for the LSPE/STRIP experiment. In particular, I focused on the study of the residual correlated noise (see Section 6.1), and on the evaluation of the bandpass mismatch (see Section 6.2).

To carry out simulations as realistic as currently possibile, I used the results from the polarimeters unit tests described in Chapter 4 to produce different noise time streams according to the characteristics of each polarimeter. In particular, the bandwidth β and the noise temperature T_{noise} were used to compute the white noise level σ, according to the radiometer equation:

$$\sigma[\text{K}] = \frac{T_{\text{CMB}} + T_{\text{tel}} + T_{\text{atm}} + T_{\text{CMB}} + T_{\text{noise}}}{\sqrt{\beta \cdot \tau}}. \tag{6.1}$$

T_{CMB} and T_{tel} are respectively the brightness temperature of the CMB and of the telescope (mirrors, windows, feedhorns) that enter each polarimeter. Their values are estimated to be 1.8 K and 7.5 K respectively (see also Table 3.2). As explained in Section 2.2.3, the brightness temperature of the atmosphere T_{atm} depends on the thickness of the atmosphere layer crossed by the line-of-sight of the telescope, and thus it depends on the elevation angle θ according to the secant law:

$$T_{\text{atm}} = T_z \cdot \sec \theta. \tag{6.2}$$

The value of the atmospheric brightness temperature at the zenith T_z has been extrapolated for Teide Observatory site through the AM (Paine, 2019)

and ATM (R. Pardo, Cernicharo, and Serabyn, 2002). The result is about $18\,\mathrm{K}$ at $43\,\mathrm{GHz}$, which means $T_{\mathrm{atm}} \simeq 19\,\mathrm{K}$[1]. $\tau = 1/f_{\mathrm{samp}}$ is the integration time corresponding to a single measurement, making Equation 6.1 an estimation of the white noise extent affecting each sample.

The information about the noise spectral behaviour, namely the knee frequency f_{knee} and the *1/f* slope α, instead, have been used to generate the correlated component of the noise. As mentioned in Section 4.2.5, unfortunately, the *1/f* characterization was performed only for 37 polarimeters out of 49. For those polarimeters without a valid estimate of f_{knee} and α, we randomly pick a value from the available measurements of the other polarimeters, so that the distributions of f_{knee} and α do not change.

The knee frequencies measured in lab cannot be used as they are, as the signal "seen" by each polarimeter in the experimental setup of Bicocca unit tests is estimated to be about $21.3\,\mathrm{K}$ (Pincella, 2017), while in the real data taking in Tenerife it would be of about 28.5 K ($T_{\mathrm{atm}} + T_{\mathrm{tel}} + T_{\mathrm{CMB}}$). Moreover, the sampling frequency in Bicocca was $25\,\mathrm{Hz}$, while in Tenerife will be $50\,\mathrm{Hz}$, which means that also the value of τ is different in the two cases. As a consequence, the white noise level σ in Tenerife will not be the same as it was during the unit tests. Figure 6.1 visually shows that the immediate consequence is a variation of the f_{fknee}, which will be lower in Tenerife. We should therefore adapt the f_{knee}s measured in Bicocca to the nominal conditions there will be in Tenerife during data taking. Calling $P(f)$ and $P'(f)$ the noise Power Spectral Density (PSD) of a polarimeter measured at Tenerife and at Bicocca unit tests respectively, we have:

$$P(f) = \sigma^2 \left(1 + \frac{f_{\mathrm{knee}}}{f}\right)^\alpha \qquad P'(f) = \sigma'^2 \left(1 + \frac{f'_{\mathrm{knee}}}{f}\right)^\alpha , \qquad (6.3)$$

and, since the two functions must be asymptotic for $f \to 0$, we ask that:

$$\sigma \left(\frac{f_{\mathrm{knee}}}{f}\right)^\alpha = \sigma' \left(\frac{f'_{\mathrm{knee}}}{f}\right)^\alpha , \qquad (6.4)$$

from which we get the relation that we can use to correct the f_{knee}s:

$$f'_{\mathrm{knee}} = f_{\mathrm{knee}} \left(\frac{\sigma}{\sigma'}\right)^{\frac{1}{\alpha}} . \qquad (6.5)$$

---

[1] Actually, a recent more precise extrapolation, done after the conclusion of these sensitivity studies, suggests a slightly lower value for T_z, of about $16.5\,\mathrm{K}$. Anyway, this is a minor correction that does not affect significantly the conclusions presented in this Chapter.
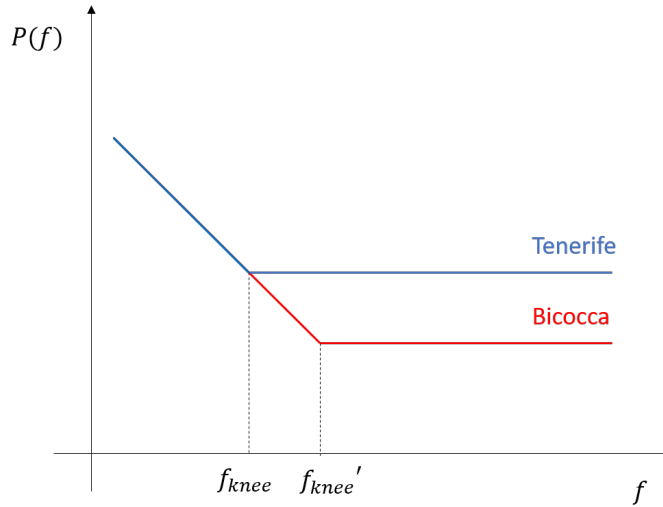
Figure 6.1: Comparison of the noise PSD of a generic polarimeter at Bicocca unit tests and at Tenerife. Since the white noise level is not the same in the two cases, f_{knee} will be different too.

6.1 Noise simulations

To quantify the noise level in STRIP maps and the impact of residual *1/f* after destriping, I performed noise only simulations (no sky signal) with the following simulation settings:

- *Observation time*: 256 days (2 years with 35% of duty cycle).

- *Sampling frequency* (f_{samp}): 50 Hz.

- *Resolution* (N_{side}): 128.

- *Baselines length* (l_{base}): 10 s.

- *Polarimeters*: all 49 polarimeters, each one simulated with its own properties (T_{noise}, f_{knee}, α and β) measured during unit tests and presented in Table 4.1. f_{knee}s have been corrected according to equation 6.5.

I ran three different types of noise only simulations, namely:

- the realistic case: TOD with both *1/f* and white noise, output map produced with the destriper.

- the no-destriper case: TOD with both *1/f* and white noise, output maps produced through simple binning.

- the white noise only case: TOD with just white noise, output map
  produced through simple binning.

In this way, we can directly see the effect of the destriper on a realistic noise
TOD (*1/f* noise + white noise) compared to the case in which the destriper
is not applied and evaluate the impact of the residual correlated noise in
comparison with the ideal case of a white-noise only TOD. As seen in
Section 1.6.2, to study the statistical property of CMB polarization field, it is
possible to decompose it into spherical harmonics, similarly to what we do
with its temperature field. In particular, this is done by computing E-modes
and B-modes power spectra from the Stokes Q and U CMB maps. Although
E- and B-modes have a specific physical meaning when referred to CMB, it
is possible to apply the same mathematical procedure and compute them
for any kind of Q and U maps, even noise maps. Since the ultimate purpose
of the LSPE experiment is the measurement of the CMB polarization pattern,
comparisons among our noise-only simulations have been done in terms
of EE and BB auto-spectra. We computed the angular power spectra with
the PolSpice software, which, as mentioned in Section 5.1.4, is a pseudo-
C_l estimator. This means that PolSpice returns an un-biased estimator of
the C_l whose average on many different random realizations of the same
model converges toward the true spectrum. For this reason, I performed a
Monte Carlo simulation for each case listed above, running the simulation
several times with different noise realizations. As seen in Chapter 5.3, the
simulation pipeline is fast enough to support Monte Carlo studies, especially
because the pointings remain the same for all realizations and therefore the
part of the pipelines that generates the pointings (and that dominates the
computing time) has to be run just once. For each realization, I computed
the EE and BB autospectra from the output Q and U maps and then I
evaluated the average of all the available spectra.

The results are shown in 6.2, where the average power spectrum of 40
noise realizations computed in the three simulation cases (realistic, no de-
striper and white noise only) is plotted. Figure 6.3 shows all the realizations
in order to give an idea of the spread of the results. The multipoles are
shown from $l = 30$; when using PolSpice to estimate the spectrum from a
map covering only a fraction of the sky, it is in fact suggested to exclude
the lowest multipoles from the computation, in order to avoid spurious
oscillations in the spectrum. Comparing the no-destriper case (orange line)
with the realistic case (green line), we can see that the destriper behaves as
expected, strongly reducing the *1/f* noise by several orders of magnitude.
However, the destriper is not able to completely suppress correlated noise
and leaves large scale features in the destriped maps, which affect the power
spectrum at low multipoles ($l < 100$), as we can clearly see from the EE

plot. In general, the residual noise in a destriped map comes from two components: unmodelled noise (all noise sources at frequencies higher than the chosen baseline length) and destriping error. The destriping error, i.e. the error in the baselines determination, is the dominant component of residual noise at low multipoles (Kurki-Suonio et al., 2009). The residual correlated noise in the map due to the non-optimal reconstruction of the *1/f* baselines also leads to very bad sprectrum estimations in some cases (see Figure 6.3) with spurious unphysical oscillations. For B-modes, this effect is even enhanced.

As explained in previous Chapter, the length of each baseline segment l_{base} is the only free parameter of the destriping algorithm and its optimal value is related to the f_{knee} as $l_{\mathrm{base}} \simeq 1/(2 f_{\mathrm{knee}})$. Since the mean f_{knee} of our polarimeters is about 0.05 Hz, we chose a baseline length of 10 s for our simulations. Figure 6.4 how the result changes in terms of E-modes spectrum with different choices of l_{base}, namely 1 s, 2 s and 60 s. Short baselines are less able to reduce *1/f* noise, which may be unexpected at first sight since it is logical to think that a vector of shorter baselines would follow more accurately the *1/f* noise time stream. Although short baselines can potentially model correlated noise better, they actually fail because they are dominated by white noise and include too little measurements to mitigate the large random values they pick. The 10 s and 60 s spectra are quite similar, with a slightly better result for 10 s at high l, where the spectrum estimation is more reliable. The usage of different baselines length has obviously an impact on the computational time of the destriper, because of the different number of variables to solve for: $\sim$ 6 min for $l_{\mathrm{base}} = 60$ s, $\sim$ 13 min for $l_{\mathrm{base}} = 10$ s, $\sim$ 1 hour and 10 min for $l_{\mathrm{base}} = 2$ s and $\sim$ 2 hours and 30 min for $l_{\mathrm{base}} = 1$ s. Even by varying the baseline length, the destriper is not able to correctly model the *1/f* noise and leaves a residual in the power spectrum, together with spurious oscillations. The main reasons for this behaviour together with possible ways to improve the destriper effectivenees will be discussed in Section 6.1.0.1.

Figure 6.5 shows the results of the noise simulations in comparison with physical signals in order to get an idea of STRIP sensitivity. The realistic case (green line) is shown, together with the white noise only case (blue line) as it represents a sort of "best case" to which the map-maker aims. The comparison is done with the expected synchrotron signal (pink line) and with the expected EE and BB spectra of the Cosmic Microwave Background, obtained with the CAMB software[2], setting a tensor-to-scalar ratio of 0.07,

---

[2]The Code for Anisotropies in the Microwave Background (CAMB) is a Fortran 90 application that computes CMB spectra given a set of input cosmological parameters. It has a web interface at https://lambda.gsfc.nasa.gov/toolbox/tb_camb_form.cfm
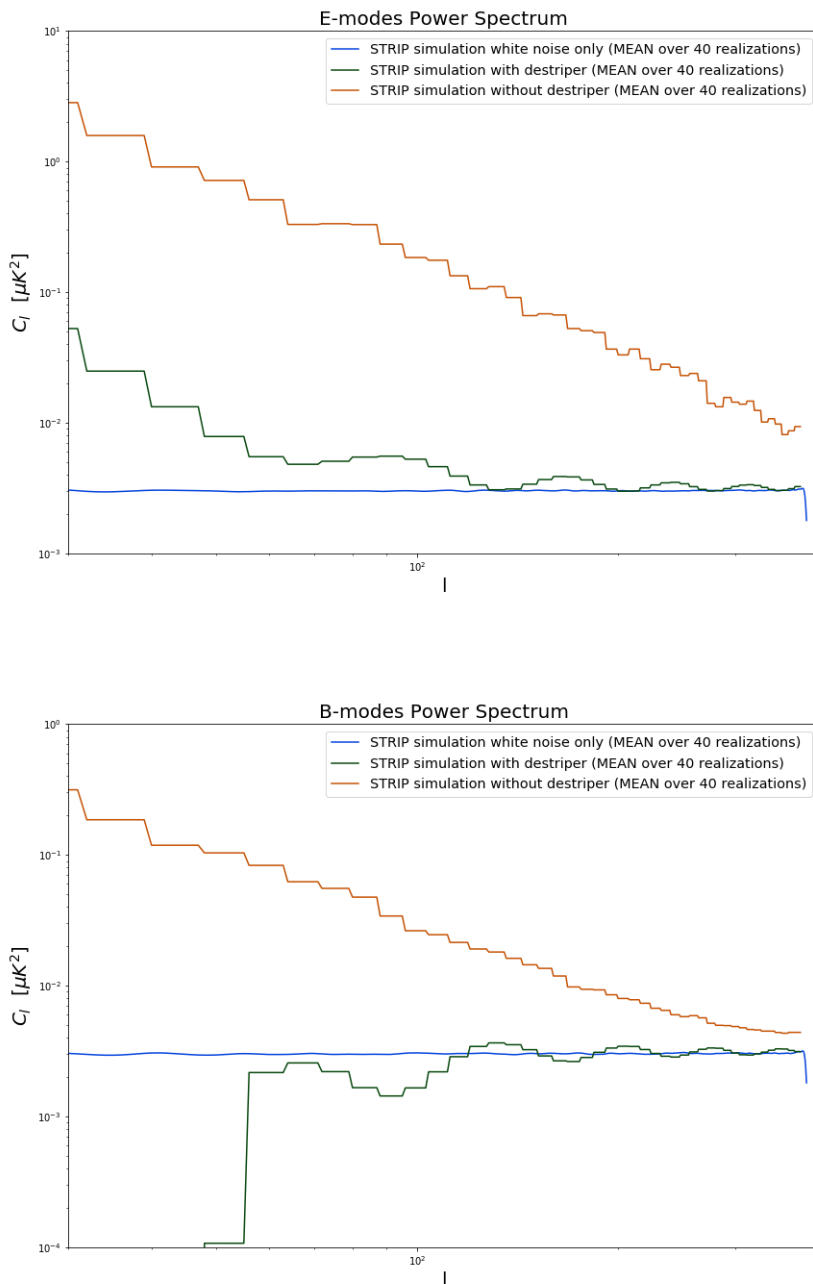
Figure 6.2: EE *top* and BB *bottom* auto-spectra showing the results of the simulations
described in the text: white noise only (blue), no-destriper (orange) and
the realistic case (green). Each curve is the average power spectrum
over 40 noise realizations.
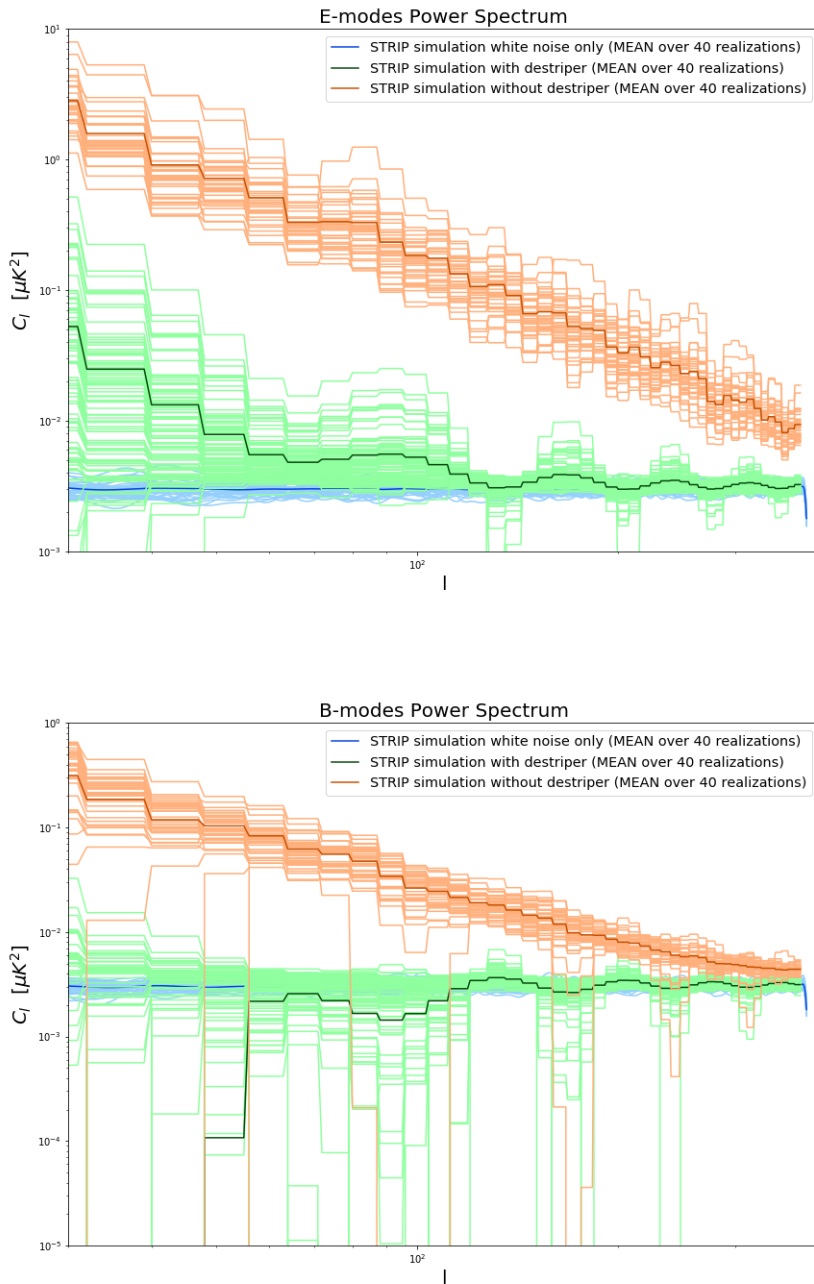
Figure 6.3: This plot shows the results of all Monte Carlo realizations for each simulation case described in the text. The average power spectrum is highlighted.
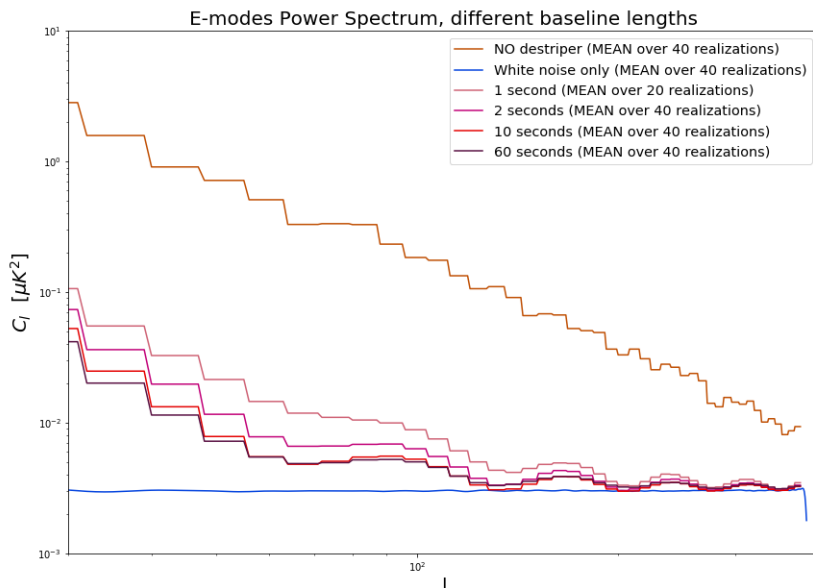
Figure 6.4: EE power spectrum obtained by using different baseline lengths: 1 s, 2 s, 10 s, 60 s, compared with the white noise only simulation. All curves are averages over 40 Monte Carlo realizations.

which is the current experimental limit). Because of its proximity to the STRIP Q-band channel, we plotted also the power spectrum of the simulated white noise level of the 44 GHz Planck map[3] (gray line). We can see that the white noise level is about 4 times lower for STRIP than for Planck, which means that STRIP has a better sensitivity in terms of both E-modes and B-modes than Planck. This is true, of course, only in the case we are able to completely remove correlated noise and other systematics effects. Understanding how to better reconstruct the spectrum at low multiples is crucial also because it is the only range where synchrotron signal is stronger than white noise. CMB signal is much lower and out of STRIP sensitivity (especially B-modes). We remind that it is well expected and of no concern, since the masurement of CMB polarization is the aim of STRIP and SWIPE together, with SWIPE having the most sensitive channels to CMB and STRIP focusing on the synchrotron characterization.

---

[3]Downloaded from the Planck Legacy Archive https://pla.esac.esa.int/
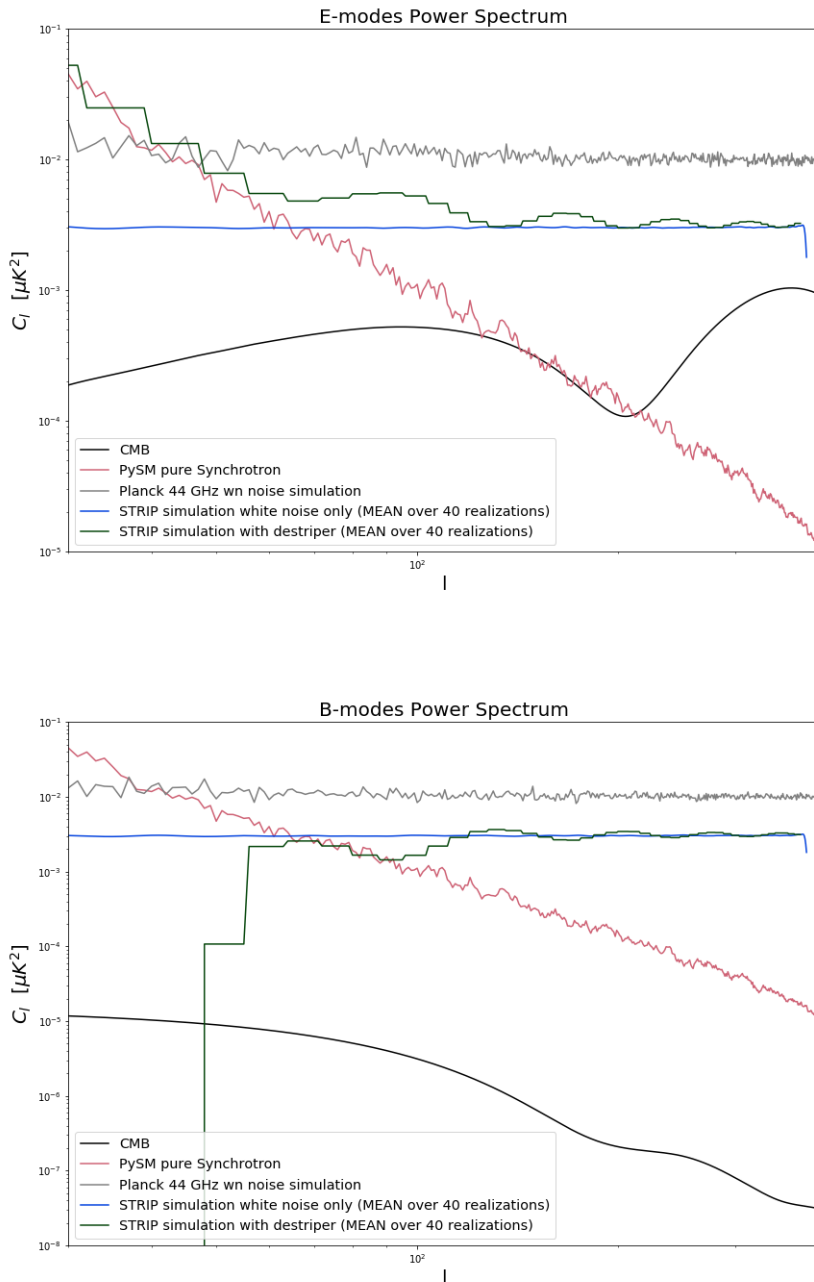
Figure 6.5: EE *top* and BB *bottom* auto-spectra showing the results of white noise only (blue) and realistic case (green) simulations. Each curve is the average power spectrum over 40 noise realizations. For comparison, also the power spectra of the simulated white noise level of the 44 GHz Plack maps (grey) is plotted, together with the spectrum of the expected synchrotron signal, obtained with PySM and the expected CMB signal obtained with CAMB (setting $r = 0.07$).

6.1.0.1   Discussion and outlook

This non-optimal behaviour of the destriper has mostly two reasons. The first is that an important fraction of STRIP polarimeters have high *1/f* slopes ($\alpha > 1$), thing that increases the level of the correlated noise component in the data that the destriper has to remove. The second reason stands in the fact that STRIP polarimeters have very different noise properties. Slopes can vary from less than 0.5 to more than 2, and f_{knees} varies from few mHz to few Hz. This very strong non-homogeneity makes the *1/f* modeling that underlies the standard destriping algorithm not accurate enough.

It is important to stress that, as already said in Chapter 4, the noise properties of the polarimeters measured during the unit tests are not optimized and, thus, just preliminary. The *1/f* characterization, in particular, is not reliable for some polarimeters and even missing for others. To make simulations with the ultimate and final characterization parameters of all polarimeters, we need to wait the conclusion of the system tests, which will be carried out in Bologna until at least Summer 2020.

If, however, the system tests will confirm this great non-homogeneity in noise properties, figuring out how to perform an accurate map-making for STRIP would be a serious issue. Although it has proven to be a very reliable and convenient map-making method for several experiments, the studies here presented show that the "standard" destriper would not be an optimal choice for STRIP. We have came up with some possible solutions that will be probably worth trying:

- Since the knee frequencies of STRIP polarimeters varies over three orders of magnitude, using a different value of l_{base} for each polarimeter would help to better model each noise time stream. Among the solutions proposed, it is probably the fastest to implement as the destriper in STRIP pipeline is already generalized to manage different baseline lengths.

- We have seen that although short baselines are expected to model correlated noise better, they actually behave worse as they are dominated by white noise random fluctuations. This can be remedied by using prior information on the noise spectrum to prevent too large differences between the amplitude of nearby baselines. In other words, in the traditional destriper we consider the baselines as independent, but we know that it is not true in real-life and, instead, the amplitude of nearby baselines is correlated. It is possible to use this prior knowledge in the destriping algorithm by computing the covariance matrix of the baselines. Recalling the map-making matrices from Chapter 5, under the assumption that the white noise component and the corre-

lated noise component are independent, we can write the total noise covariance matrix as:

$$C_n \equiv \langle nn^T \rangle = FC_aF^T + C_w, \tag{6.6}$$

where $C_w = \langle ww^T \rangle$ is the white noise covariance and $C_a = \langle aa^T \rangle$ is the covariance matrix for the baseline amplitudes a and constitutes the noise prior we were talking about. In a other words, we add one step to the destriping algorithm, namely the computation of the noise prior C_a as the covariance matrix between a set of reference baselines functions $\tilde{a}$ (for uniform baselines, the reference value is the average of the noise stream in a time l_{base}). A general formula to compute the elements of the matric C_a is provided by Keihanen and al., 2005 and Keihanen et al., 2009. With a prior, the destriping equation 5.27 becomes:

$$(F^T C_w^{-1} ZF + C_a^{-1})a = F^T C_w^{-1} Zy. \tag{6.7}$$

After having computed C_a, the conjugate gradient technique is used to solve a from Equation 6.7. The tricky part here is the evaluation of the term $C_a^{-1}a$, since matric C_a can be very large. However, like maximum-likelihood algorithms do on the total noise covariance matrix C_n, some assumptions on the C_a matrix are usually made. For example, the noise is assumed to be stationary, i.e. the properties of the correlated noise component do not change with time. As we have seen in Section 5.2, this means that matrix C_a depends on indices i, i' only through their difference, making it approximable by a circulant matrix. With this approximation, the evaluation of $C_a^{-1}a$ becomes less computational time consuming as circulant matrices can be diagonalized with a discrete Fourier transform. Kurki-Suonio et al. (2009) shows that the noise prior has a dramatic effect on the performance of short baselines and results keep improving as the baselines is shortened. This means that, with a noise prior, we can improve the destriper performances at will, extending the method to very short baselines, which model the noise better (paying of course the toll of longer computing times). The destriper + noise prior is, for instance, the strategy followed by MADAM (Keihanen and al., 2005), a map-maker developed for the Planck experiment.

- Use a maximum-likelihood method (like ROMA (de Gasperis et al., 2005)), solving equation 5.10 without approximating the *1/f* noise as a sequence of baselines. This method would produce optimal maps and solve the problem of the residual correlated noise in the maps, but in much longer computational times. If we choose this path we

would probably look for more powerful computing facilities, as the medium-size cluster we used so far, would not be able to sustain the heavy computations a M-L requires.

For STRIP, however, the situation is much more complicated than it was for Planck, thing that would actually prevent us to implement a MADAM-like destriper or a standard M-L (or even use directly MADAM or ROMA on STRIP data). The problem is related to the assumption of stationary noise that underlies both MADAM and the most used M-L methods. The diagonal of the matrix C_a contains the variance of the baselines of all detectors, placed in sequence. However, while Planck detectors were very similar in properties, this is not the case for STRIP and we cannot really say that C_a (or C_n) depends on indices i, i' only through their difference, since each part of the matrix corresponding to a different polarimeter would have different noise properties. Of course, if this were the only issue, we could consider noise stationary in each block corresponding to a single polarimeter and treating the C_a matrix as a circulant block matrix. However, unlike Planck, STRIP is a ground-based experiment, which means that the assumption of stationary noise is not valid a priori. As Equation 6.1 shows, the noise level in data depends on the intensity of the signal entering the polarimeter, which, for a grund-based experiment, is crucially related to the atmosphere. Seasonal or day/night variations on the mean atmosphere brightness temperature and short time-scale turbolences, in fact, continuosly change the signal power seen by each polarimeter, making the noise definitely not stationary. Moreover, as 6.1 shows, white noise variations implies changes of the f_{knee}, which means a variability of the instrumental correlated noise. In conclusion, if the unit tests measurements would be confirmed, understanding the best way to perform map-making would require a deep study, as the traditional methods are not suitable for the STRIP case.

6.2   Bandpass mismatch

The simulation pipeline described in Chapter 5 is suitable for the study of several sistematics effects, already presented in Section 2.2.3. Besides the *1/f* residual, directly connected to the destriper performance and presented in the previous Section, I focused on the bandpass mismatch, exploiting the results of the analisis I have done on the bandpass characterization data obtained during the unit tests and described in Section 4.2.3. As already mentioned, bandpass mismatch arises from the fact that different detectors have in general different bandpass responses $I(\nu)$. This means that different detectors are more or less sensitive to the signal from the sky, according to its frequency. This mismatch introduces an error in the map, as the

map-making process assumes the sky signal from each pixel to be constant and the same for all detectors. In real life this is not true and the measured sky signal would depend on the bandpass response of each polarimeter. To quantify the entity of the artifacts introduced in the map because of the bandpass mismatch, I perfomed the following simulation:

1. using PySM, I produced an input map at 43 GHz including all Galactic polarized components: CMB, synchtrotron radiation and dust. We exploited PySM functions to produce 49 different maps, each one customized for each STRIP polarimeter and obtained by convolving the sky signal with their measured bandpass response.

2. I performed 40 signal+noise simulations into two different cases: *i)* all polarimeters looking at the same 43 GHz map and *ii)* each polarimeter scanning its own sky map. To isolate the effect of the bandpass mismatch from the unavoidable differences in the final map caused by noise fluctuations, each Monte Carlo realization has been done with the same noise TOD in the two cases.

3. I produced 40 "difference maps", by making the difference of the two maps for each noise realization.

The E-modes and B-modes mean spectrum of the difference maps is shown in Figure 6.6, in comparison with the white noise spectrum and the spectrum of the residual *1/f*, evaluated in the previous section. The bandpass mismatch spectrum is orders of magnitude lower than the white noise level (especially in terms of E-modes) and becomes even lower at high multipoles. We stress that, even if we have contained the noise contribution in the final map by making the difference between two maps with the noise TOD, the noise dependence is not zero since they are still destriped maps on overall different TODs (as the sky signal part is different) and thus the baselines estimation can be different in the two cases.
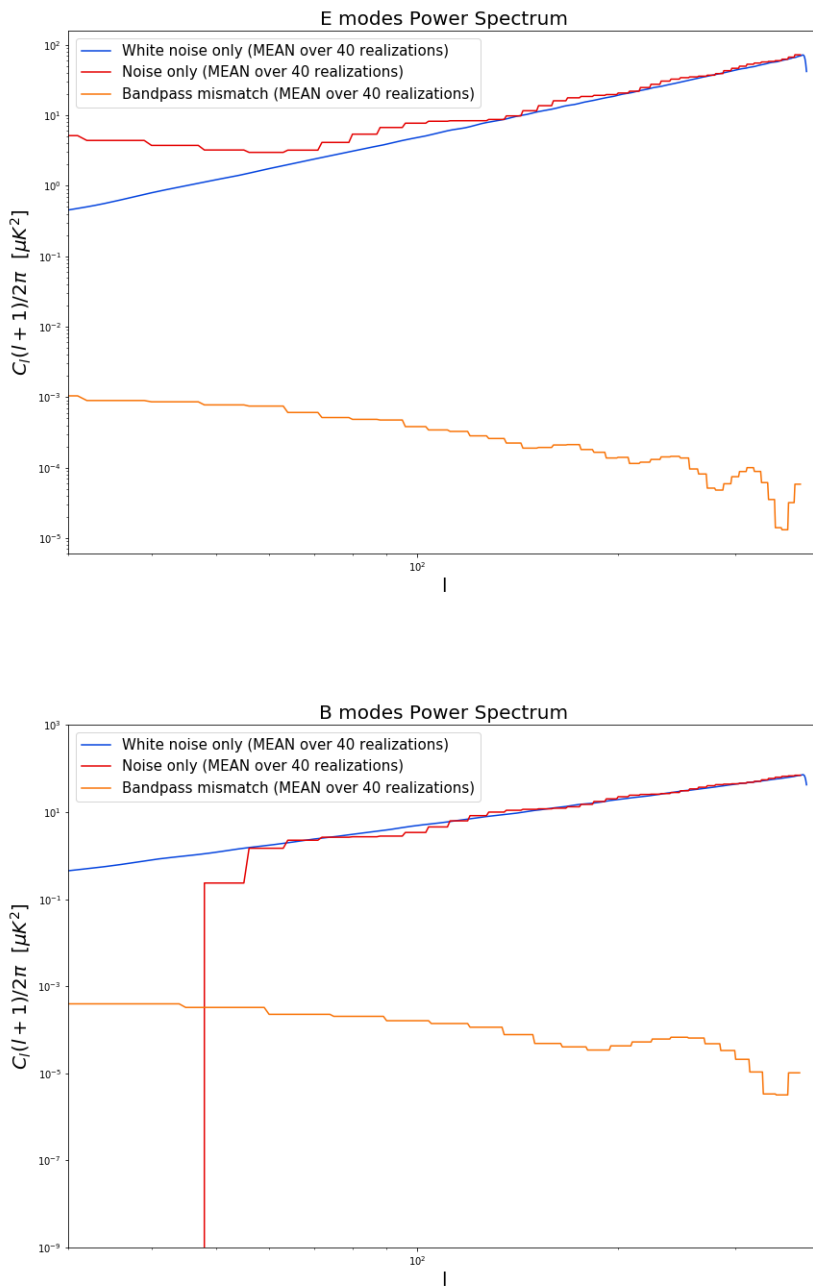
Figure 6.6: EE *top* and BB *bottom* autospectra showing the systematic effect due to the bandpass mismatch (orange) in comparison with the white noise level (blue) and the correlated noise residual (red).

6.3 Future developments

The developed pipeline allows us to perform end-to-end simulations of the STRIP sky observations through the production of TODs with a realistic noise and the reconstruction of the map by means of the destriping algorithm. As we have seen, this is enough to perform preliminary studies about the scientific performance of the instrument and gives us important indications about how to orient the future data analysis strategy. However, the pipeline is not yet complete and there is room for a number of improvements, concerning in particular the simulation of systematics effects:

- *Effect of optical beams*: measurements carried out in the anechoic chamber already provided us the characterization of the optical beam pattern of all STRIP horns. Adding a dedicated module to the pipeline able to simulate the observation of the sky considering the actual angular response, will be of great importance in order to understand the impact of beam asymmetries and sidelobes pickup on the final results. A Preliminary work in this context is ongoing.

- *Atmosphere*: being a ground-based experiment, STRIP will have to deal with the atmospheric signal. The atmosphere can constitute an important limitation to STRIP ultimate performance, as its temporal and spacial inhomogeneities introduce spurious signals in the time order data acquired, not trivial to remove. Simulations of the atmosphere contribution would be of crucial importance, but the problem is complex and requires a deep study. Work is already ongoing, with the final purpose to add a dedicated atmosphere module to the pipeline.

- *Polarimeters non-idealities*: as mentioned in Section 2.2.3, non-idealities in the polarimeters architecture can cause $I \rightarrow Q/U$ and $Q/U \rightarrow U/Q$ leakage effects. In the present state of the pipeline, input Q or U maps are scanned as they are, but the inclusion of non-idealities in the polarimeter behaviour would be of interest in view of high accuracy simulations. Indeed, leakage effects are expected to be only a minor correction: a preliminary work by Krachmalnicoff, 2015 showed that these effects have a negligible impact on the measurement of the synchrotron radiation at 43 GHz, showing that the STRIP polarimeter architecture itself is capable of minimizing this kind of systematic effects.

- Other systematics: the simulation of other systematics effects like the pointing uncertainties, the uncertainty in the polarization angle

and the gain fluctuations are foreseen to be included soon in the pipeline. A module simulating the response of an ADC has been recently included but end-to-end simulations to quantify the impact on ADC non-linearities on the final performance are yet to be carried out.

Conclusions

This thesis work has been carried out in the framework of the LSPE experiment, designed to measure the polarized signal of the Cosmic Microwave Background and in particular to constrain the B-modes component of the polarization. LSPE is build of two completely independent instruments, SWIPE and STRIP, looking at the same area in the Northern sky at five different frequencies.

During my PhD I have been working for the STRIP instrument, whose aim is to provide wide maps of the Galactic synchrotron foreground through a two-years observation campaign at the Teide Observatory in Tenerife, scanning the sky with 49 radiometric polarimeters centered at 43 GHz.

In the first part of my PhD I was actively involved in the characterization tests of STRIP polarimetric modules, which took place at the University of Milano Bicocca. During the unit tests campaign, the functionality of each polarimeter has been tested and the characterization of its bandpass response and of its noise properties has been carried out. I participate to the STRIP unit tests both as an operator in the laboratory and as a data analyst, focusing in particular on the analysis of the bandpass response. The result of this test campaign has been the population of the STRIP focal plane, together with the filling of a database holding preliminary characterization data for all polarimeters. The ultimate and optimized instrumental characterization will be carried out during the system tests, already ongoing in Bologna and foreseen to last until Summer 2020.

The greatest part of my PhD thesis, however, has been devoted to the development of a simulation pipeline for the STRIP instrument, focusing on the generation of a realistic data time stream and on the implementation of a map-maker. Among the various approaches to map-making for CMB experiments, we chose the destriping technique, which models the correlated component of the noise as a sequence of constant baselines. The destriping

algorithm has been proven to be extremely successful for many experiments, providing a high-fidelity reconstruction of sky maps in a fraction of computational time with respect to the more accurate (but time consuming) maximum-likelihood methods. As the matrixes involved in the map-making equations can be made of trillions of samples, the implementation of a destriper is not trivial.

The simulation code, written in Julia and fully parallelized with MPI, is able to carry out a complete end-to-end simulation of the STRIP observation campaign in about 50 minutes on the INDACO cluster of the University of Milano. Exploiting the speed of the simulation pipeline, I ran Monte Carlo end-to-end simulations of the STRIP sky observations, recovering maps and power spectra in order get information about the scientific performance of the experiment. In this simulations, I exploits the informations on the instrumental characteristics measured during the unit tests (bandwidth, fknee frequency, *1/f* slope and noise temperature), producing data streams customized for each polarimeter on the focal plane of STRIP.

The simulations show that the destriper behaves well in removing the greatest part of the *1/f* noise, but it leaves a noise residual in the map affecting in particular the low multipoles of the power spectrum. This non optimal behaviour is mainly due to the great non-homogeneity of the noise properties of STRIP polarimeters, together with the presence of some modules with very high correlated noise. Possible solutions to this problem could be, in principle, the usage of different baseline lenghts for different polarimeters, the inclusion of a noise prior in the destriping process or, ultimately, the use of a M-L approach.

However, the fact that STRIP is a ground based experiment makes things more complicated, as the crucial assumption of stationary noise that stands at the base of most of traditional map-making approaches cannot be made. Therefore, if confirmed by the system level tests, STRIP noise properties could be an issue for map-making and a deep study in this context would be necessary.

The simulation pipeline I implemented can be used for the study of a number of systematics effects. Besides the study on the residual *1/f* noise connected to the destriping performance, I studied the bandpass mismatch effect, relying on the analysis I performed on unit tests bandpass response data. The simulations show that the bandpass mismatch impact is negligible if compared with the Galactic signal and it is order of magnitudes lower than the white noise level in the output sky maps.

As pointed out, the pipeline has room for improvements, as it does not include yet the simulation of many systematics effects like the optical beams and the atmospheric modeling.

I would like to mention that the work presented in this thesis has been

carried out in the context of a large scientific collaboration, as it often happens in modern experimental physics, and therefore includes also the efforts of several colleagues who I thankfully acknowledge here.

Bibliography

Abazajian, K. N. et al. (Oct. 2016). "CMB-S4 Science Book, First Edition". In: *ArXiv e-prints*. arXiv: 1610.02743 (cit. on pp. 36, 57).

ACTPol collaboration (Dec. 2016a). "The Atacama Cosmology Telescope: The Polarization-sensitive ACTPol Instrument". In: ApJS 227, 21, p. 21. DOI: 10.3847/1538-4365/227/2/21. arXiv: 1605.06569 [astro-ph.IM] (cit. on p. 35).

ACTPol collaboration (Dec. 2016b). "The Atacama Cosmology Telescope: The Polarization-sensitive ACTPol Instrument". In: ApJS 227, 21, p. 21. DOI: 10.3847/1538-4365/227/2/21. arXiv: 1605.06569 [astro-ph.IM] (cit. on p. 56).

Ade, P. A. R. et al. (2015). "Planck intermediate results. XIX. An overview of the polarized thermal emission from Galactic dust". In: *Astronomy & Astrophysics* 576, A104. ISSN: 1432-0746. DOI: 10.1051/0004-6361/201424082. URL: http://dx.doi.org/10.1051/0004-6361/201424082 (cit. on p. 43).

Ade, P. et al. (2018). "Constraints on Primordial Gravitational Waves Using Planck , WMAP, and New BICEP2/ Keck Observations through the 2015 Season". In: *Physical Review Letters* 121.22. ISSN: 1079-7114. DOI: 10.1103/physrevlett.121.221301. URL: http://dx.doi.org/10.1103/PhysRevLett.121.221301 (cit. on p. 36).

Ade, P.A.R. et al. (2014). "Detection of B-Mode Polarization at Degree Angular Scales by BICEP2". In: *Physical Review Letters* 112.24. ISSN: 1079-7114. DOI: 10.1103/physrevlett.112.241101. URL: http://dx.doi.org/10.1103/PhysRevLett.112.241101 (cit. on p. 36).

Ade, Peter et al. (2019). In: 2019.02, pp. 056–056. DOI: 10.1088/1475-7516/2019/02/056. URL: https://doi.org/10.1088%2F1475-7516%2F2019%2F02%2F056 (cit. on p. 56).

Aghanim, N. et al. (2014). "Planck2013 results. III. LFI systematic uncertainties". In: *Astronomy & Astrophysics* 571, A3. ISSN: 1432-0746. DOI: 10.1051/0004-6361/201321574. URL: http://dx.doi.org/10.1051/0004-6361/201321574 (cit. on p. 51).

Alpher, V. S. (Nov. 2014). "Ralph A. Alpher, George Antonovich Gamow, and the Prediction of the Cosmic Microwave Background Radiation". In: *ArXiv e-prints*. arXiv: 1411.0172 (cit. on p. 14).

Barkats, D. et al. (2005). "Cosmic Microwave Background Polarimetry Using Correlation Receivers with the PIQUE and CAPMAP Experiments". In: *The Astrophysical Journal Supplement Series* 159.1, pp. 1–26. DOI: 10.1086/430208. URL: https://doi.org/10.1086%2F430208 (cit. on p. 79).

Bassett, Bruce A., Shinji Tsujikawa, and David Wands (2006). "Inflation dynamics and reheating". In: *Reviews of Modern Physics* 78.2, 537–589. ISSN: 1539-0756. DOI: 10.1103/revmodphys.78.537. URL: http://dx.doi.org/10.1103/RevModPhys.78.537 (cit. on p. 26).

Baumann, Daniel (2009). *TASI Lectures on Inflation*. arXiv: 0907.5424 [hep-th] (cit. on p. 27).

Bennett, C. L. et al. (Jan. 2003). "The Microwave Anisotropy Probe Mission". In: ApJ 583, pp. 1–23. DOI: 10.1086/345346. eprint: astro-ph/0301158 (cit. on pp. 16, 58).

Benson, B. A. and SPT collaboration (July 2014). "SPT-3G: a next-generation cosmic microwave background polarization experiment on the South Pole telescope". In: *Millimeter, Submillimeter, and Far-Infrared Detectors and Instrumentation for Astronomy VII*. Vol. 9153. Proc. SPIE, 91531P. DOI: 10.1117/12.2057305. arXiv: 1407.2973 [astro-ph.IM] (cit. on pp. 35, 56).

Bersanelli, M. et al. (2012). "A coherent polarimeter array for the Large Scale Polarization Explorer (LSPE) balloon experiment". In: Proc. SPIE. Vol. 8446. Society of Photo-Optical Instrumentation Engineers (SPIE) Conference Series, p. 84467C. DOI: 10.1117/12.925688. arXiv: 1208.0164 [astro-ph.IM] (cit. on p. 66).

Bersanelli, M. et al. (2010). "Planck pre-launch status: Design and description of the Low Frequency Instrument". In: *Astronomy & Astrophysics* 520, A4. DOI: 10.1051/0004-6361/200912853. URL: https://doi.org/10.1051/0004-6361/200912853 (cit. on p. 79).

Betoule, M. et al. (2014). "Improved cosmological constraints from a joint analysis of the SDSS-II and SNLS supernova samples". In: A&A 568, A22, A22. DOI: 10.1051/0004-6361/201423413. arXiv: 1401.4064 [astro-ph.CO] (cit. on p. 2).

BICEP2/Keck Collaboration and Planck Collaboration (2015). "Joint Analysis of BICEP2/Keck Array and Planck Data". In: Phys. Rev. Lett. 114.10,

101301, p. 101301. DOI: 10.1103/PhysRevLett.114.101301. arXiv: 1502.00612 [astro-ph.CO] (cit. on p. 39).

Bischoff, C. et al. (2013). "The Q/U Imaging ExperimenT Instrument". In: ApJ 768.1, 9, p. 9. DOI: 10.1088/0004-637X/768/1/9. arXiv: 1207.5562 [astro-ph.IM] (cit. on p. 77).

Bischoff, Colin (2010). "Observing the cosmic microwave background polarization anisotropy at 40 GHz with QUIET". PhD thesis. The University of Chicago (cit. on pp. 82, 87).

Bornemann, J. and V. A. Labay (1995). "Ridge waveguide polarizer with finite and stepped-thickness septum". In: *IEEE Transactions on Microwave Theory and Techniques* 43.8, pp. 1782–1787. ISSN: 0018-9480. DOI: 10.1109/22.402260 (cit. on p. 72).

Calvo, M. et al. (Aug. 2016). "The NIKA2 Instrument, A Dual-Band Kilopixel KID Array for Millimetric Astronomy". In: *Journal of Low Temperature Physics* 184, pp. 816–823. DOI: 10.1007/s10909-016-1582-0. arXiv: 1601.02774 [astro-ph.IM] (cit. on p. 51).

Castro-Almazán, Julio A. et al. (2016). "Precipitable Water Vapour at the Canarian Observatories (Teide and Roque de los Muchachos) from routine GPS". In: *Observatory Operations: Strategies, Processes, and Systems VI*. Vol. 9910. Society of Photo-Optical Instrumentation Engineers (SPIE) Conference Series, 99100P. DOI: 10.1117/12.2232646 (cit. on p. 68).

Choi, J. et al. (Jan. 2018). "Status of the GroundBIRD Telescope". In: *European Physical Journal Web of Conferences*. Vol. 168. European Physical Journal Web of Conferences, p. 01014. DOI: 10.1051/epjconf/201816801014 (cit. on pp. 51, 57, 68).

CLASS collaboration (July 2016). "The Cosmology Large Angular Scale Surveyor". In: *Millimeter, Submillimeter, and Far-Infrared Detectors and Instrumentation for Astronomy VIII*. Vol. 9914. Proc. SPIE, 99141K. DOI: 10.1117/12.2233125. arXiv: 1608.08234 [astro-ph.IM] (cit. on p. 56).

Cleary, Kieran A. (2010). "Coherent polarimeter modules for the QUIET experiment". In: vol. 7741. DOI: 10.1117/12.857673. URL: https://doi.org/10.1117/12.857673 (cit. on p. 70).

collaboration, BICEP3/Keck (July 2016). "BICEP3 performance overview and planned Keck Array upgrade". In: *Millimeter, Submillimeter, and Far-Infrared Detectors and Instrumentation for Astronomy VIII*. Vol. 9914. Proc. SPIE, 99140S. DOI: 10.1117/12.2233894. arXiv: 1607.04668 [astro-ph.IM] (cit. on p. 56).

Collaboration, BICEP/Keck et al. (2018). *Measurements of Degree-Scale B-mode Polarization with the BICEP/Keck Experiments at South Pole*. arXiv: 1807.02199 [astro-ph.CO] (cit. on pp. 31, 33, 38).

Columbro, F. et al. (2019). "The short wavelength instrument for the polarization explorer balloon-borne experiment: Polarization modulation issues". In: *Astronomische Nachrichten* 340.83, pp. 83–88. DOI: 10.1002/asna.201913566. arXiv: 1904.01891 [astro-ph.IM] (cit. on p. 66).

Coppi, Gabriele et al. (July 2016). "Developing a long duration 3 He fridge for the LSPE-SWIPE instrument". In: p. 991265. DOI: 10.1117/12.2232448 (cit. on p. 65).

Day, Peter K. et al. (2003). "A broadband superconducting detector suitable for use in large arrays". In: *Nature* 425.6960, pp. 817–821. DOI: 10.1038/nature02037. URL: https://doi.org/10.1038/nature02037 (cit. on p. 51).

de Bernardis, P., S. Masi, and OLIMPO and LSPE Teams (Jan. 2013). "Precision CMB measurements with long-duration stratospheric balloons: activities in the Arctic". In: *Astrophysics from Antarctica*. Ed. by M. G. Burton, X. Cui, and N. F. H. Tothill. Vol. 288. IAU Symposium, pp. 208–213. DOI: 10.1017/S1743921312016894 (cit. on p. 64).

de Bernardis, P. et al. (2012). "SWIPE: a bolometric polarimeter for the Large-Scale Polarization Explorer". In: Proc. SPIE. Vol. 8452. Society of Photo-Optical Instrumentation Engineers (SPIE) Conference Series, 84523F. DOI: 10.1117/12.926569. arXiv: 1208.0282 [astro-ph.IM] (cit. on pp. 58, 62).

de Gasperis, G. et al. (2005). "ROMA: A map-making algorithm for polarised CMB data sets". In: A&A 436.3, pp. 1159–1165. DOI: 10.1051/0004-6361:20042512. arXiv: astro-ph/0502142 [astro-ph] (cit. on pp. 117, 149).

Delabrouille, J. (Feb. 1998). "Analysis of the accuracy of a destriping method for future cosmic microwave background mapping with the PLANCK SURVEYOR satellite". In: A&AS 127, pp. 555–567. DOI: 10.1051/aas:1998119 (cit. on pp. 117, 127).

Dickinson, Clive (2016). *CMB foregrounds - A brief review*. arXiv: 1606.03606 [astro-ph.CO] (cit. on p. 40).

Dickinson, Clive et al. (2018). "The State-of-Play of Anomalous Microwave Emission (AME) research". In: *New Astronomy Reviews* 80, 1–28. ISSN: 1387-6473. DOI: 10.1016/j.newar.2018.02.001. URL: http://dx.doi.org/10.1016/j.newar.2018.02.001 (cit. on p. 44).

Dodelson, Scott (2003). *Modern Cosmology*. Academic Press (cit. on p. 27).

Donzelli, Simona et al. (2009). "Impact of the 1/f noise and the asymmetric beam on non-Gaussianity searches with Planck". In: *Astrophys. J.* 706, pp. 1226–1240. DOI: 10.1088/0004-637X/706/2/1226. arXiv: 0907.4650 [astro-ph.CO] (cit. on p. 119).

Doré, O. et al. (2001). "MAPCUMBA: A fast iterative multi-grid map-making algorithm for CMB experiments". In: A&A 374, pp. 358–370. DOI: 10.

1051/0004-6361:20010692. arXiv: astro-ph/0101112 [astro-ph] (cit. on p. 117).

Draine, B. T. and Brandon S. Hensley (2016). "Quantum suppression of alignment in ultrasmall grains: microwave emission from spinning dust will be negligibly polarized". In: *The Astrophysical Journal* 831.1, p. 59. ISSN: 1538-4357. DOI: 10.3847/0004-637x/831/1/59. URL: http://dx.doi.org/10.3847/0004-637X/831/1/59 (cit. on p. 44).

EBEX collaboration (June 2013). "The E and B EXperiment EBEX". In: *American Astronomical Society Meeting Abstracts*. Vol. 222. American Astronomical Society Meeting Abstracts, p. 119.07 (cit. on p. 58).

Einstein, A. (1916). "Die Grundlage der allgemeinen Relativitätstheorie". In: *Annalen der Physik* 354.7, pp. 769–822. DOI: 10.1002/andp.19163540702. eprint: https://onlinelibrary.wiley.com/doi/pdf/10.1002/andp.19163540702. URL: https://onlinelibrary.wiley.com/doi/abs/10.1002/andp.19163540702 (cit. on p. 5).

Errard, J. et al. (2015). "Modeling Atmospheric emission for CMB ground-based observations". In: *The Astrophysical Journal* 809.1, p. 63. DOI: 10.1088/0004-637x/809/1/63. URL: https://doi.org/10.1088%2F0004-637x%2F809%2F1%2F63 (cit. on p. 55).

Farese, Philip C. et al. (2004). "COMPASS: An Upper Limit on Cosmic Microwave Background Polarization at an Angular Scale of 20′". In: *The Astrophysical Journal* 610.2, pp. 625–634. DOI: 10.1086/421837. URL: https://doi.org/10.1086%2F421837 (cit. on p. 79).

Femenía, B. et al. (1998). "The Instituto de Astrofísica de Canarias-Bartol Cosmic Microwave Background Anisotropy Experiment: Results of the 1994 Campaign". In: ApJ 498.1, pp. 117–136. DOI: 10.1086/305549. arXiv: astro-ph/9711225 [astro-ph] (cit. on p. 68).

Fernández-Cerezo, S. et al. (2006). "Observations of the cosmic microwave background and galactic foregrounds at 12-17GHz with the COSMOSOMAS experiment". In: MNRAS 370.1, pp. 15–24. DOI: 10.1111/j.1365-2966.2006.10505.x. arXiv: astro-ph/0601203 [astro-ph] (cit. on p. 68).

Fixsen, D. J. et al. (Sept. 1997). "The Spectrum of the Cosmic Microwave Background Anisotropy from the Combined COBE FIRAS and DMR Observations". In: *The Astrophysical Journal* 486, pp. 623–628. DOI: 10.1086/304560. eprint: astro-ph/9704176 (cit. on p. 16).

Franceschet, Cristian et al. (2018). "The STRIP instrument of the Large Scale Polarization Explorer: microwave eyes to map the Galactic polarized foregrounds". In: *Millimeter, Submillimeter, and Far-Infrared Detectors and Instrumentation for Astronomy IX*. Vol. 10708. Society of Photo-Optical Instrumentation Engineers (SPIE) Conference Series, 107081G. DOI: 10.1117/12.2313558 (cit. on pp. 66, 71, 74).

Génova-Santos, R. et al. (2015). "QUIJOTE scientific results - I. Measurements of the intensity and polarisation of the anomalous microwave emission in the Perseus molecular complex". In: MNRAS 452.4, pp. 4169–4182. DOI: `10.1093/mnras/stv1405`. arXiv: `1501.04491 [astro-ph.GA]` (cit. on p. 68).

Génova-Santos, R. et al. (2017). "QUIJOTE scientific results - II. Polarisation measurements of the microwave emission in the Galactic molecular complexes W43 and W47 and supernova remnant W44". In: MNRAS 464.4, pp. 4107–4132. DOI: `10.1093/mnras/stw2503`. arXiv: `1605.04741 [astro-ph.GA]` (cit. on p. 68).

Górski, K. M. et al. (Apr. 2005). "HEALPix: A Framework for High-Resolution Discretization and Fast Analysis of Data Distributed on the Sphere". In: ApJ 622, pp. 759–771. DOI: `10.1086/427976`. eprint: `astro-ph/0409513` (cit. on p. 115).

Gualtieri, Riccardo (Jan. 2016). "Multi-mode TES bolometer optimization for the LSPE-SWIPE instrument". In: *Journal of Low Temperature Physics* 184. DOI: `10.1007/s10909-015-1436-1` (cit. on p. 65).

Guth, Alan H. (1981). "Inflationary universe: A possible solution to the horizon and flatness problems". In: *Phys. Rev. D* 23 (2), pp. 347–356. DOI: `10.1103/PhysRevD.23.347`. URL: `https://link.aps.org/doi/10.1103/PhysRevD.23.347` (cit. on p. 23).

Gutiérrez, C. M. et al. (2000). "The Tenerife Cosmic Microwave Background Maps: Observations and First Analysis". In: ApJ 529.1, pp. 47–55. DOI: `10.1086/308246`. arXiv: `astro-ph/9903196 [astro-ph]` (cit. on p. 68).

Harrison, D. L. et al. (2000). "A measurement at the first acoustic peak of the cosmic microwave background with the 33-GHz interferometer". In: MNRAS 316.2, pp. L24–L28. DOI: `10.1046/j.1365-8711.2000.03762.x`. arXiv: `astro-ph/0004357 [astro-ph]` (cit. on p. 68).

Hivon, Eric et al. (May 2001). "MASTER of the Cosmic Microwave Background Anisotropy Power Spectrum: A Fast Method for Statistical Analysis of Large and Complex Cosmic Microwave Background Data Sets". In: *The Astrophysical Journal* 567. DOI: `10.1086/338126` (cit. on p. 117).

Hu, W. and M. White (Oct. 1997). "A CMB polarization primer". In: New A 2, pp. 323–344. DOI: `10.1016/S1384-1076(97)00022-5`. eprint: `astro-ph/9706147` (cit. on pp. 29, 34).

Hubble, Edwin (1929). "A relation between distance and radial velocity among extra-galactic nebulae". In: *Proceedings of the National Academy of Sciences* 15.3, pp. 168–173. ISSN: 0027-8424. DOI: `10.1073/pnas.15.3.168`. eprint: `https://www.pnas.org/content/15/3/168.full.pdf`. URL: `https://www.pnas.org/content/15/3/168` (cit. on p. 2).

Iarocci, A. et al. (Nov. 2008). "PEGASO: An ultra light long duration strato-spheric payload for polar regions flights". In: *Advances in Space Research* 42, pp. 1633–1640. DOI: 10.1016/j.asr.2007.05.079 (cit. on p. 64).

Ichiki, Kiyotomo (June 2014). "CMB foreground: A concise review". In: *Progress of Theoretical and Experimental Physics* 2014, 6B109–0. DOI: 10.1093/ptep/ptu065 (cit. on pp. 41, 42).

Jarosik, N. et al. (2003). "First-YearWilkinson Microwave Anisotropy Probe (WMAP) Observations: On-Orbit Radiometer Characterization". In: *The Astrophysical Journal Supplement Series* 148.1, pp. 29–37. DOI: 10.1086/377221. URL: https://doi.org/10.1086%2F377221 (cit. on p. 79).

Jones, Michael E et al. (2018). "The C-Band All-Sky Survey (C-BASS): design and capabilities". In: *Monthly Notices of the Royal Astronomical Society* 480.3, 3224–3242. ISSN: 1365-2966. DOI: 10.1093/mnras/sty1956. URL: http://dx.doi.org/10.1093/mnras/sty1956 (cit. on p. 57).

K. Grimes, P et al. (Jan. 2009). "Clover - Measuring the Cosmic Microwave Background B-mode Polarization". In: (cit. on p. 70).

Keating, B. and PolarBEAR collaboration (Oct. 2011). "Ultra High Energy Cosmology with POLARBEAR". In: *ArXiv e-prints*. arXiv: 1110.2101 [astro-ph.CO] (cit. on pp. 35, 56).

Keihanen, E. and et al. (Apr. 2003). "A maximum likelihood approach to the destriping technique". In: *Astronomy and Astrophysics* 428. DOI: 10.1051/0004-6361:200400060 (cit. on p. 122).

Keihanen, E. and et al. (June 2005). "MADAM - a map-making method for CMB experiments". English. In: *Monthly Notices of the Royal Astronomical Society* 360.1, pp. 390–400. ISSN: 0035-8711. DOI: 10.1111/j.1365-2966.2005.09055.x (cit. on pp. 121, 127, 149).

Keihanen, E. et al. (July 2009). "Making CMB temperature and polarization maps with Madam". In: (cit. on p. 149).

Klypin, A. A., I. A. Strukov, and D. P. Skulachev (Sept. 1992). "The Relikt mis-sions - Results and prospects for detection of the microwave background anisotropy". In: MNRAS 258, pp. 71–81. DOI: 10.1093/mnras/258.1.71 (cit. on p. 58).

Kovac, J. M. et al. (2002). "Detection of polarization in the cosmic microwave background using DASI". In: *Nature* 420.6917, 772–787. ISSN: 1476-4687. DOI: 10.1038/nature01269. URL: http://dx.doi.org/10.1038/nature01269 (cit. on p. 35).

Krachmalnicoff, Nicoletta (2015). "Challenges for present and future cosmic microwave background observations: systematics effects and foreground emission in polarization". PhD thesis. Università degli Studi di Milano (cit. on pp. 111, 153).

Kurki-Suonio, H. et al. (2009). "Destriping CMB temperature and polariza-tion maps". In: *Astronomy & Astrophysics* 506.3, 1511–1539. ISSN: 1432-

0746. DOI: 10.1051/0004-6361/200912361. URL: http://dx.doi.org/10.1051/0004-6361/200912361 (cit. on pp. 120, 126, 127, 143, 149).

Kusaka, A. et al. (Mar. 2014). "Publisher's Note: "Modulation of cosmic microwave background polarization with a warm rapidly rotating half-wave plate on the Atacama B-Mode Search instrument" [Rev. Sci. Instrum. 85, 024501 (2014)]". In: *Review of Scientific Instruments* 85.3, 039901, p. 039901. DOI: 10.1063/1.4867655. arXiv: 1310.3711 [astro-ph.IM] (cit. on p. 51).

Lawrence, C R et al. (2009). "Coherent detectors". In: *Journal of Physics: Conference Series* 155.1, p. 012002. URL: http://stacks.iop.org/1742-6596/155/i=1/a=012002 (cit. on p. 50).

Lazarian, A and D Finkbeiner (2003). "Microwave emission from aligned dust". In: *New Astronomy Reviews* 47.11-12, 1107–1116. ISSN: 1387-6473. DOI: 10.1016/j.newar.2003.09.037. URL: http://dx.doi.org/10.1016/j.newar.2003.09.037 (cit. on p. 41).

Li, Hong et al. (2018). "Probing primordial gravitational waves: Ali CMB Polarization Telescope". In: *National Science Review* 6.1, 145–154. ISSN: 2053-714X. DOI: 10.1093/nsr/nwy019. URL: http://dx.doi.org/10.1093/nsr/nwy019 (cit. on p. 57).

Liddle, Andrew (2005). *An Introduction to Modern Cosmology. Second Edition*. Wiley (cit. on p. 1).

Maino, D. et al. (1999). "The Planck-LFI instrument: Analysis of the $1/f$ noise and implications for the scanning strategy". In: *Astronomy & Astrophysics Supplement Series* 140.3, 383–391. ISSN: 1286-4846. DOI: 10.1051/aas:1999429. URL: http://dx.doi.org/10.1051/aas:1999429 (cit. on p. 117).

Maino, D. et al. (2002). "Removing $1/f$ noise stripes in cosmic microwave background anisotropy observations". In: *Astronomy & Astrophysics* 387.1, 356–365. ISSN: 1432-746. DOI: 10.1051/0004-6361:20020242. URL: http://dx.doi.org/10.1051/0004-6361:20020242 (cit. on pp. 117, 127).

Mather, J. C. et al. (1991). "Early results from the Cosmic Background Explorer (COBE)". In: *Advances in Space Research* 11, pp. 181–191. DOI: 10.1016/0273-1177(91)90489-7 (cit. on p. 58).

Natoli, P. et al. (2001). "A Map-Making algorithm for the Planck Surveyor". In: *Astronomy & Astrophysics* 372.1, 346–356. ISSN: 1432-746. DOI: 10.1051/0004-6361:20010393. URL: http://dx.doi.org/10.1051/0004-6361:20010393 (cit. on p. 117).

Newburgh, Laura (2010). "The Q/U Imaging ExperimenT (QUIET): The Q-band Receiver Array Instrument and Observations". PhD thesis. Columbia University (cit. on p. 94).

OLIMPO collaboration (Aug. 2005). "A balloon-borne survey of the mm/sub-mm sky: OLIMPO". In: *17th ESA Symposium on European Rocket and Balloon Programmes and Related Research*. Ed. by B. Warmbein. Vol. 590. ESA Special Publication, pp. 581–586 (cit. on p. 58).

Padin, S. et al. (Jan. 2002). "The Cosmic Background Imager". In: PASP 114, pp. 83–97. DOI: 10.1086/324786. eprint: astro-ph/0110124 (cit. on p. 79).

Paine, Scott (Sept. 2019). *The am atmospheric model*. Version 11.0. DOI: 10.5281/zenodo.3406496. URL: https://doi.org/10.5281/zenodo.3406496 (cit. on pp. 77, 139).

Paykari, P. and J.-L. S. Starck (2012). "Cosmic Microwave Background Data Analysis". In: *Advances in Machine Learning and Data Mining for Astronomy*. Ed. by M. J. Way et al., pp. 55–87 (cit. on p. 112).

Penzias, A. A. and R. W. Wilson (July 1965). "A Measurement of Excess Antenna Temperature at 4080 Mc/s." In: ApJ 142, pp. 419–421. DOI: 10.1086/148307 (cit. on p. 16).

Perlmutter, S. et al. (1999). "Measurements of Ω and Λ from 42 High-Redshift Supernovae". In: ApJ 517.2, pp. 565–586. DOI: 10.1086/307221. arXiv: astro-ph/9812133 [astro-ph] (cit. on p. 2).

Peterzen, S., S. Masi, and P. Debernardis (2010). "Polar Stratospheric Research Platforms -Ballooning in the Polar Regions". In: *38th COSPAR Scientific Assembly*. Vol. 38. COSPAR Meeting, p. 4 (cit. on pp. 64, 67).

Peterzen, S. et al. (2008). "Long Duration Balloon flights development. (Italian Space Agency)". In: Mem. Soc. Astron. Italiana 79, p. 792 (cit. on p. 64).

Peverini, Oscar et al. (Sept. 2015). "Q-band antenna-feed system for the Large Scale Polarization Explorer balloon experiment". In: pp. 883–886. DOI: 10.1109/ICEAA.2015.7297240 (cit. on p. 72).

Piacentini, Francesco et al. (Oct. 2018). "Winter long duration stratospheric balloons from Polar regions". In: *arXiv e-prints*. arXiv: 1810.05565 [astro-ph.IM] (cit. on p. 65).

Pincella, Claudio (2017). "Characterization of the polarimeters of the STRIP-LSPE experiment". Università degli Studi di Milano Bicocca (cit. on p. 140).

PIPER collaboration (Jan. 2017). "The Primordial Inflation Polarization Explorer (PIPER)". In: *American Astronomical Society Meeting Abstracts*. Vol. 229. American Astronomical Society Meeting Abstracts, p. 430.04 (cit. on p. 58).

Planck Collaboration (2016). "Planck 2015 results. I. Overview of products and scientific results". In: A&A 594, A1. DOI: 10.1051/0004-6361/201527101. URL: https://doi.org/10.1051/0004-6361/201527101 (cit. on pp. 16, 58).

Planck Collaboration (2018). "Planck 2018 results. IV. Diffuse component separation". In: arXiv: 1807.06208 [astro-ph.CO] (cit. on pp. 19, 42, 43, 46).

Planck Collaboration et al. (2016). "Planck 2015 results. XVI. Isotropy and statistics of the CMB". In: A&A 594, A16, A16. DOI: 10.1051/0004-6361/201526681. arXiv: 1506.07135 [astro-ph.CO] (cit. on p. 61).

Planck Collaboration et al. (2018). "Planck 2018 results. VI. Cosmological parameters". In: *arXiv e-prints*, arXiv:1807.06209, arXiv:1807.06209. arXiv: 1807.06209 [astro-ph.CO] (cit. on pp. 2, 7, 11, 19, 20, 37).

Pogosian, Levon et al. (2019). "Future CMB constraints on cosmic birefringence and implications for fundamental physics". In: Phys. Rev. D 100.2, 023507, p. 023507. DOI: 10.1103/PhysRevD.100.023507. arXiv: 1904.07855 [astro-ph.CO] (cit. on p. 61).

Poidevin, F. et al. (2019). "QUIJOTE scientific results - III. Microwave spectrum of intensity and polarization in the Taurus Molecular Cloud complex and L1527". In: MNRAS 486.1, pp. 462–485. DOI: 10.1093/mnras/sty3462. arXiv: 1812.08274 [astro-ph.GA] (cit. on p. 68).

Poletti, Davide et al. (2017). "Making maps of cosmic microwave background polarization forB-mode studies: the POLARBEAR example". In: *Astronomy & Astrophysics* 600, A60. ISSN: 1432-0746. DOI: 10.1051/0004-6361/201629467. URL: http://dx.doi.org/10.1051/0004-6361/201629467 (cit. on pp. 117, 118).

Poutanen, T. et al. (2006). "Comparison of map-making algorithms for CMB experiments". In: *Astronomy & Astrophysics* 449.3, 1311–1322. ISSN: 1432-0746. DOI: 10.1051/0004-6361:20052845. URL: http://dx.doi.org/10.1051/0004-6361:20052845 (cit. on p. 118).

Press, W. et al. (2007). *Numerical recipes. The art of Scientific Computing - Third edition*. Cambridge University Press (cit. on p. 100).

QUBIC collaboration (Sept. 2016). "QUBIC Technical Design Report". In: *ArXiv e-prints*. arXiv: 1609.04372 [astro-ph.IM] (cit. on p. 57).

QUIET Collaboration et al. (2011). "First Season QUIET Observations: Measurements of Cosmic Microwave Background Polarization Power Spectra at 43 GHz in the Multipole Range 25 <= ℓ <= 475". In: ApJ 741.2, 111, p. 111. DOI: 10.1088/0004-637X/741/2/111. arXiv: 1012.3191 [astro-ph.CO] (cit. on pp. 72, 79).

QUIET Collaboration et al. (2012). "Second Season QUIET Observations: Measurements of the Cosmic Microwave Background Polarization Power Spectrum at 95 GHz". In: ApJ 760.2, 145, p. 145. DOI: 10.1088/0004-637X/760/2/145. arXiv: 1207.5034 [astro-ph.CO] (cit. on p. 74).

R. Pardo, Juan, J Cernicharo, and E Serabyn (Jan. 2002). "Atmospheric transmission at microwaves (ATM): An improved model for millimeter/sub-

millimeter applications". In: *Antennas and Propagation, IEEE Transactions on* 49, pp. 1683 –1694. DOI: 10.1109/8.982447 (cit. on pp. 77, 140).

Readhead, A. C. S. (2004). "Polarization Observations with the Cosmic Background Imager". In: *Science* 306.5697, 836–844. ISSN: 1095-9203. DOI: 10.1126/science.1105598. URL: http://dx.doi.org/10.1126/science.1105598 (cit. on p. 35).

Remazeilles, M. et al. (2016). "Sensitivity and foreground modelling for large-scale cosmic microwave background B-mode polarization satellite missions". In: *Monthly Notices of the Royal Astronomical Society* 458.2, 2032–2050. ISSN: 1365-2966. DOI: 10.1093/mnras/stw441. URL: http://dx.doi.org/10.1093/mnras/stw441 (cit. on p. 44).

Revenu, Benoît et al. (May 1999). "Destriping of Polarized Data in a CMB Mission with a Circular Scanning Strategy". In: *A and AS* 142. DOI: 10.1051/aas:2000308 (cit. on p. 117).

Riess, Adam G. et al. (1998). "Observational Evidence from Supernovae for an Accelerating Universe and a Cosmological Constant". In: AJ 116.3, pp. 1009–1038. DOI: 10.1086/300499. arXiv: astro-ph/9805201 [astro-ph] (cit. on p. 2).

Rubiño-Martín, J. A. et al. (2012). "The QUIJOTE-CMB experiment: studying the polarisation of the galactic and cosmological microwave emissions". In: *Ground-based and Airborne Telescopes IV*. Vol. 8444. Society of Photo-Optical Instrumentation Engineers (SPIE) Conference Series, 84442Y. DOI: 10.1117/12.926581 (cit. on pp. 57, 68).

Rybicki, G. B. and A. P. Lightman (1979). *Radiative processes in astrophysics* (cit. on p. 40).

Ryden, Barbara (2017). *Introduction to Cosmology. Second Edition*. Cambridge University Press (cit. on p. 1).

SPIDER collaboration (July 2010). "SPIDER: a balloon-borne CMB polarimeter for large angular scales". In: *Millimeter, Submillimeter, and Far-Infrared Detectors and Instrumentation for Astronomy V*. Vol. 7741. Proc. SPIE, 77411N. DOI: 10.1117/12.857720. arXiv: 1106.2158 [astro-ph.CO] (cit. on p. 58).

Stompor, Radek et al. (2001). "Making maps of the cosmic microwave background: The MAXIMA example". In: *Physical Review D* 65.2. ISSN: 1089-4918. DOI: 10.1103/physrevd.65.022003. URL: http://dx.doi.org/10.1103/PhysRevD.65.022003 (cit. on p. 117).

Strikwerda, John (2004). *Finite Difference Schemes and Partial Differential Equations*. SIAM (cit. on p. 123).

Sutton, D. et al. (Dec. 2009). "Fast and precise map-making for massively multi-detector CMB experiments". In: *Monthly Notices of the Royal Astronomical Society* 407. DOI: 10.1111/j.1365-2966.2010.16954.x (cit. on pp. 118, 127).

Takakura, S. et al. (Jan. 2019). "Measurements of Tropospheric Ice Clouds with a Ground-based CMB Polarization Experiment, POLARBEAR". In: *The Astrophysical Journal* 870, p. 102. DOI: 10.3847/1538-4357/aaf381 (cit. on p. 56).

Tran, Huan et al. (2008). "Comparison of the crossed and the Gregorian Mizuguchi-Dragone for wide-field millimeter-wave astronomy". In: *Appl. Opt.* 47.2, pp. 103–109. DOI: 10.1364/AO.47.000103. URL: http://ao.osa.org/abstract.cfm?URI=ao-47-2-103 (cit. on p. 69).

Watson, Robert A. et al. (2003). "First results from the Very Small Array - I. Observational methods". In: MNRAS 341.4, pp. 1057–1065. DOI: 10.1046/j.1365-8711.2003.06338.x. arXiv: astro-ph/0205378 [astro-ph] (cit. on p. 68).

Zaldarriaga, Matias and Uroš Seljak (1997). "All-sky analysis of polarization in the microwave background". In: *Physical Review D* 55.4, 1830–1840. ISSN: 1089-4918. DOI: 10.1103/physrevd.55.1830. URL: http://dx.doi.org/10.1103/PhysRevD.55.1830 (cit. on pp. 32, 33).

Zonca, A. et al. (2013). "Destriping cosmic microwave background polarimeter data". In: *Astronomy and Computing* 3-4, 13–22. ISSN: 2213-1337. DOI: 10.1016/j.ascom.2013.10.002. URL: http://dx.doi.org/10.1016/j.ascom.2013.10.002 (cit. on p. 127).